

**SUB-WAVELENGTH MICROWAVE RADAR
IMAGING FOR DETECTION OF BREAST CANCER
TUMORS**

Sub-Wavelength Microwave Radar Imaging for Detection of Breast Cancer Tumors

By

Daniel M. Hailu

B. Eng., McMaster University

A THESIS SUBMITTED TO THE SCHOOL OF GRADUATE STUDIES
IN PARTIAL FULFILLMENT OF THE REQUIREMENTS
FOR THE DEGREE
MASTER OF APPLIED SCIENCE

McMaster University
Hamilton, Ontario, Canada

MASTER OF APPLIED SCIENCE (2007)
(Electrical and Computer Engineering)

McMaster University
Hamilton, Ontario

TITLE: **Sub-Wavelength Microwave Radar Imaging for Detection of Breast Cancer Tumors**

AUTHOR: Daniel Hailu
B.Eng. (Computer Engineering with Distinction,
McMaster University, Hamilton, Canada)

SUPERVISORS: Natalia K. Nikolova, Associate Professor,
Department of Electrical and Computer Engineering
Dipl.Eng. (Technical University of Varna)
Ph.D. (University of Electro-Communication)
P.Eng. (Province of Ontario)
Senior Member, IEEE

Mohamed H. Bakr, Associate Professor,
Department of Electrical and Computer Engineering
B.Sc., M.Sc. (Cairo University, Cairo, Egypt)
Ph.D. (McMaster University, Hamilton, Canada)
P.Eng. (Province of Ontario)
Member, IEEE

NUMBER OF PAGES: XXIV, 158

ABSTRACT

Ultra-wideband microwave imaging, with its advantages of absence of breast compression, nonionizing and noninvasive properties, is a complementary method to X-ray mammography for breast cancer detection that is safe and reasonably inexpensive. The motivation for employing microwave imaging techniques for detecting early-stage breast cancer stems from published research results showing the strong contrast in the dielectric properties at microwave frequencies between normal breast tissue and malignant lesion.

This thesis contributes to development of novel techniques for the detection of early-stage breast cancer tumors well below a centimeter with specificity and high degree of accuracy, i.e., with minimum false negatives/positives. In our proposed approach, a modified Shannon entropy criterion (SEC) is formulated for determining when the time-reversed wave focuses back to the source target in the presence of an inhomogeneous lossy medium. It is demonstrated through two examples, the time-reversal mirror and cavity, that the SEC is found to be more robust than the inverse varimax norm. TR has been shown to be superior to other simple delay-based focusing techniques and here we have extended the TR algorithm by making it more robust

in localizing small tumors. The importance of this finding becomes evident as the SEC allows for the detection of tumors that are sub-wavelength in size.

Our novel sub-wavelength ultra-wide band (UWB) microwave radar imaging technique exploits the principle of phase-shifting mask (PSM) from optical lithography and is implemented using a time-reversal (TR) algorithm based on the transmission-line matrix (TLM) method. We incorporate the SEC in a TR algorithm to achieve a robust imaging algorithm exploiting the measurements acquired by our phase-shifting mask (PSM) experimental set-up. Unlike the FDTD TR algorithm by Kosmas *et al.*, which excites one of the 23 antenna elements, we propose a different system where all antennas are stimulated simultaneously with their excitation based on the PSM principle. A 0.5-mm diameter tumor was detected and located using a 200-ps UWB pulse in a realistic inhomogeneous two dimensional breast model. The breast model was derived from magnetic resonance imaging data and simulated using the TLM method. The effect of the dielectric contrast and proximity of tumor to the antenna receivers are examined. A TLM-based TR algorithm employing two types of time reversal mirrors (TRMs) is proposed to improve the accuracy of localizing the sub-wavelength tumors.

The final part of the thesis examines the feasibility and the design of a narrowbeam UWB antenna for microwave breast cancer detection focusing on the antenna feed structure and the printed TEM horn antenna. A feed structure of an UWB antenna for microwave radar imaging is designed. The UWB antennas are

fundamental components of the UWB radar imaging hardware. The performance of the antenna is crucial for the resolution and the reliability of the whole imaging system. A TEM horn antenna is studied and suggestions are made regarding the hardware implementations of the experimental setup. We conclude by suggesting future work toward hardware and practical implementation of UWB microwave radar imaging with high resolution.

*To the glory of my Lord and Savior, Jesus Christ and
to my parents Dr. Hailu Gebre-Mariam and Mrs. Fekerte Haile.*

ACKNOWLEDGEMENTS

The author wishes to express his sincere appreciation to his supervisors Dr. Natalia K. Nikolova and Dr. Mohamed H. Bakr, the Computational Electromagnetics Laboratory, McMaster University, for their expert supervision, for teaching me how to better communicate my research work and continuing encouragement during the course of this work.

I would like to start by sincerely thanking my senior supervisor, Prof. Natalia Nikolova for being always available for support and guidance, identifying my ability to make big and complex problems simple, continually providing me fruitful comments, and for never ceasing to guide me to improve my technical and other weaknesses.

I would also want to express my sincere gratitude and appreciation to my co-supervisor. During the past year, both my supervisors have contributed greatly to my personal growth both technical and inter-personal skills. They also have thought me how to conduct research independently and exposed me to various concepts in computational Electromagnetics, antenna design and biomedical imaging fields. In fact, it was a great honor and pleasurable experience to work under their supervision.

ACKNOWLEDGEMENTS

I am also grateful for Prof. Wei-Ping Huang and Prof. Xun Li for being members on my committee and for being outstanding mentors of my undergraduate courses and brilliant lectures in graduate courses. I greatly admire their dedication for the success of their students, sharing their exceptional expertise and valuable advice.

I would also want to thank NSERC for funding this research. I would like to thank Dr. Brian Yemen, Prof. Gerald R. Moran from the Department of Medical Physics and Applied Radiation Sciences, McMaster University, and the staff of Henderson General Hospital, Hamilton, Canada for making MRI data of breast available for research.

Many thanks are also due to the technical staff members in the Department of Electrical and Computer Engineering at McMaster University, Terry Greenly, Cosmin Coroiu, Steve Spencer and Stan Zolinski. Special thanks to Stan Zolinski for letting use the ECE Department computer.

Finally, I want to express my heartfelt gratitude to my wonderful family for continuously being there for me and for encouragement, understanding and continuous support. Special thanks to my father, helped me build strong character, and never ceased to motivate me in my academic pursuits, and my mother for her spiritual strength, prayers and support.

CONTENTS

| | |
|---|-------------|
| ABSTRACT | III |
| ACKNOWLEDGMENTS | VII |
| LIST OF FIGURES | XIII |
| LIST OF TABLES | XIX |
| LIST OF SYMOLS AND ACRONYMS | XX |
| | |
| CHAPTER 1 INTRODUCTION | 1 |
| 1.1 Motivation..... | 1 |
| 1.2 Outline of Thesis..... | 4 |
| 1.3 Contributions..... | 8 |
| References..... | 9 |
| | |
| CHAPTER 2 REVIEW: ULTRAWIDEBAND MICROWAVE RADAR IMAGING TECHNIQUES FOR BREAST CANCER DETECTION | 14 |
| 2.1 Confocal Microwave Imaging..... | 14 |
| 2.1.1 CMI Focusing Algorithm..... | 15 |
| 2.1.2 Calibration Step: Skin Reflection Clutter Removal Approach | 19 |

CONTENTS

| | | |
|------------------|---|-----------|
| 2.1.3 | Integration Step..... | 19 |
| 2.1.4 | Compensation Step..... | 20 |
| 2.1.5 | Discussion of Advantages and Disadvantages | 21 |
| 2.2 | Microwave Imaging Via Space-Time (MIST) Beamforming | 23 |
| 2.2.1 | MIST Beamforming Algorithm | 25 |
| 2.2.2 | FIR Filter and Window Design | 28 |
| 2.2.3 | Discussion of Advantages and Disadvantages | 30 |
| 2.3 | Time Reversal with the FDTD Method | 33 |
| 2.3.1 | FDTD TR Algorithm | 37 |
| 2.3.2 | Discussion of Advantages and Disadvantages | 41 |
| | References..... | 43 |
| CHAPTER 3 | NOVEL ROBUST TLM-BASED TIME-REVERSAL MICROWAVE RADAR IMAGING TECHNIQUE | 45 |
| 3.1 | Introduction..... | 45 |
| 3.2 | Two-dimensional TM-Mode TR technique with TLM Method..... | 47 |
| 3.3 | Modified Shannon Entropy Criteria..... | 50 |
| 3.4 | Examples..... | 52 |
| 3.4.1 | Planar System using Time-Reversal Mirror | 52 |

| | | |
|------------------|---|-----------|
| 3.4.2 | Cylindrical System using Time-Reversal Cavity | 59 |
| 3.5 | Concluding Remarks..... | 65 |
| | References..... | 66 |
| CHAPTER 4 | ACHIEVING SUB-WAVELENGTH RESOLUTION WITH THE TLM-BASED SHANNON ENTROPY TR TECHNIQUE | 67 |
| 4.1 | Introduction..... | 67 |
| 4.2 | Motivation of Employing Phase-Shifting Mask (PSM) Technology for Sub-wavelength Imaging | 70 |
| 4.3 | Experimental Setup | 75 |
| 4.4 | TLM-based TR Algorithm using Modified Shannon Entropy Criterion (SEC) | 78 |
| 4.5 | Results and Discussions | 80 |
| 4.6 | Effect of Dielectric Contrast | 86 |
| 4.7 | TLM-based TR Algorithm Employing Two TRMs | 87 |
| 4.7.1 | Results and Discussion | 90 |
| 4.7.2 | Effect of Chest Wall | 93 |
| 4.8 | Concluding Remarks..... | 94 |
| | References..... | 95 |

CONTENTS

| | | |
|------------------|---|------------|
| CHAPTER 5 | NARROWBEAM ULTRA WIDEBAND ANTENNAS FOR MICROWAVE BREAST CANCER DETECTION | 97 |
| 5.1 | Introduction..... | 97 |
| 5.2 | Review: TEM Horn Antenna..... | 100 |
| 5.2.1 | Tapered TEM Horn Antenna | 100 |
| 5.2.2 | Double-Ridged Pyramidal Horn Antenna | 102 |
| 5.3 | Antenna Specifications..... | 104 |
| 5.3.1 | Fundamental Antenna Parameters..... | 104 |
| 5.3.2 | Objective..... | 106 |
| 5.4 | Printed Tapered TEM Horn Antenna with Different Feed Structures..... | 109 |
| 5.4.1 | Coaxial-to-Microstrip Feed Transition | 110 |
| 5.4.2 | SMA Connector Modeling..... | 114 |
| 5.4.3 | SMA Connector to Microstrip Feed Transition..... | 116 |
| 5.5 | Concluding Remarks..... | 143 |
| | References..... | 144 |
| CHAPTER 6 | CONCLUSIONS | 148 |
| | BIBLIOGRAPHY | 151 |

LIST OF FIGURES

| | | |
|----------|--|----|
| Fig. 2.1 | CMI involves illuminating the breast with an ultra-wideband pulse from a number of physical antenna locations. (a) Breast model with tumor. (b) Focal point in the breast model. | 16 |
| Fig. 2.2 | Illustration of the MIST beamforming process for nominee location \mathbf{r}_o for the i th antenna channel..... | 25 |
| Fig. 2.3 | An inverse scattering experiment where the measurement data are obtained at \mathbf{r} on S and the transmitter is at $\hat{\mathbf{r}}$ | 35 |
| Fig. 2.4 | The inputs to the TR system are the backscattered fields from the tumor and clutter recorded by the antenna receivers in the forward model. The time reversal mirror (TRM) has antenna element 11 as a transmitter. Antenna element 11 transmits a pulse and all the others including element 11 record the backscattered fields. | 38 |
| Fig. 2.5 | Backpropagation starts from the fields at the antennas and the wave progressively converges to the scatterer at certain optimal time, and then diverges again. The tumor response is found at the peak (shown in white), which occurs at the optimal time. | 39 |
| Fig. 3.1 | 2D-TLM shunt node: (a) illustration of the scattering and connection steps, (b) schematic. | 47 |
| Fig. 3.2 | The 2-D MRI data of a 57 year old female. | 53 |
| Fig. 3.3 | The corresponding 2-D dielectric profile of the inhomogeneous breast tissue. | 53 |

LIST OF FIGURES

| | | |
|-----------|--|----|
| Fig. 3.4 | The inverse varimax norm as function a of time. The first minimum at time step 749 is assigned as a solution. The corresponding tumor location is at -0.85 cm span and 3.55 cm depth. | 55 |
| Fig. 3.5 | The resultant image corresponding to the solution obtained using the inverse varimax norm. The corresponding tumor location is at -0.85 cm span and 3.55 cm depth, while the actual tumor location was at -0.85 cm span and 3.65 cm depth. | 56 |
| Fig. 3.6 | The modified Shannon entropy criterion (SEC) response as function of time. The global minimum is assigned as solution. There is only one minimum instead of multiple minima and the corresponding location to the solution is at -0.85 cm span and 3.55 cm depth. | 57 |
| Fig. 3.7 | The resultant image corresponding to the solution obtained using the SEC. The corresponding tumor location is at -0.85 cm span and 3.55 cm depth, while the actual tumor location was at -0.85 cm span and 3.65 cm depth. | 58 |
| Fig. 3.8 | The MRI-derived 2D TLM model for the cylindrical configuration for heterogeneous breast without tumor. | 59 |
| Fig. 3.9 | The MRI-derived 2D TLM model for the cylindrical configuration for heterogeneous breast with tumor inserted at X span 0.3 cm and Y span 3.65 cm. | 60 |
| Fig. 3.10 | The inverse varimax norm as a function of time. The first minimum does not give accurate solution. The location of the solution using the global minimum is at X span 0.2 cm and Y span 3.55 cm, which is fairly accurate. | 61 |
| Fig. 3.11 | The resultant image corresponding to the solution obtained using the inverse varimax norm. The corresponding location to the solution is at X span 0.2 cm and Y span 3.55 cm. | 62 |
| Fig. 3.12 | The SEC response as a function of time. The first minimum is the global minimum and it gives an accurate solution. The location of the solution is at X span 0.25 cm and Y span 3.55 cm. | 63 |

LIST OF FIGURES

| | | |
|-----------|--|----|
| Fig. 3.13 | The resultant image corresponding to the solution obtained using the SEC. The corresponding location to the solution is at X span 0.25 cm and Y span 3.55 cm. | 64 |
| Fig. 4.1 | (a) The 2-D MRI data of a 57 year old female and (b) the corresponding 2-D dielectric profile of the inhomogeneous breast tissue with the 0.5-mm diameter tumor inserted at -0.95 cm span and 3.7 cm depth. The 23 receivers shown with circles are fed with alternating-phase voltage values. | 76 |
| Fig. 4.2 | Single breast dielectric profile of MRI-derived TLM model with a 0.5-mm diameter tumor inserted at -0.95 cm span and 3.7 cm depth. | 77 |
| Fig. 4.3 | The response for: (a) the inverse varimax norm vs. time and (b) the modified Shannon entropy (SEC) vs. time. There is one minimum obtained at time step 1938 or 2.286 ns, where in (b), the wave converges to an optimal peak value. | 82 |
| Fig. 4.4 | The ghost image created by the TR technique with only one antenna transmitting in the forward model, all receivers transmitting in the TR model, and employing inverse varimax norm. No scatterer is found. | 83 |
| Fig. 4.5 | The image obtained through the proposed TR technique with the TLM method and employing the concept of the PSM and the modified Shannon entropy. | 83 |
| Fig. 4.6 | The difference between the actual location of the tumor and the one found by the proposed TLM TR algorithm using varying taper parameter values. The location of the tumor is -0.95 cm span and 3.7 cm depth. | 85 |
| Fig. 4.7 | The image obtained using two TRMs through the proposed TR technique with TLM method and employing the concept of PSM and SEC. The taper parameters are $\nu = 0.038 \cdot t_p$ and $\nu_2 = 0.003 \cdot t_p$. The 0.5-mm diameter tumor is shown by a black asterisk and the receivers in the TR model are denoted by stars. | 91 |

LIST OF FIGURES

| | | |
|-----------|--|-----|
| Fig. 4.8 | The image obtained using a single TRM, employing the concept of PSM and using SEC. The taper parameter is $\nu = 0.019 \cdot t_p$. The 0.5-mm diameter tumor is shown by a white asterisk and the receivers in the TR model are shown by stars. | 92 |
| Fig. 4.9 | The image obtained using two TRMs, employing the concept of PSM and using SEC. The taper parameters are $\nu = 0.019 \cdot t_p$ and $\nu_2 = 0.215 \cdot t_{p2}$. The 0.5-mm diameter tumor is shown by a black asterisk and the receivers in the TR model are denoted by stars. | 92 |
| Fig. 4.10 | The 2-D dielectric profile of the inhomogeneous breast tissue including the muscle chest wall and a 0.5-mm diameter tumor located close to the chest wall. | 93 |
| Fig. 4.11 | The image obtained using two TRMs, employing the concept of PSM and using SEC. The taper parameters are $\nu = 0.019 \cdot t_p$ and $\nu_2 = 0.215 \cdot t_{p2}$. The 0.5-mm diameter tumor is shown with a red asterisk and the receivers in the TR model are shown as stars. The back-propagating waves focus to a location slightly different from the actual location because of the chest wall reflections. | 94 |
| Fig. 5.1 | Antenna in transmitting mode connected to a transmission line. | 105 |
| Fig. 5.2 | An example of microstrip transmission line design using a circuit model in ADS. | 112 |
| Fig. 5.3 | An example of microstrip transmission line design using EM simulator in HFSS. | 113 |
| Fig. 5.4 | The geometry of the SMA connector feeding the antenna. | 115 |
| Fig. 5.5 | The half-structure of the feed with the SMA connector, microstrip line and radial stub as simulated in HFSS. | 119 |
| Fig. 5.6 | The E-field distribution in the radial stub and the microstrip line as simulated in HFSS. | 119 |

LIST OF FIGURES

| | | |
|-----------|--|-----|
| Fig. 5.7 | The proposed feed structure with the SMA connector, EM coupling structure, and microstrip line implemented on alumina substrate and simulated in HFSS. | 121 |
| Fig. 5.8 | The return loss $ S_{11} $ dB response corresponding to the proposed feed structure in Fig. 5.7 as simulated in HFSS. | 122 |
| Fig. 5.9 | The VSWR response corresponding to the proposed feed structure in Fig. 5.7 as simulated in HFSS. | 123 |
| Fig. 5.10 | Responses: (a) $ S_{12} $ and (b) $ S_{11} ^2 + S_{12} ^2$, corresponding to the proposed feed structure in Fig. 5.7 as simulated in HFSS. | 124 |
| Fig. 5.11 | The proposed feed structure with double-layer dielectric, the SMA connector, EM coupling structure, and microstrip line implemented on alumina substrate and simulated in HFSS. ... | 126 |
| Fig. 5.12 | The return loss $ S_{11} $ dB response corresponding to the proposed feed structure in Fig. 5.11 as simulated in HFSS. ... | 126 |
| Fig. 5.13 | The VSWR response corresponding to the proposed feed structure in Fig. 5.11 as simulated in HFSS. | 127 |
| Fig. 5.14 | Responses: (a) $ S_{12} $ and (b) $ S_{11} ^2 + S_{12} ^2$, corresponding to the proposed feed structure in Fig. 5.11 as simulated in HFSS. | 128 |
| Fig. 5.15 | The near-field radiation pattern: (a) without absorber in the back and (b) with absorber corresponding to the proposed feed structure in Fig. 5.11 as simulated in HFSS. | 129 |
| Fig. 5.16 | The E-field distribution at 6 GHz in the substrate and Teflon extension added for the proposed feed structure in Fig. 5.11 as simulated in HFSS. | 130 |
| Fig. 5.17 | The return loss $ S_{11} $ dB response corresponding to the proposed feed structure with the SMA connector, EM coupling structure, and microstrip implemented on FR4 substrate with thickness of 62 mil as simulated in HFSS. | 131 |

LIST OF FIGURES

| | | |
|-----------|---|-----|
| Fig. 5.18 | The VSWR response corresponding to the proposed feed structure with the SMA connector, EM coupling structure, and microstrip implemented on FR4 substrate with thickness of 62 mil as simulated in HFSS. | 132 |
| Fig. 5.19 | The return loss dB response corresponding to the proposed feed structure with the SMA connector, EM coupling structure, and microstrip implemented on FR4 substrate with thickness of 31 mil as simulated in HFSS. | 133 |
| Fig. 5.20 | The VSWR response corresponding to the proposed feed structure with the SMA connector, EM coupling structure, and microstrip implemented on FR4 substrate with thickness of 31 mil as simulated in HFSS. | 134 |
| Fig. 5.21 | The planar numerical model of the breast medium with the skin layer between the air-breast interface as simulated in HFSS. | 138 |
| Fig. 5.22 | Proposed antenna design #1 with feed structure on alumina substrate and the radiating substrate with dielectric constant of 12.24 and height of 40 mil as simulated in HFSS. | 139 |
| Fig. 5.23 | The return loss response for proposed antenna design #1 as simulated in HFSS. | 140 |
| Fig. 5.24 | The VSWR response for proposed antenna design #1 as simulated in HFSS. | 141 |
| Fig. 5.25 | The group delay response for proposed antenna design #1 as simulated in HFSS. | 142 |

LIST OF TABLES

| | | |
|-----------|--|-----|
| TABLE 2.1 | Comparison of UWB Microwave Radar Imaging Techniques..... | 32 |
| TABLE 4.1 | Comparison of Dielectric Contrast on Detection of Tumor | 86 |
| TABLE 5.1 | Summary of Microstrip Design Parameters..... | 114 |
| TABLE 5.2 | SMA Geometry Parameters..... | 116 |
| TABLE 5.3 | Summary of Comparison of Various Types of Feed Structure for UWB Antennas..... | 137 |
| TABLE 5.4 | Averaged Debye Model Parameters..... | 138 |
| TABLE 5.5 | Antenna Geometry Design Parameters..... | 139 |

LIST OF SYMOLS AND ACRONYMS

Symbols

| | |
|--------------------|---|
| ω | Frequency in radians |
| ϵ_r | Relative permittivity |
| $\tilde{\epsilon}$ | Complex permittivity |
| ϵ_o | Permittivity of free space |
| ϵ_∞ | High frequency permittivity |
| ϵ_s | Low frequency permittivity |
| ϵ_b | Permittivity of background |
| μ | Permeability |
| σ | Conductivity |
| σ_s | Ionic conductivity |
| τ | UWB pulse width |
| ν | Taper parameter |
| ν_2 | Taper parameter for second time-reversal mirror receivers |
| a | Wire radius |
| B_n | Post-processed backscatter waveform at n th antenna |

LIST OF SYMBOLS AND ACRONYMS

| | |
|---------------------|---|
| D^k | Parameter at time step k |
| \hat{G}_s | Normalized lossy stub capacitance |
| H | Shannon Entropy |
| h | Height of dipole antenna |
| n_a | Reference discrete time |
| k | Complex propagation constant |
| k_b | Wavenumber of the background |
| κ | Dimension such as axial coordinate of antenna |
| Γ | Reflection coefficient |
| Ψ_{TR} | Wave field generated by TRM |
| Ψ_{TRS} | Wave field generated by time-reversed source |
| L | FIR filter length |
| P_L | Power lost as heat |
| P_r | Power delivered to the antenna for radiation |
| P_{av}^r | Reflected average power |
| P_{in} | Total input power accepted by antennas |
| r^i | Internal resistance for an antenna |
| R_r | Radiation resistance of the antenna |
| R_L | Loss resistance of the antenna |

LIST OF SYMOBLS AND ACRONYM

| | |
|---------------|--|
| R_A | Antenna resistance at input terminals |
| t_p | Peak time |
| t_{p2} | Peak time for the second set of receivers |
| T_s | Sampling interval |
| λ | Wavelength |
| π | PI |
| Δ_k | Size of the specified trust region |
| V_{ypeak}^k | Maximum voltage for time step k inside breast medium |
| V_y^t | Total field solution response |
| V_y^h | Field solution of analysis of breast model without tumor |
| V_y^p | Particular tumor response |
| V_y^{p2} | Peak of the received waveform from the second TRM |
| V_g | Peak generator voltage incident on the transmission line |
| X_A | Antenna reactance at input terminals |
| \hat{Y}_s | Normalized capacitive stub admittance |
| Z_c | Characteristic impedance |
| Z_{in} | Input imedance |

LIST OF SYMBOLS AND ACRONYMS

Acronyms

| | |
|------|---|
| ADS | Advanced Design System |
| CAD | Computer-Aided Design |
| CEM | Computational Electromagnetics |
| CMI | Confocal Microwave Imaging |
| DWBA | Distorted-Wave Born Approximation |
| EM | Electromagnetics |
| FDTD | Finite Difference Time Domain |
| FIR | Finite Impulse Response |
| FWHM | Full-Width Half-Maximum |
| HFSS | High Frequency Structure Simulator |
| IEEE | Institute of Electrical and Electronics Engineers |
| MIST | Microwave Imaging via Space-Time |
| MoM | Method of Moments |
| MRI | Magnetic Resonance Imaging |
| PCB | Printed Circuit Board |
| PML | Perfectly Matched Layer |
| PSM | Phase-Shifting Mask |
| RF | Radio Frequency |
| SEC | Modified Shannon Entropy Criterion |

LIST OF SYMOBLS AND ACRONYM

| | |
|--------------|-------------------------------------|
| SMA | Sub-Miniature version A |
| S/N | Signal-to-Noise |
| S-parameters | Scattering parameters |
| TEM | Transverse Electromagnetic |
| TLM | Transmission-Line Matrix (Modeling) |
| TM | Transverse Magnetic |
| TR | Time Reversal |
| TRM | Time Reversal Mirror |
| TRC | Time Reversal Cavity |
| TSAR | Tissue Sensing Adaptive Radar |
| UWB | Ultra-Wideband |
| VSWR | Voltage Standing Wave Ratio |

CHAPTER 1

INTRODUCTION

1.1 MOTIVATION

Breast cancer is one of the leading causes of death among women [1]. Annually, an estimated 200,000 new cases of breast cancer are diagnosed and more than 40,000 women die as the result of the disease [1][2]. X-ray mammography remains the primary screening method for detecting early-stage breast tumors. The mammographic technique involves X-ray imaging of a compressed breast. Anywhere between 4% to 34% of all breast cancers are missed by conventional mammography [3] and nearly 70% of all breast lesions identified by mammography turn out to be benign [2][4]. Significant technical advances such as digital mammography [5], driven in part by the Mammography Quality Standards Act, have greatly improved the overall quality and interpretation of mammographic images. Digital mammography has reached a level of maturity with the first digital mammography unit, the General Electric Senographe 2000 D, approved for sale in the United States in February 2000, followed by a large number of digital mammography units being installed

CHAPTER 1 INTRODUCTION

worldwide [5]. Despite this progress, drawbacks of mammography include the need for improved sensitivity and specificity, particularly in the case of radiographically dense breast tissue, the risk of accumulating low-dose ionizing radiation over repeated scans, and patient discomfort due to breast compression during the checkup. These limitations of X-ray mammography provide clear motivation for the development of a complementary breast-imaging tool to assist in early detection and diagnosis.

Microwave imaging, with its advantages of absence of breast compression, nonionizing, and noninvasive properties is a complementary method for breast cancer detection that is safe, and reasonably inexpensive. The motivation for employing microwave imaging techniques for detecting early-stage breast cancer stems from published research results showing the strong contrast in the dielectric properties at microwave frequencies between normal breast tissue and malignant lesion [6] - [9].

Current research in active microwave breast imaging can be divided into two main categories: microwave tomography [10] - [17], and ultrawideband (UWB) radar techniques [18] - [34]. Microwave tomography aims to recover the exact shape, location, and dielectric properties, i.e., relative dielectric constant and conductivity of an object from measurements of reflection and refraction associated with scattering from objects. Since this involves solving ill-posed nonlinear inverse scattering problems, which are computationally expensive, especially for strong scatterers, an alternative based on the principles of ground

penetrating radar and confocal microscopy had been proposed [18] - [34]. It seeks to identify the existence and location of strong microwave scatterers in the breast. Here, we explain the basic concepts and review some major developments in the area of ultra-wideband (UWB) microwave radar imaging. In a UWB microwave imaging system, a wideband pulse is transmitted from an array of antennas located near the breast surface and then the backscattered microwave signals from malignant lesions in the breast are used to identify the presence and location of malignant tumors. The use of an UWB pulse is common to all the UWB microwave radar imaging techniques.

The confocal microwave imaging (CMI) [19][24] technique, the microwave imaging based on space-time (MIST) beamforming [26], the tissue sensing adaptive radar (TSAR) [28] and the time reversal (TR) with the FDTD method [31][32] are the major UWB microwave imaging techniques used for tumor detection and localization. The detection of small tumors using these techniques is restricted by the wavelength-related diffraction limit. Hence, of the aforementioned techniques, the TR technique has been identified as having the best qualities for the detection of sub-wavelength size tumors. On the other hand, the FDTD TR technique [31], as compared to the other methods that require electromagnetic simulations (tomography methods), has the ability to detect and determine the location of a tumor scatterer through a single time-domain simulation. One FDTD simulation required by the FDTD TR algorithm implies longer image recovery time than the CMI and TSAR techniques, which are

CHAPTER 1 INTRODUCTION

signal-extraction techniques while the FDTD TR technique is a physics-based technique.

To detect early-stage breast cancer tumors well below a centimeter with specificity and high degree of accuracy, i.e., with minimum false negatives/positives, requires novel solutions in terms of both hardware and algorithms.

1.2 OUTLINE OF THESIS

In this thesis, we approach this problem using two principles:

- 1) Modified Shannon Entropy Criterion (SEC) for determining when the time-reversed wave focuses back to the source target in the presence of an inhomogeneous lossy medium;
- 2) Phase-Shifting Mask (PSM) technology from optical lithography enabling waves from adjacent apertures to cancel diffraction effects and increase the spatial resolution with which patterns can be projected onto wafer.

We first review some relevant concepts and summarize the current state-of-the-art in the published UWB microwave imaging techniques for tumor detection and localization. Through the use of the modified Shannon entropy criteria, a novel robust time reversal technique based on the transmission-line matrix method (TLM) is developed as an alternative to [31][32]. The TLM method [35], which is the primary numerical analysis method throughout this research, is implemented in Matlab [36]. The planar system for the supine position and the cylindrical system for the prone position are implemented and the TLM TR algorithm exploiting SEC is demonstrated.

We formulate an experimental setup for achieving sub-wavelength resolution with the PSM technique for detection of breast cancer tumors. Then we incorporate the SEC in a TR algorithm to achieve a robust imaging algorithm exploiting the measurements acquired by our PSM set-up. Unlike the FDTD TR algorithm by Kosmas *et al.* [31][32] which excites one of the 23 antenna elements, we propose a system where all antennas are stimulated simultaneously with their excitation based on the PSM principle explained in chapter 4. Our sub-wavelength UWB microwave imaging technique is applied to detect a 0.5-mm diameter tumor inside a breast in the supine position. The effect of the dielectric contrast and the proximity of the tumor to the antenna receivers are examined. A TLM-based TR algorithm employing two time reversal mirrors (TRMs) is proposed to improve the accuracy of localizing the sub-wavelength tumors.

CHAPTER 1 INTRODUCTION

After that, we examine the feasibility and the design of a narrowbeam UWB antenna for microwave breast cancer detection focusing on the antenna feed structure and the printed TEM horn antenna. We conclude by suggesting future work toward hardware and practical implementation for UWB microwave radar imaging with high resolution.

Chapter 2 reviews the UWB microwave radar imaging techniques for breast cancer detection available in the literature.

Chapters 3 to 4 describe the modified Shannon Entropy (SEC) and its application to determining when the time-reversed propagating wave focuses back onto the scatterer.

Chapter 3 presents the novel robust TLM-based time reversal microwave imaging technique. The simulation required for the data acquisition model and the TR model is implemented in a two-dimensional TM-mode and is programmed using Matlab. The planar and cylindrical examples, with dielectric profile based on MRI-derived data of the breast of a 57 year old female, are used to demonstrate the advantages of the SEC as compared to the inverse varimax norm criteria. Then, the need to use a technique for detecting below the diffraction limit imposed by the UWB pulse is discussed.

In Chapter 4, we propose a sub-wavelength UWB microwave radar imaging technique [37] that incorporates SEC in a TR algorithm and the experimental setup formulated using the PSM principle. This technique is then applied to the detection of a 0.5-mm diameter tumor using a 200-ps UWB pulse.

CHAPTER 1 INTRODUCTION

The breast is in the supine position. We investigate the effect of the dielectric contrast and the depth of the tumor on the robustness of the SEC. Based on these findings, an enhanced sub-wavelength microwave imaging technique that exploits two TRMs is proposed.

In Chapter 5, we design the feed structure of an UWB antenna for microwave radar imaging. The UWB antennas are fundamental components of the UWB radar imaging hardware. The performance of the antenna is crucial for the resolution and the reliability of the whole imaging system. A TEM horn antenna is studied and suggestions are made regarding the hardware implementations of the experimental setup. In addition to the feed structure, antenna models and breast phantoms are implemented using Agilent HFSS [38]. For optimizing the feed structure, circuit models in Agilent ADS were utilized [39].

The thesis concludes with suggestions for further research. For convenience, a summary of all bibliography is given at the end of the thesis.

1.3 CONTRIBUTIONS

The author contributed substantially to the following original developments presented in this thesis:

- I. Development and formulation of the modified Shannon entropy criterion (SEC) for applications to TR algorithms. This is applicable to both TLM TR and FDTD TR algorithms.
- II. Implementation of the SEC TLM-based TR algorithm in Matlab.
- III. Development of a Demo program that generates dielectric profile of breast using MRI image data.
- IV. Implementation of a 2-D TLM model as a forward model for data acquisition.
- V. Formulation of the PSM concept in the case of UWB microwave imaging.
- VI. Development and implementation of novel experimental setup using the principle of PSM for detecting tumors of sub-wavelength size.
- VII. Development of a feed structure, breast phantom and UWB antenna models using Agilent HFSS, a commercial EM simulator, and Agilent ADS.

REFERENCES

- [1] American Cancer Society, "Cancer facts and figures 2007," Amer. Cancer Soc., Atlanta, GA, 2007.
- [2] *Mammography and Beyond: Developing Techniques for the Early Detection of Breast Cancer*. Washington, DC: Institutes of Medicine, National Academy Press, 2001.
- [3] P. T. Huynh, A. M. Jarolimek, and S. Daye, "The false-negative mammogram," *Radiograph*, vol. 18, no. 5, pp. 1137–1154, 1998.
- [4] J. G. Elmore, M. B. Barton, V. M. Mocer, S. Polk, P. J. Arena, and S. W. Fletcher, "Ten-year risk of false positive screening mammograms and clinical breast examinations," *New Eng. J. Med.*, vol. 338, no. 16, pp. 1089–1096, 1998.
- [5] E. D. Pisano, M. J. Yaffe, C. M. Kuzmiak, *Digital Mammography*, Lippincott Williams & Wilkins, Philadelphia, PA, USA 2004.
- [6] S. S. Chaudhary, R. K. Mishra, A. Swarup, and J. M. Thomas, "Dielectric properties of normal and malignant human breast tissues at radiowave and microwave frequencies," *Indian J. Biochem. Biophys.*, vol. 21, pp. 76–79, Feb. 1984.
- [7] A. J. Surowiec, S. S. Stuchly, J. R. Barr, and A. Swarup, "Dielectric properties of breast carcinoma and the surrounding tissues," *IEEE Trans. Biomed. Eng.*, vol. 35, pp. 257–263, Apr. 1988.
- [8] S. Gabriel, R. W. Lau, and C. Gabriel, "The dielectric properties of biological tissues: II. Measurements on the frequency range 10 Hz to 20 GHz," *Phys. Med., Biol.*, vol. 41, no. 11, pp. 2251–2269, Nov. 1996.
- [9] W. T. Joines, Y. Zhang, C. Li, and R. L. Jirtle, "The measured electrical properties of normal and malignant human tissues from 50 to 900 MHz," *Med. Phys.*, vol. 21, pp. 547–550, Apr. 1994.

CHAPTER 1 INTRODUCTION

- [10] P. M. Meaney and K. D. Paulsen, "Nonactive antenna compensation for fixed-array microwave imaging: Part II—Imaging results," *IEEE Trans. Med. Imag.*, vol. 18, no. 6, pp. 508-518, June 1999.
- [11] P. M. Meaney, M. W. Fanning, D. Li, S. P. Poplack, and K. D. Paulsen, "A clinical prototype for active microwave imaging for the breast," *IEEE Trans. Microwave Theory Tech.*, vol. 48, no. 11, pp. 1841-1853, Nov. 2000.
- [12] D. Li, P. M. Meaney, T. Raynolds, S. A. Pendergrass, M. W. Fanning, and K. D. Paulsen, "Parallel-detection microwave spectroscopy system for breast imaging," *Rev. Sci. Instrum.*, vol. 75, pp. 2305-2313, 2004.
- [13] S. P. Poplack, P. M. Meaney, A. Hartov, K. D. Paulsen, T. D. Torsteson, M. R. Grove, S. K. Soho, and W.A. Wells, "Electromagnetic breast imaging: Average tissue property value in women with negative clinical findings," *Radiol.*, vol. 231, no. 2, pp. 571-580, May 2004.
- [14] A. E. Souvorov, A. E. Bulyshev, S. Y. Semenov, R. H. Svenson and G. P. Tatsis, "Two-dimensional computer analysis of a microwave flat antenna array for breast cancer tomography," *IEEE Trans. Microwave Theory Tech.*, vol. 48, no. 8, pp. 1413-1415, Aug. 2000.
- [15] A. E. Bulyshev, S. Y. Semenov, A. E. Souvorov, R. H. Svenson, A. G. Nazarov, Y.E. Sizov and G. P. Tatsis, "Computational modeling of three-dimensional microwave tomography of breast cancer," *IEEE Trans. Biomed. Eng.*, vol. 48, no. 9, pp. 1053-1056, Sep. 2001.
- [16] Q. H. Liu, Z. Q. Zhang, T. T. Wang, J. A. Bryan, G. A. Ybarra, L. W. Nolte, and W. T. Joines, "Active microwave imaging I — 2-D forward and inverse scattering methods," *IEEE Trans. Microwave Theory Tech.*, vol. 50, no. 1, pp. 123-133, January 2002.
- [17] Z. Q. Zhang, Q. Liu, C. Xiao, E. Ward, G. Ybarra, and W. T. Joines, "Microwave breast imaging: 3-D forward scattering simulation," *IEEE Trans. Biomed. Eng.*, vol. 50, no. 10, pp. 1180-1189, Oct. 2003.
- [18] E. C. Fear, S. C. Hagness, P. M. Meaney, M. Okoniewski, and M. A. Stuchly, "Enhancing breast tumor detection with near field imaging," *IEEE Microwave Mag.*, vol. 3, pp. 8-56, Mar 2002.

- [19] S. C. Hagness, A. Taflove, and J. E. Bridges, "Two-dimensional FDTD analysis of a pulsed microwave Confocal system for breast cancer detection: fixed-focus and antenna-array sensors," *IEEE Trans. Biomed. Eng.*, vol. 45, no. 12, pp. 1470-1479, 1998.
- [20] S. C. Hagness, A. Taflove, and J. E. Bridges, "Three-Dimensional FDTD analysis of a pulsed microwave Confocal system for breast cancer detection: design of an antenna-array element," *IEEE Trans. Antennas Propagat.*, vol. 47, no. 5, pp. 783-791, 1999.
- [21] X. Li, S. K. Davis, S. C. Hagness, D. W. Weide and B. D. Van Veen, "Microwave imaging via space-time beamforming: experimental investigation of tumor detection in multilayer breast phantoms," *IEEE Trans. Microwave Theory Tech.*, vol. 52, pp. 1856-1865, Aug. 2004.
- [22] E. C. Fear and M. A. Stuchly, "Microwave detection of breast cancer," *IEEE Trans. Microwave Theory Tech.*, vol. 48, no. 11, pp. 1854-1863, 2000.
- [23] X. Li and S. C. Hagness, "A confocal microwave imaging algorithm for breast cancer detection," *IEEE Microwave Wireless Compon. Lett.*, vol. 11, no. 3, pp. 130-132, 2001.
- [24] E. C. Fear, X. Li, S. C. Hagness, and M. Stuchly, "Confocal microwave imaging for breast cancer detection: Localization of tumors in three dimensions," *IEEE Trans. Biomed. Eng.*, vol. 49, pp. 812-822, Aug. 2002.
- [25] E. C. Fear, J. Sill, and M. A. Stuchly, "Experimental feasibility study of confocal microwave imaging for breast tumor detection," *IEEE Trans. Microwave Theory Tech.*, vol. 51, no. 3, pp. 887-892, 2003.
- [26] E. J. Bond, S. C. Hagness, and B. D. Van Veen, "Microwave imaging via space-time beamforming for early detection of breast cancer," *IEEE Trans. Antennas Propagat.*, vol. 51, no. 8, pp. 1690-1705, 2003.
- [27] S. K. Davis, H. Tandradinata, S. C. Hagness, and B. D. Van Veen, "Ultrawideband microwave breast cancer detection: a detection-theoretic approach using the generalized likelihood ratio test," *IEEE Trans. Biomed. Eng.*, vol. 52, no. 7, 2005.

CHAPTER 1 INTRODUCTION

- [28] J. M. Sill and E. C. Fear, "Tissue sensing adaptive radar for breast cancer detection—experimental investigation of simple tumor models," *IEEE Trans. Microwave Theory Tech.*, vol. 53, pp. 3312-3319, Nov. 2005.
- [29] X. Li, S. K. Davis, S. C. Hagness, D. W. van der Weide, and B. D. Van Veen, "Microwave imaging via space-time beamforming: experimental investigation of tumor detection in multilayer breast phantoms," *IEEE Trans. Microwave Theory Tech.*, vol. 52 no. 8, pp. 1856-1865, 2004.
- [30] X. Li, E. J. Bond, B. D. Van Veen and S. C. Hagness, "An overview of ultra-wideband microwave imaging via space-time beamforming for early-stage breast-cancer detection," *IEEE Antennas Propagat. Mag.*, vol. 47, pp. 19-34, Feb. 2005.
- [31] P. Kosmas and C. M. Rappaport, "Time reversal with the FDTD method for microwave breast cancer detection," *IEEE Trans. Microwave Theory Tech.*, vol. 53, no. 7, pp. 2317-2323, July 2005.
- [32] P. Kosmas and C. M. Rappaport, "A matched-filter FDTD-based time reversal approach for microwave breast cancer detection," *IEEE Trans. Antennas and Propagat.*, vol. 54, no. 4, pp. 1257-1264, April 2006.
- [33] D. W. Winters, E. J. Bond, B. D. Van Veen, and S. C. Hagness, "Estimation of the frequency-dependent average dielectric properties of breast tissue using a time-domain inverse scattering technique," *IEEE Trans. Antennas Propagat.* Vol. 54, no. 11, November 2006.
- [34] W. Zhi, F. Chin and M. Chia, "Near Field UWB LCMV imaging for breast cancer detection with entropy based artifacts removal," in *IEEE Int. Conf. on Acoustics, Speech, and Signal Processing*, vol. 2, II-577 - II-580, May 2006.
- [35] C. Christopoulos, *The Transmission-Line Modeling (TLM) method in Electromagnetics*, Morgan & Claypool Publishers, San Rafael, CA, USA, 2006.
- [36] MATLAB™ 7.1, The MathWorks Inc., 3 Apple Hill Drive, Natick, MA, 2005.

CHAPTER 1 INTRODUCTION

- [37] D. M. Hailu, N. K. Nikolova and M. H. Bakr, "Sub-wavelength microwave radar imaging for detection of breast cancer tumors," *in 2007 IEEE Int. Microwave Symp. on Signals, Systems, and Electronics*, pp.107-110, Montréal, Canada, July 2007.
- [38] Ansoft HFSS ver. 10.1, Ansoft Corporation, 225 West Station Square Drive, Suite 200, Pittsburgh, PA 15219 USA, 2006.
- [39] Agilent ADS, Agilent Technologies, 1400 Fountaingrove Parkway, Santa Rosa, CA 95403-1799, USA.

CHAPTER 2

REVIEW: ULTRAWIDEBAND MICROWAVE RADAR IMAGING TECHNIQUES FOR BREAST CANCER DETECTION [1]

2.1 CONFOCAL MICROWAVE IMAGING (CMI)

Hagness *et al.* [2], [3] first proposed confocal microwave imaging (CMI) for breast cancer detection. They based their findings on numerical modelling and the principles of confocal microscopy. A planar CMI system for patients in the supine position and cylindrical CMI system for patients in the prone position have been presented and analyzed for localization of tumors in three dimensions [4] - [6]. The CMI technique is simple and avoids the complexity of microwave tomography, which involves solutions of ill-posed nonlinear inverse scattering problems. CMI does not construct exact permittivity and conductivity profiles nor does it find the exact shape of the tumor, but rather attempts to image strong scattering focal points. Analogous to ground penetrating radar, CMI involves

CHAPTER 2 REVIEW: ULTRA-WIDEBAND MICROWAVE RADAR IMAGING TECHNIQUES FOR BREAST CANCER DETECTION

illuminating the breast with an ultra-wideband pulse from a number of antenna locations. Then recorded reflections are synthetically focused within the breast tissue. The detection of malignant tumors is achieved by the coherent addition of signal returns from strongly scattering objects within the breast.

2.1.1 CMI Focusing Algorithm [6]

At each antenna position, the antenna is excited with an ultra-wideband (UWB) pulse such as the differentiated Gaussian [6]:

$$V(t) = V_o(t - t_o)e^{-(t-t_o)^2/\tau^2} \quad (2.1)$$

where V_o is used to adjust the amplitude of the pulse. In [6], $\tau = 62.5$ ps, $t_o = 4\tau$ and (2.1) has full-width half-maximum (FWHM) of 0.17 ns in time and approximately 6 GHz in frequency, with maximum spectral content near 4 GHz. The current (magnetic field) at the antenna feed for planar configuration is recorded because a resistively loaded bowtie antenna scans over the surface of the naturally flattened breast. For the cylindrical configuration, the voltage (electric field) is recorded because a resistively loaded dipole antenna scans around the breast. The signals recorded after the excitations contain the backscattered signals from the breast.

Fig. 2.1 demonstrates the illumination of the breast model with an UWB pulse with the tumor inside the breast. Letting the same antenna receive and transmit, the early-time response, which contains the incident pulse, and the late-time

CHAPTER 2 REVIEW: ULTRA-WIDEBAND MICROWAVE RADAR IMAGING TECHNIQUES FOR BREAST CANCER DETECTION

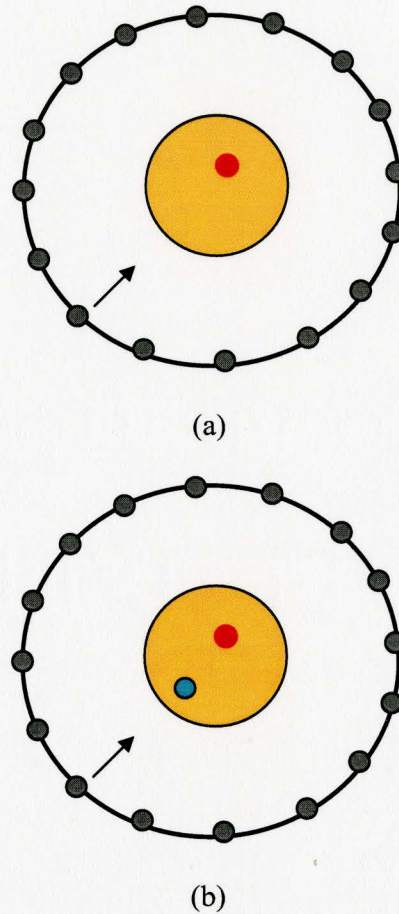


Fig. 2.1 CMI involves illuminating the breast with an ultra-wideband pulse from a number of physical antenna locations. (a) Breast model with tumor. (b) Focal point in the breast model.

response, which contains tumor backscatter and backscatter due to clutter, are in the recorded waveform. Next we consider the CMI focusing algorithm.

CHAPTER 2 REVIEW: ULTRAWIDEBAND MICROWAVE RADAR IMAGING TECHNIQUES FOR BREAST CANCER DETECTION

The steps involved in the CMI technique for image formation are (see Fig. 2.1) :

Measurement Stage

- Step 1* Excite each antenna element of an N -element antenna array, one at a time, using an UWB pulse.
- Step 2* Store backscattered pulse responses at the N receiving antennas for each excitation location.

Post-Processing Stage

- Step 1* Select a focal point within the imaging range - P_j .
- Step 2* Select a transmitter antenna - T_i .
- Step 3* Using the velocity of propagation in the coupling medium, which is known, determine the propagation time from the transmitting antenna to the focal point and back to the receiver.
- Step 4* The N individual backscatter waveforms are time-shifted accordingly to achieve coherent sum of backscattered responses at the desired focal point P_j .
- Step 5* Repeat for all transmitting antennas T_i ($i = 1, \dots, N$) to obtain total backscattered response at desired focal point P_j .
- Step 6* Repeat for all focal points in the image.

The preceding formulation did not include some additional steps involved in the image formation. Signal processing techniques are used to reduce the early-time content, and to selectively enhance the tumor response while suppressing clutter. The early-time clutter is much greater in magnitude than the

CHAPTER 2 REVIEW: ULTRAWIDEBAND MICROWAVE RADAR IMAGING TECHNIQUES FOR BREAST CANCER DETECTION

tumor response and has to be removed to permit reliable detection of tumors in the reconstructed images.

To form the image, the distances from each antenna to the focal point are computed and converted into time delays as in *Step 3* of the post-processing stage. Then the time delays are used to identify the input from each processed signal. All contributions are summed and the squared value of this sum is assigned to the pixel value at the focal point. The intensity value I of the pixel at the location \mathbf{r} is assigned as [6]

$$I(\mathbf{r}) = \left[\sum_{n=1}^N B_n(\tau_n(\mathbf{r})) \right]^2 \quad (2.2)$$

where B_n is the post-processed backscatter waveform at the n th antenna located

at \mathbf{r}_n and $\tau_n(\mathbf{r}) = \frac{2|\mathbf{r} - \mathbf{r}_n|}{v\Delta t}$ is the discrete time delay in number of time steps

from the n th antenna to the synthetic focal point at \mathbf{r} . Here, v is the approximate velocity of propagation of the signal in the medium, calculated by assuming that the breast tissue is homogeneous. There is on-going research on estimating the dielectric properties of the skin and the dispersive heterogeneous breast tissue for more accurate calculation of the velocity of propagation.

CHAPTER 2 REVIEW: ULTRAWIDEBAND MICROWAVE RADAR IMAGING TECHNIQUES FOR BREAST CANCER DETECTION

2.1.2 Calibration Step: Skin Reflection Clutter Removal Approach

The early-time content of the signal in a monostatic arrangement consists of the UWB pulse radiated by the antenna, some noise and the reflected signal from the skin. The calibration step attempts to remove the latter signals known as clutter. The calibration procedure is approximate and based on assuming that the signals recorded at various antenna locations have comparable incident pulse and skin reflections. In the planar system, the calibration involves taking the average of the reflected current response at each antenna in a row, and subtracting the averaged value from the response at each antenna in the same row. The planar antenna array has its elements arranged in rows and columns.

In the cylindrical system, the incident pulse from the antenna and the skin reflections are uncorrelated and separated in time. The skin-reflection signal is a voltage obtained by subtracting the incident signal from the total reflected one in the time domain and then aligned in time through shifting. Then the average of the aligned skin reflection signals from the antennas in a row is subtracted from the recorded waveform of each antenna.

2.1.3 Integration Step

The integration step identifies the magnitude of the scattered signal at the receiving antenna corresponding to the propagation time. The calibrated signals from each antenna are integrated in time. Since the differentiated Gaussian excitation signal (2.1) has a zero-crossing at its central point in time, the

CHAPTER 2 REVIEW: ULTRAWIDEBAND MICROWAVE RADAR IMAGING TECHNIQUES FOR BREAST CANCER DETECTION

backscattered signal that follows after a specific time delay corresponding to the round-trip distance between the antenna and the scatterer would also have a zero-crossing at its centre point.

After integration, the time shifted signal would have a maximum at the centre point, allowing for the coherent addition of local maxima.

2.1.4 Compensation Step

The goal of the compensation step is to counterbalance losses because of conductivity in the breast tissue and isotropic radiation. The compensation step is an approximate procedure. To estimate the compensation factors for the planar system in [6], an antenna is immersed in the FDTD homogeneous lossy medium modelling the breast tissue. It is excited with the signal (2.1), and the electric field magnitudes are calculated and recorded at points along a line perpendicular to the antenna. These values are linearly interpolated to estimate the total radial spreading and the ohmic loss at certain distances from the antenna.

In the cylindrical system, the radial spread is estimated by a $1/r$ model, where r is the distance from the antenna. The ohmic loss compensation for the cylindrical system causes amplification of the clutter due to the heterogeneities in the breast. Therefore, it is neglected [6]. Compensation factors and propagation distance corresponding to each time step in the processed signals are computed and applied.

2.1.5 Discussion of Advantages and Disadvantages

The advantage of the CMI is the simplicity of its post-processing algorithm. It has been experimentally proven to be a potentially useful tool for detecting and localizing small breast tumors in three dimensions.

The design of the antenna array element is a primary concern for all UWB microwave imaging techniques. In [3], the design of a resistively-loaded bowtie antenna element of a confocal antenna array was discussed and its EM pulse radiation and reflection characteristics within a homogeneous half-space model of a breast were presented. After studying the dynamic range of a CMI system and the shape properties of malignant tumors, it was concluded that “the dynamic range of a sensor array comprised of such antenna elements in conjunction with existing microwave equipment is adequate to detect small cancerous tumors usually missed by X-ray mammography” [3].

The disadvantages of CMI include the lack of capability to compensate for frequency-dependent propagation effects. Particularly, the weaknesses of CMI are in the calibration and compensation steps. The CMI technique assumes that the signals recorded at various antenna locations have comparable incident and skin backscattered fields. It also assumes that the breast tissue is homogeneous or can be modeled by an averaged uniform dielectric constant and conductivity. Due to these assumptions, it has limited ability to segregate against spurious reflections and noise, and limited robustness to uncertainties in the shape of the signal occurring because of variations in tumor size and shape.

CHAPTER 2 REVIEW: ULTRAWIDEBAND MICROWAVE RADAR IMAGING TECHNIQUES FOR BREAST CANCER DETECTION

With respect to the antenna design, it assumes that there is no coupling between the antenna elements. There is a need to determine the optimal number of antenna elements in the array to detect the tumor response. A realistic design, however, must include the effects of the antenna mutual coupling, the clutter and the distortion. The detection of smaller and deeper tumors especially near the chest wall is difficult due to strong reflection from the chest wall muscle. Performance measures have been developed to evaluate and investigate tumor detection and localization. The within-breast signal-to-clutter (SC) ratio and the between-breast SC ratio have been developed and used in [6]. The within-breast SC ratio compares the “maximum tumor response with maximum clutter response in the same image,” and the between-breast SC ratio “compares the maximum tumor response with the pixel intensity at the same location in the image formed without a tumor present” [6]. Additional statistical measures supplement these performance ratios.

2.2 MICROWAVE IMAGING VIA SPACE-TIME (MIST)

BEAMFORMING

Microwave imaging via space-time (MIST) was proposed by Bond *et al.* [7] to improve upon some limitations of the CMI algorithms which include:

- Limited capacity to compensate for frequency-dependent propagation effects.
- Limited capacity to segregate against artifacts and noise.
- Assumption that the signals recorded at various antenna locations have comparable incident and skin backscattered fields.
- Assumption that the breast tissue is homogeneous.
- Uncertainty in the shape of the signal due to variations in the tumor size and shape.

Similar to CMI, each antenna in an array transmits a low-power UWB pulse into the breast and the backscattered signals are recorded. The beamformer is a signal processor used with the antenna array to yield a weighted combination of the signals from the antennas [8]. It assumes that each antenna element transmits sequentially. The aim of beamforming is to separate signals that have the same frequency content but are from different locations in space. An adaptive beamformer adjusts these weights in response to backscattered signal at the antennas to optimize its spatial response [8][9]. Therefore, it facilitates suppression of interference noise and clutter due to the heterogeneity of the breast

CHAPTER 2 REVIEW: ULTRA WIDEBAND MICROWAVE RADAR IMAGING TECHNIQUES FOR BREAST CANCER DETECTION

tissue. The MIST beamforming technique uses a class of beamformers called minimum variance beamformer because the weights are chosen so that to the beamformer output variance. Thus, unlike CMI, the beamformer focuses the recorded reflected signals from each antenna in space.

The MIST beamformer does this by time shifting the recorded signals to align with reflections from an assumed possible scatterer at a nominee location. A nominee location is a focal point within the breast tissue. The recorded reflected signal at each antenna is assumed to pass through a single unique communication channel (medium) for each nominee location within the breast. Physically, the channel is the medium from the antenna to the nominee location with averaged dielectric properties or averaged speed of propagation. After the alignment, for each antenna channel, the time-aligned recorded signal is passed through a finite-impulse response (FIR) filter. Then the signal is summed with the signals from the other channels to produce the beamformer output, which is timed using a window function to the time interval of the reflected signal from the nominee location, and recalculated in the form of an energy signal.

FIR filters work by multiplying an array of L data samples by an array of L tap coefficients and summing the elements of the resulting array. L is the filter length. The FIR filters here act as bandpass filters and are designed to maximize the output signal-to-noise ratio. The bank of FIR filters allow the boosting of backscattered signals originating from the nominee location while attenuating

CHAPTER 2 REVIEW: ULTRAWIDEBAND MICROWAVE RADAR IMAGING TECHNIQUES FOR BREAST CANCER DETECTION

those associated with the undesired frequency ranges and other locations. It is important to note that increasing the filter length results in better stopband attenuation and steeper rolloff.

The energy intensity is plotted as a function of location providing an image for the nominee location. If a strong scatterer exists at the nominee location, a relatively bright intensity is shown at the corresponding pixels.

2.2.1 MIST Beamforming Algorithm

The space-time beamformer designed for each scan location \mathbf{r}_0 makes a signal that is a weighted combination of time-delayed recorded received signals after skin-artifact removal. The image of the backscattered energy $\xi(\mathbf{r})$ is obtained by applying a space-time beamformer to each location and obtaining $\xi(\mathbf{r}_0)$ for each antenna channel. Fig. 2.2 shows the process for the received signal $x_i[n]$ in the i th antenna channel.

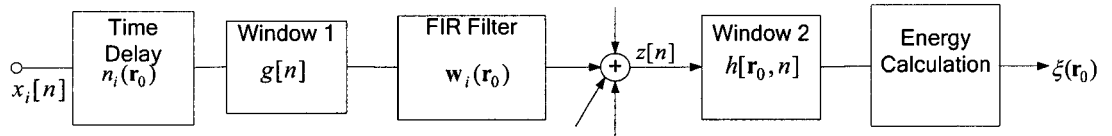


Fig. 2.2 Illustration of the MIST beamforming process [7] for nominee location \mathbf{r}_0 for the i th antenna channel.

The antenna channel involves propagation through heterogeneous breast and skin medium from the antenna to the scatterer at \mathbf{r}_0 and back. The

CHAPTER 2 REVIEW: ULTRAWIDEBAND MICROWAVE RADAR IMAGING TECHNIQUES FOR BREAST CANCER DETECTION

beamformer passes backscattered signals from \mathbf{r}_0 while attenuating signals from other locations. $S_{ii}(\mathbf{r}_0, \omega)$ is defined as an analytical model of the monostatic frequency response associated with propagation through the i th antenna channel, which is related to the Fourier transform of the skin-artifact removed signal. The assumption is made because each antenna acts as both a receiver and a transmitter at the same location. In such a system, surfaces of constant waves are spheres centered at the antenna element. As seen in Fig. 2.2, the signal $x_i[n]$ is then delayed by an integer number of time samples [7]:

$$n_i(\mathbf{r}_0) = n_a - \tau_i(\mathbf{r}_0) \quad (2.3)$$

where $\tau_i(\mathbf{r}_0)$ is the roundtrip propagation delay in number of time steps for the location \mathbf{r}_0 in the i th channel, and n_a is the reference discrete time to which the recorded backscattered signals are aligned after skin-artifact removal. The roundtrip propagation delay is computed by dividing the roundtrip path length by the average speed of propagation and rounding. Thus, there is a need to accurately determine average speed of propagation in the propagation model. In [7], n_a is chosen as the worst case delay throughout all locations and channels.

The signals are then windowed to remove clutter that is present prior to n_a . The window function for Window 1 shown in Fig. 2.2 is [7]

$$g[n] = \begin{cases} 1, & n \geq n_a \\ 0, & \text{otherwise.} \end{cases} \quad (2.4)$$

CHAPTER 2 REVIEW: ULTRA WIDEBAND MICROWAVE RADAR IMAGING TECHNIQUES FOR BREAST CANCER DETECTION

The next step in the process seen in Fig. 2.2 is the filtering stage using the FIR filters to equalize attenuation and dispersion. Before passing the signal through a bandpass filter, any fractional time delays remaining in the backscattered tumor responses after alignment with discrete time n_a have to be interpolated. The filter bank serves to isolate different frequency components in the signal.

The Fourier transform of the signal $x_i[n]$ is defined as [7]

$$X_i(\omega) = I(\omega)S_{ii}(\mathbf{r}_0, \omega), \quad 1 \leq i \leq N \quad (2.5)$$

where N is the number of antennas and $I(\omega)$ is the Fourier transform of the transmitted UWB pulse. In Fig. 2.2, the FIR filter in the i th channel has coefficients $\mathbf{w}_i = [w_{i0}, w_{i1}, \dots, w_{i(L-1)}]^T$, where L is filter length. The filter response is [7]

$$W_i(\omega) = \sum_{m=0}^{L-1} w_{im} \exp(-j\omega m T_s) = \mathbf{w}_i^T \mathbf{d}(\omega), \quad 1 \leq i \leq N \quad (2.6)$$

where T_s is the sampling interval and $\mathbf{d}(\omega) = [1, e^{-j\omega T_s}, \dots, e^{-j\omega(L-1)T_s}]^T$. The design requirement on the weights \mathbf{w}_i^T is that the signals from a location \mathbf{r}_0 must have unit gain and linear phase shift.

CHAPTER 2 REVIEW: ULTRA WIDEBAND MICROWAVE RADAR IMAGING TECHNIQUES FOR BREAST CANCER DETECTION

This is done using the following constraint [7]

$$\sum_{i=1}^N S_{ii}(\mathbf{r}_0, \omega) W_i(\omega) \exp(-j\omega n_i(\mathbf{r}_0)) = \sum_{i=1}^N \tilde{S}_{ii}(\mathbf{r}_0, \omega) \mathbf{w}_i^T \mathbf{d}(\omega) \approx \exp(-j\omega T_s(L-1)/2) \quad (2.7)$$

where $\tilde{S}_{ii}(\mathbf{r}_0, \omega)$ is the frequency response found by removing linear phase shift due to round trip propagation delay $\tau_i(\mathbf{r}_0)$. The average time delay due to the FIR filter is $T_s(L-1)/2$. Once constraint (2.7) is satisfied, the output $z[n]$ has Fourier transform given by [7]

$$Z(\omega) = I(\omega) \exp\{-j\omega[T_s(L-1)/2 + n_a]\}. \quad (2.8)$$

As seen in Fig. 2.2, using Window 2, $z[n]$ is windowed to eliminate additional clutter. The energy is calculated as follows [7]

$$\xi(\mathbf{r}_0) = \sum_n |z[n]h[\mathbf{r}_0, n]|^2 \quad (2.9)$$

where $h(\mathbf{r}_0, n)$ is the window. Finally, the beamformer output energy is plotted as a function of location after scanning throughout the breast model.

2.2.2 FIR Filter and Window Design [7]

We may rewrite (2.7) as [7]

$$\begin{bmatrix} \mathbf{w}_1^T, \dots, \mathbf{w}_N^T \end{bmatrix}^T \begin{bmatrix} \tilde{S}_{11}(\mathbf{r}_0, \omega) \mathbf{d}(\omega) \\ \tilde{S}_{22}(\mathbf{r}_0, \omega) \mathbf{d}(\omega) \\ \vdots \\ \tilde{S}_{NN}(\mathbf{r}_0, \omega) \mathbf{d}(\omega) \end{bmatrix} = \mathbf{w}^T \mathbf{d}(\mathbf{r}_0, \omega) \approx \exp(-j\omega T_s(L-1)/2) \quad (2.10)$$

CHAPTER 2 REVIEW: ULTRAWIDEBAND MICROWAVE RADAR IMAGING TECHNIQUES FOR BREAST CANCER DETECTION

where the weight vector is $N \cdot L \times 1$. The filters are designed by approximating (2.10) on a dense grid of M distinct frequencies across the band. The matrix containing the $\mathbf{d}(\mathbf{r}_0, \omega)$ at each of these frequencies is

$$\mathbf{A} = [\mathbf{d}(\mathbf{r}_0, \omega_1), \dots, \mathbf{d}(\mathbf{r}_0, \omega_M)]. \quad (2.11)$$

The right-hand side of (2.10) for the M frequencies becomes

$$\mathbf{f}_d = [\exp(-j\omega_1 T_s (L-1)/2), \dots, \exp(-j\omega_M T_s (L-1)/2)]. \quad (2.12)$$

A robust beamformer is designed by solving the penalized least squares problem

$$\min_{\mathbf{w}} \left\{ \|\mathbf{w}^T \mathbf{A} - \mathbf{f}_d\|_2^2 + \lambda \|\mathbf{w}\|_2^2 \right\} \quad (2.13)$$

where λ is the regularization parameter. Regularization is needed to control the noise gain if \mathbf{A} is ill-conditioned and to reduce the norm, which can cause the gain at locations other than \mathbf{r}_0 to amplify noise.

For the window design, Bond *et al.* [7] assume a point scatterer model, because of the interest in detecting very small tumors. If (2.7) is satisfied, and given the point scatterer assumption, then $z[n]$ is a time-shifted, attenuated, and sampled version of the transmitted UWB pulse. The choice of the window that reduces clutter by only considering samples of $z[n]$ containing the backscattered tumor energy (2.9) is [7]

$$h[\mathbf{r}_0, n] = \begin{cases} 1, & n_l \leq n \leq n_h \\ 0, & \text{otherwise} \end{cases} \quad (2.14)$$

CHAPTER 2 REVIEW: ULTRA WIDEBAND MICROWAVE RADAR IMAGING TECHNIQUES FOR BREAST CANCER DETECTION

where the backscattered signal occupies discrete time space n_l through n_h in $z[n]$.

In practice, the tumor is not a point scatterer and due to the frequency-dependence of the scattering, the recorded backscattered signal is a distorted version of the UWB pulse. The duration of the backscattered signal is increased because of dispersion and due to the increasing complexity of window selection. Investigations in [7] indicate that the duration of the backscattered signal is proportional to tumor size.

2.2.3 Discussion of Advantages and Disadvantages

The MIST beamforming algorithm is robust to variations in assumed and actual average dielectric properties. However, as mentioned in Table 2.1, the propagation model uses the average speed of propagation. Thus, the accuracy of the averaged frequency-dependent dielectric properties is vital for optimum performance. It also takes into account the frequency-dependent propagation effects. In addition, the MIST beamforming algorithm along with the skin-artifact removal method removes skin-artifact clutter at the expense of distorting the tumor signal.

To eliminate distortion, a near-field UWB linear constraint minimum variance (LCMV) beamforming technique is proposed by Zhi *et al.* [10]. LCMV beamforming with entropy removes artifacts by using an entropy function. The

CHAPTER 2 REVIEW: ULTRAWIDEBAND MICROWAVE RADAR IMAGING TECHNIQUES FOR BREAST CANCER DETECTION

entropy measures the variation or similarity of the signals from the different antennas at a specified time. An entropy function similar to the one used in [11] is defined to measure the similarity of the different antenna signals. Similar artifacts in the early-time response from the antenna elements results in higher entropy. A window function is designed to eliminate similar artifacts at all antennas.

CHAPTER 2 REVIEW: ULTRA WIDEBAND MICROWAVE RADAR IMAGING
TECHNIQUES FOR BREAST CANCER DETECTION

TABLE 2.1
COMPARISON OF UWB MICROWAVE RADAR IMAGING TECHNIQUES

| Technique | Accounts for Variability in Breast Tissue Heterogeneities | Dispersion Model for Breast Tissue | Algorithm Employed | Drawbacks / Trade-offs |
|---------------------------|---|--|---|---|
| <i>CMI</i> | No, assumes that breast is homogeneous with an averaged dielectric constant and conductivity for the propagation model. | None* | Simple time-shift and summing technique | <ul style="list-style-type: none"> • Does not compensate for frequency-dependent propagation effects • Assumes breast tissue is homogeneous. |
| <i>MIST Beamforming</i> | <p>Yes, assume each antenna channel has unique backscattered field due to tumor at a certain location.</p> <p>Compensates for frequency-dependent propagation effects.</p> <p>But MIST is robust to deviation between assumed and actual average dielectric properties.</p> | <p>Uses frequency-dependent propagation model.</p> <p>In [12], TDIS algorithm updates MIST to find optimum average breast tissue Debye model parameters.</p> | Minimum variance Space-time Beamformer | <ul style="list-style-type: none"> • Propagation model uses the average speed of propagation so accuracy in estimation of average dielectric properties is vital for optimum performance. • Dispersive effects increase the duration of the backscattered signal complicating window selection. • Assumes the received signal in the ith channel only contains backscatter due to lesion at location \mathbf{r}_0. |
| <i>Time-Reversal FDTD</i> | Achieves focusing without prior knowledge of breast tissue properties, and is robust to breast inhomogeneities. | None | TR Technique | <ul style="list-style-type: none"> • Not proved experimentally • Assumes linearization in inverse scattering problem • Depends on skin-clutter removal. |

*Uses the single-pole Debye model for the proof of concept forward model used in simulations.

2.3 TIME REVERSAL WITH THE FDTD METHOD

As an alternative to the CMI and MIST, Kosmas *et al.* [11][13] proposed a tumor detection and localization technique based on the principles of time reversal (TR) with the finite-difference time-domain (FDTD) method. The advantages of the TR FDTD compared to the CMI and MIST methods are:

- Compensates for path loss due to lossy breast medium.
- The TR scattered field focuses back to the tumor even when the properties of the background medium are only approximately known. An approximate averaged value of the permittivity of the propagation medium would suffice to achieve convergence.
- Omitting the skin layer and the breast heterogeneities from the TR mirror (TRM) breast model does not affect significantly the focusing of the wave back to the tumor.
- Assumes the tumor acts as a point scatterer.
- The TR medium for the approximate TRM breast model does not model dispersion; instead, a smaller taper parameter is used to offset the effects of dispersion.

A time-reversal mirror (TRM) comprises an array of receivers where a single UWB pulse excitation is used for the focusing to resolve small tumors [11]. It is shown that the tumor acts as a point scatterer, which introduces an amplitude scaling and time delay to the shape of the total reflected field. The key

CHAPTER 2 REVIEW: ULTRAWIDEBAND MICROWAVE RADAR IMAGING TECHNIQUES FOR BREAST CANCER DETECTION

assumption is that the scatterer is treated as a point source and the nonlinear inverse scattering problem is reduced to a linear inverse scattering problem, assuming no multiple scattering. The aim is to localize the point source with no information on the size or shape of the tumor, and to recover it from a simple application of the TR process. This is also the case for other UWB microwave radar imaging techniques.

The TR method may be cast in the framework of the distorted-wave Born approximation (DWBA) [13][14][17]. The DWBA method described in [15][16][17] originates from the concept of expressing the scattering potential as the sum of the known background and a small perturbation or deviation, which is to be determined. This is because:

- the TR model is assumed homogeneous with a single scatterer in the breast medium [18];
- the TLM TR simulation takes into account both dielectric polarization current and conduction current; these are treated independently and disregarding dispersion in the medium permittivity and conductivity.

The DWBA approximation is a single-scattering approximation, where the scattered field amplitude is a linear functional of the object $O(\mathbf{r}) = k^2(\mathbf{r}) - k_b^2(\mathbf{r})$. Fig. 2.3 shows an example of an inverse scattering experiment. In this experiment, the measurement data are obtained at \mathbf{r} on S with the transmitter at

CHAPTER 2 REVIEW: ULTRAWIDEBAND MICROWAVE RADAR IMAGING TECHNIQUES FOR BREAST CANCER DETECTION

$\hat{\mathbf{r}}$. From Fig. 2.3, the EM scattering problem can be formulated as the solution of the volume integral equation [16]

$$\mathbf{E}(\mathbf{r}) = \mathbf{E}_{inc}(\mathbf{r}) + \int_V d\mathbf{r}' \bar{\mathbf{G}}(\mathbf{r}, \mathbf{r}', \varepsilon_b) \cdot [k^2(\mathbf{r}') - k_b^2(\mathbf{r}')] \mathbf{E}(\mathbf{r}'). \quad (2.15)$$

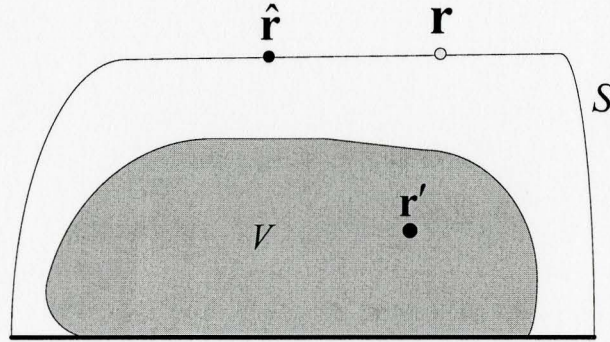


Fig. 2.3 An inverse scattering experiment where the measurement data are obtained at \mathbf{r} on S and the transmitter is at $\hat{\mathbf{r}}$ [16].

where ε_b , and $k_b^2 = \omega^2 \mu \varepsilon_b$ are the permittivity and wave number of the background, and $k^2(\mathbf{r}') = \omega^2 \mu \varepsilon(\mathbf{r}')$ is the wavenumber of the scatterer, which is the function to be sought. The integral in (2.15) is the contribution to the field \mathbf{E} from the volume current induced in the scatterer by the total electric field \mathbf{E} , or generated by the displacement current and conduction current due to conductivity of scatterer. The volume integral equation method was developed in 1913 by Esmarch for finding scattering solution of a bounded highly inhomogeneous medium [16][17].

CHAPTER 2 REVIEW: ULTRA WIDEBAND MICROWAVE RADAR IMAGING TECHNIQUES FOR BREAST CANCER DETECTION

The incident field $\mathbf{E}_{inc}(\mathbf{r})$ is the field present in the absence of the scatterer or when $k^2(\mathbf{r}) = k_b^2(\mathbf{r})$. In (2.15), $\bar{\mathbf{G}}(\mathbf{r}, \mathbf{r}', \varepsilon_b)$ is the dyadic Green's function, which is the solution of [16]

$$\nabla \times \nabla \times \bar{\mathbf{G}}(\mathbf{r}, \mathbf{r}', \varepsilon_b) - k_b^2 \bar{\mathbf{G}}(\mathbf{r}, \mathbf{r}', \varepsilon_b) = \bar{\mathbf{I}} \delta(\mathbf{r} - \mathbf{r}'). \quad (2.16)$$

Since in the inverse scattering problem, the measurement data are available only outside the scatterer, we can only have

$$\mathbf{E}_{sca}(\mathbf{r}) = \mathbf{E}(\mathbf{r}) - \mathbf{E}_{inc}(\mathbf{r}), \quad \mathbf{r} \in S \quad (2.17)$$

where S is some surface outside V .

The only knowledge we have about the scatterer is the scattered field $\mathbf{E}_{sca}(\mathbf{r})$ and we write it from (2.15) as [16]

$$\mathbf{E}_{sca}(\mathbf{r}) = \int_V d\mathbf{r}' \bar{\mathbf{G}}(\mathbf{r}, \mathbf{r}', \varepsilon_b) \cdot [k^2(\mathbf{r}') - k_b^2(\mathbf{r}')] \mathbf{E}(\mathbf{r}'), \quad \mathbf{r} \in S. \quad (2.18)$$

This integral equation cannot be used to solve for $k^2(\mathbf{r}')$ since $\mathbf{E}(\mathbf{r}')$ is unknown.

In addition, $\mathbf{E}(\mathbf{r}')$ is a function of $k^2(\mathbf{r}')$ so the integral is a non-linear function of

$k^2(\mathbf{r}')$. The nonlinear dependence of the scattered field on $O(\mathbf{r}') = k^2(\mathbf{r}') - k_b^2(\mathbf{r}')$

is due to the mutual interactions between the induced polarization currents. This

is also a multiple scattering effect. Letting $\mathbf{E}(\mathbf{r}') = \mathbf{E}_{inc}(\mathbf{r}')$ linearizes the problem

and (2.18) becomes [16]

$$\mathbf{E}_{sca}(\mathbf{r}) = \int_V d\mathbf{r}' \bar{\mathbf{G}}(\mathbf{r}, \mathbf{r}', \varepsilon_b) \cdot [k^2(\mathbf{r}') - k_b^2(\mathbf{r}')] \mathbf{E}_{inc}(\mathbf{r}'), \quad \mathbf{r} \in S. \quad (2.19)$$

which is linear in $k^2(\mathbf{r}') - k_b^2(\mathbf{r}')$.

Since the TR algorithm attempts to localize the scatterer by considering it as a point source, full recovery of $k^2(\mathbf{r}')$ is not possible using time reversal. Due to the high contrast of the tumor with respect to the normal breast tissue, the forward model does not contradict the validity of the DWBA approximation, and $k^2(\mathbf{r}') - k_b^2(\mathbf{r}')$ in (2.19) is nonzero for an arbitrarily small region around the tumor.

2.3.1 FDTD TR Algorithm

Fig. 2.4 and Fig. 2.5 illustrate the TR procedure. Fig. 2.4 is a schematic of the FDTD model that represents a breast medium of some irregular shape. The shape of the breast and its medium are complex and are derived from a realistic MRI data as described in the next chapter.

CHAPTER 2 REVIEW: ULTRA WIDEBAND MICROWAVE RADAR IMAGING TECHNIQUES FOR BREAST CANCER DETECTION

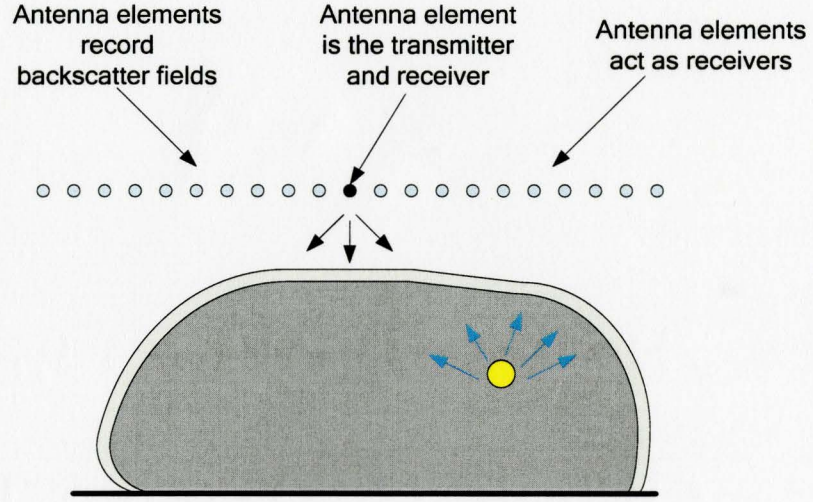


Fig. 2.4 The inputs to the TR system [11] are the backscattered fields from the tumor and clutter recorded by the antenna receivers in the forward model. The time reversal mirror (TRM) has antenna element 11 as a transmitter. Antenna element 11 transmits a pulse and all the others including element 11 record the backscattered fields.

The backscattered electric field signals from a number of antennas are recorded after transmission from one antenna. The input signal for backpropagation at each receiver is [13]

$$g_i(t) = E_x(y_i, z_i) \cdot \exp \left(- \left(\frac{t - t_p}{\nu} \right)^2 \right) \quad (2.20)$$

where t_p is the peak time at which the received wave $E_x(y_i, z_i)$ has maximum for a short pulse excitation, and ν is the taper parameter, which reduces pulse spread and width of the impulse window function.

CHAPTER 2 REVIEW: ULTRAWIDEBAND MICROWAVE RADAR IMAGING TECHNIQUES FOR BREAST CANCER DETECTION

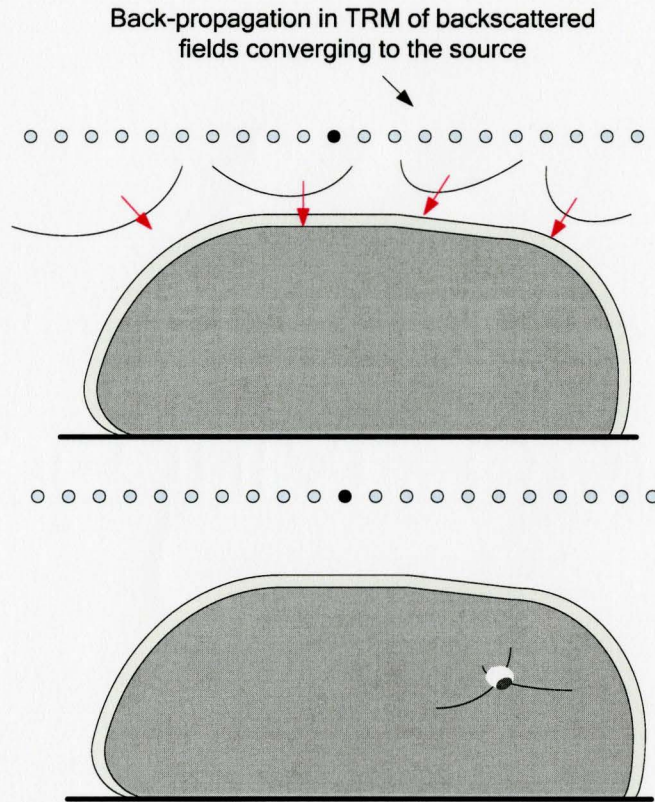


Fig. 2.5 Backpropagation starts from the fields at the antennas and the wave progressively converges to the scatterer at certain optimal time, and then diverges again. The tumor response is found at the peak (shown in white), which occurs at the optimal time.

In a simulation using time-reversed FDTD equations, it was shown in [19] that if a point source radiates in free space and time-reversed FDTD equations are applied to all points in the grid, the wave will converge back to the source at time corresponding to the maximum of the initial excitation. This is explained by the space-time matched filtering achieved by the TR mirror [11][20]. Fig. 2.5 shows

CHAPTER 2 REVIEW: ULTRA WIDEBAND MICROWAVE RADAR IMAGING TECHNIQUES FOR BREAST CANCER DETECTION

backpropagation waves starting from the fields at the antennas and progressively converging to the scatterer at certain optimal time for a known background.

If the background medium is unknown and causes uncertainties, this procedure can cause a false image and so another evaluation method is required. When the wave focuses back to the source, it is possible to produce a sharp and intense image at the target and small intensity away from it. The measure of how fast the intensity goes from peak to small values is entropy. So a minimum entropy criterion is employed in [11][13] for a 2-D problem based on the inverse varimax norm,

$$R(E_x^n) = \frac{\left[\sum \sum_{j,k} E_x^{n2}(j,k) \right]^2}{\sum \sum_{j,k} E_x^{n4}(j,k)} \quad (2.21)$$

where n is the time step of the TR algorithm, (j, k) are the grid cell coordinates, and summation is done over the domain of the breast. This approach guarantees a focused image but introduces small localization errors and hence is used sparingly where the simpler measures are unsuccessful.

The derivation of the time-reversed FDTD equations uses the TR transformation $t' = -t$ and the following equalities hold [11]:

$$\begin{aligned} \rho(t') &= \rho(t) \\ \mathbf{E}(t') &= \mathbf{E}(t) \\ \mathbf{B}(t') &= -\mathbf{B}(t) \\ \mathbf{J}(t') &= -\mathbf{J}(t) \end{aligned} \quad (2.22)$$

The electric field for the TM_x case in FDTD can be written [13]

CHAPTER 2 REVIEW: ULTRA WIDEBAND MICROWAVE RADAR IMAGING TECHNIQUES FOR BREAST CANCER DETECTION

$$E_x^{n'+1/2}(j, k) = E_x^{n'-1/2}(j, k) - \frac{\Delta t}{\epsilon \Delta x} \left\{ H_z^{n'}\left(\frac{j+1}{2}, k\right) - H_z^{n'}\left(\frac{j-1}{2}, k\right) \right. \\ \left. - H_y^{n'}\left(j, \frac{k+1}{2}\right) + H_y^{n'}\left(j, \frac{k-1}{2}\right) \right. \\ \left. + \sigma \Delta x E_x^{n'+1/2}(j, k) \right\} \quad (2.22)$$

where $\Delta x = \Delta y = \Delta$ is the grid spacing and Δt is the time step. Here the permittivity and conductivity values are for the nondispersive TR medium at some central frequency. The backpropagated equations have the next discrete time step $n' + 1/2$ which is the previous time step in forward propagation. The TR algorithm employs a TR system that has the propagating medium reversed and thus losses are compensated. So the TR algorithm has the advantage of compensating for attenuation and being applied in lossy media.

2.3.2 Discussion of Advantages and Disadvantages

The TR technique is elegant and computationally cost effective compared to the tomographic methods. In practical implementation, the other UWB antennas require more than a single measurement from the antennas. Particularly, the time-domain inverse scattering (TDIS) algorithm [12] entails the need for calculating the gradient of the cost function used in estimation of frequency-dependent average dielectric properties. In the TR technique, it is possible to use a single measurement from an array of antennas in order to detect and determine the location of a tumor scatterer. It claims to achieve proper focusing in 3D space even when some properties of the breast medium are not fully known.

CHAPTER 2 REVIEW: ULTRA WIDEBAND MICROWAVE RADAR IMAGING TECHNIQUES FOR BREAST CANCER DETECTION

The disadvantage of the TR technique is that it assumes that each antenna acts as a point source and the tumor is a point scatterer. This assumption is used to linearize the inverse scattering problem. Since focusing depends on the ability to identify the tumor response from the total signal at each receiver, the elimination of clutter and skin artifacts due to heterogeneities of breast tissue and skin reflections is vital. Loss compensation in TR is mainly possible for dielectric media with moderate conductivity. In these dielectrics, displacement current is dominant. Other disadvantages include the fact that design requirements for the UWB antennas have not been considered in the TR FDTD method. Finally, in order to minimize false positives, to optimize clutter removal, and to determine the shape of malignant tumors, it may be preferable to employ nonlinear modelling approaches together with the TR FDTD algorithm.

Although TR can detect tumors with high resolution, given the UWB pulse bandwidth, it has a drawback in relation to the diffraction limit. Therefore, this challenge may be addressed in research involving sub-wavelength microwave imaging techniques. Table 2.1 compares TR with other UWB microwave imaging techniques.

CHAPTER 2 REVIEW: ULTRAWIDEBAND MICROWAVE RADAR IMAGING TECHNIQUES FOR BREAST CANCER DETECTION

REFERENCES

- [1] D. M. Hailu, "Review of ultrawideband microwave radar imaging techniques for breast cancer detection," Computational Electromagnetic Lab Technical Report, CEM-R-38, January 2007.
- [2] S. C. Hagness, A. Taflove, and J. E. Bridges, "Two-dimensional FDTD analysis of a pulsed microwave Confocal system for breast cancer detection: fixed-focus and antenna-array sensors," *IEEE Trans. Biomed. Eng.*, vol. 45, no. 12, pp. 1470-1479, 1998.
- [3] S. C. Hagness, A. Taflove, and J. E. Bridges, "Three-Dimensional FDTD analysis of a pulsed microwave Confocal system for breast cancer detection: design of an antenna-array element," *IEEE Trans. Antennas Propagat.*, vol. 47, no. 5, pp. 783-791, 1999.
- [4] E. C. Fear and M. A. Stuchly, "Microwave detection of breast cancer," *IEEE Trans. Microwave Theory Tech.*, vol. 48, no. 11, pp. 1854-1863, 2000.
- [5] X. Li and S. C. Hagness, "A confocal microwave imaging algorithm for breast cancer detection," *IEEE Microwave Wireless Compon. Lett.*, vol. 11, no. 3, pp. 130-132, 2001.
- [6] E. C. Fear, X. Li, S. C. Hagness, and M. Stuchly, "Confocal microwave imaging for breast cancer detection: Localization of tumors in three dimensions," *IEEE Trans. Biomed. Eng.*, vol. 49, pp. 812-822, Aug. 2002.
- [7] E. J. Bond, S. C. Hagness, and B. D. Van Veen, "Microwave imaging via space-time beamforming for early detection of breast cancer," *IEEE Trans. Antennas Propagat.*, vol. 51, no. 8, pp. 1690-1705, 2003.
- [8] B. Van Veen, "Minimum variance beamforming," in *Adaptive Radar Detection and Estimation*, S. Haykin and A. Steinhardt, Eds. New York: Wiley, 1992, ch. 4, pp. 161-236.
- [9] S. Haykin, *Adaptive Filter Theory*. Upper Saddle River, NJ: Prentice-Hall, 1996.
- [10] W. Zhi, F. Chin, M. Chia, "Near Field UWB LCMV imaging for breast cancer detection with entropy based artifacts removal," in *IEEE Int. Conf. on Acoustics, Speech, and Signal Processing*, vol. 2, II-577 - II-580, May 2006.

CHAPTER 2 REVIEW: ULTRAWIDEBAND MICROWAVE RADAR IMAGING TECHNIQUES FOR BREAST CANCER DETECTION

- [11] P. Kosmas and C. M. Rappaport, "Time reversal with the FDTD method for microwave breast cancer detection," *IEEE Trans. Microwave Theory Tech.*, vol. 53, no. 7, pp. 2317-2323, July 2005.
- [12] D. W. Winters, E. J. Bond, B. D. Van Veen, and S. C. Hagness, "Estimation of the frequency-dependent average dielectric properties of breast tissue using a time-domain inverse scattering technique," *IEEE Trans. Antennas Propagat.* Vol. 54, no. 11, November 2006.
- [13] P. Kosmas and C. M. Rappaport, "A matched-filter FDTD-based time reversal approach for microwave breast cancer detection," *IEEE Trans. Antennas and Propagat.*, vol. 54, no. 4, pp. 1257-1264, April 2006.
- [14] S. Lehman and A. J. Devaney, "Transmission mode time-reversal superresolution imaging," *J. Acoust. Soc. Amer.*, vol. 113, pp. 2742-2753, 2003.
- [15] J. R. Taylor, *Scattering Theory*, FL: R. Krieger Inc., 1983.
- [16] W. C. Chew, *Waves and Fields in Inhomogeneous Media*. New York: Van Nostrand Reinhold, 1990.
- [17] M. Born and E. Wolf, *Principles of Optics*. 6th Ed. New York: Pergamon Press, 1980.
- [18] M. Fink, *Phys. Today* 50, 34, 1997.
- [19] R. Sorrentino, L. Rosseli and P. Mezzanote, "Time-reversal in finite difference time domain method," *IEEE Microwave Guided Wave Lett.*, vol. 3-11, no. 11, pp. 402-404, Nov. 1993.
- [20] M. Fink, D. Cassereau, A. Derode, C. Prada, P. Roux, M. Tanter, J. L. Thomas, and F. Wu, "Time-reversed acoustics," *Rep. Prog. Phys.*, vol. 63, pp. 1933-1995, 2000.

CHAPTER 3

NOVEL ROBUST TLM-BASED TIME-REVERSAL MICROWAVE RADAR IMAGING TECHNIQUE

3.1 INTRODUCTION

As an alternative to the CMI and MIST, Kosmas *et al.* [1][2] proposed a tumor detection and localization technique based on the principles of time reversal (TR) with the finite-difference time-domain (FDTD) method. The advantages and disadvantages of this technique are discussed in [3]. It is shown that if a point source radiates in free space and the time-reversed FDTD equations are applied to all points of the grid, the wave will converge back to the source at a time corresponding to the maximum of the initial excitation. The technique, which is proposed in [1][2] uses the time-reversed FDTD equations and the inverse varimax norm criterion. It is able to achieve focusing even when properties of the background medium are not known a priori as will be the case in a realistic microwave breast cancer detection system. In addition, it is able to

CHAPTER 3 NOVEL ROBUST TLM-BASED TIME-REVERSAL MICROWAVE RADAR IMAGING TECHNIQUE

compensate for losses because the propagating medium is reversed in the TR system.

This chapter discusses the use of the transmission-line matrix (TLM) method [4] instead of the FDTD method for building the time reversal mirror and cavities. In addition, we devise a new robust criterion for stopping the algorithm when the wave focuses back to the source scatterer. The new criterion we use is the modified Shannon entropy criterion (SEC) [5]. It is found to be more robust than the inverse varimax norm. Thus, our TR technique is different from [1][2] in that it is based on the TLM equations and it uses a better minimum entropy criterion based on [8].

We briefly note that the proposed TR algorithm is also different from the TLM-based algorithms proposed in [6][7]. This is because it is specifically designed for the detection of point-like scatterers such as small tumors in human tissue and it applies a robust stopping or convergence criterion, the SEC. In this chapter, the robustness of the SEC is demonstrated as compared to the inverse varimax norm. The technique is applied to the planar system using time-reversal mirror (TRM) and a cylindrical system using time-reversal cavity (TRC).

3.2 TWO-DIMENSIONAL TM-MODE TR TECHNIQUE WITH TLM METHOD

The TLM method carries out a sequence of scattering and connection steps [4]. It is a discrete time and space sampling method for modeling propagation of EM waves governed by Maxwell's equations. The propagation space is represented by a mesh of interconnected transmission lines modeling permittivity, permeability and conductivity of the space. Fig. 3.1 illustrates these scattering and connection steps in a 2-D TLM algorithm. The two-dimensional TM-mode, TLM shunt node is shown schematically in Fig. 3.1, where at any time and grid

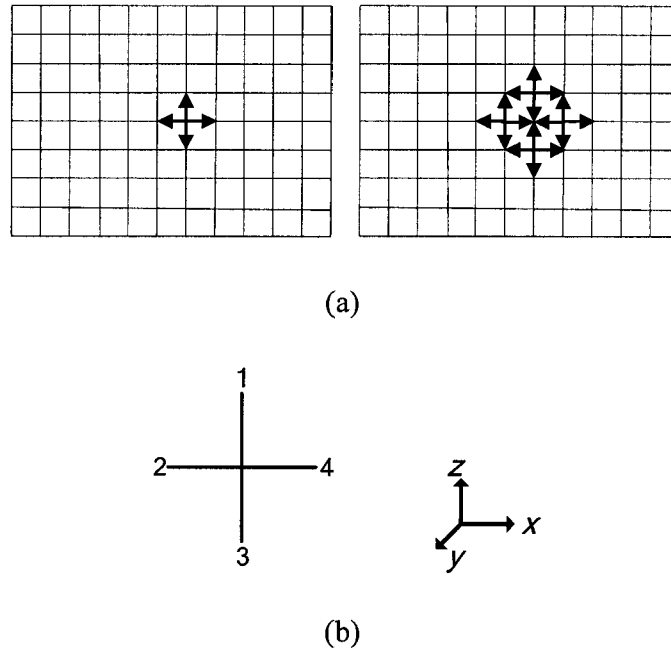


Fig. 3.1 2D-TLM shunt node: (a) illustration of the scattering and connection steps, (b) schematic.

CHAPTER 3 NOVEL ROBUST TLM-BASED TIME-REVERSAL MICROWAVE RADAR IMAGING TECHNIQUE

point we have the correspondences $V_y \equiv E_y$, $I_z \equiv H_x$, $I_x \equiv -H_z$, $2C \equiv \varepsilon$, $L \equiv \mu$, where ε and μ are the permittivity and permeability of the medium.

The TLM process is reversible in time because the scattering matrix is equal to its inverse [9]. Due to this property, reversing the process is possible without changing the algorithm [7]. One can reconstruct a source distribution from a known field solution by reversing the TLM process in time [6][7]. For the two-dimensional inhomogeneous breast medium, the TLM TR update equations involve sequences of scattering and connection steps, where for each node, the total node voltage is given as [4]

$${}_kV_y = \frac{2({}_kV_1^i + {}_kV_2^i + {}_kV_3^i + {}_kV_4^i) + 2{}_kV_s^i \hat{Y}_s}{4 + \hat{Y}_s + \hat{G}_s}. \quad (3.1)$$

The incident impulse ${}_kV_1^i$ on line 1 and the source impulse ${}_kV_s^i$ at the k -th time step, are scattered according to [4]

$$\begin{aligned} & {}_{k+1} \begin{bmatrix} V_1 \\ V_2 \\ V_3 \\ V_4 \end{bmatrix}^r = \mathbf{S} {}_k \begin{bmatrix} V_1 \\ V_2 \\ V_3 \\ V_4 \end{bmatrix}^i \\ \mathbf{S} &= \frac{1}{\hat{Y}} \begin{bmatrix} 2 - \hat{Y} & 2 & 2 & 2 & 2\hat{Y}_s \\ 2 & 2 - \hat{Y} & 2 & 2 & 2\hat{Y}_s \\ 2 & 2 & 2 - \hat{Y} & 2 & 2\hat{Y}_s \\ 2 & 2 & 2 & 2 - \hat{Y} & 2\hat{Y}_s \\ 2 & 2 & 2 & 2 & 2\hat{Y}_s - \hat{Y} \end{bmatrix} \end{aligned} \quad (3.2)$$

where $\hat{Y} = 4 + \hat{Y}_s + \hat{G}_s$. The normalized capacitive stub admittance is given by [4]

CHAPTER 3 NOVEL ROBUST TLM-BASED TIME-REVERSAL MICROWAVE RADAR IMAGING TECHNIQUE

$$\hat{Y}_s = 4(\varepsilon_r - 1) \quad (3.3)$$

and the normalized lossy stub capacitance is given by [5]

$$\hat{G}_s = -\sigma Z_c \Delta l \quad (3.4)$$

where Z_c is the characteristic impedance of each link line. The change in sign of (3.4) compensates for the ohmic losses in the TR model.

The boundaries on all four sides for both the data acquisition model and the TR model are TEM zero-reflection absorbing walls. The breast medium's inhomogeneity depends on the MRI image data used to generate the permittivity and conductivity profile of the forward breast model.

Antenna receivers are located close to breast-skin interface in the coupling medium, which is known. The input signal for backpropagation at each receiver is expressed as in [1] with a modification specific to the TLM case [5]:

$$f_i(t) = V_y(x_i, z_i) \cdot \exp \left[- \left(\frac{t - t_p}{\nu} \right)^2 \right] \quad (3.5)$$

where t_p is the time instant when the peak of the received waveform $V_y^p(x_i, z_i)$ occurs for a short pulse excitation, and ν is the taper parameter, which determines the width of the impulse temporal window function. The location of each receiver is given by the coordinates (x_i, z_i) , $i = 1, \dots, N$, and N is the number of receivers ($N = 23$ in [1]).

3.3 MODIFIED SHANNON ENTROPY CRITERIA

Similarly to the TR FDTD equations [1][2], if a point source radiates in free space and the TR TLM equations are applied to all points in the grid, the wave will converge back to the source at the time corresponding to the maximum of the initial excitation. In [1], a minimum entropy criterion is employed based on the inverse varimax norm.

In this chapter, we consider another entropy measure, the Shannon entropy given by [8]

$$H(p_1, p_2, \dots, p_n) = -K \sum_{l=1}^n p_l \log_2 p_l \quad (3.6)$$

where K is a constant and n is the number of possible events with probabilities of occurrence given by p_l where $l=1,2,\dots,n$. One of the properties of the Shannon entropy is that if all the p_l are equal or have uniform probability distribution then H (3.6) is a monotonic increasing function [8]. Our aim is to exploit this property and make modifications to (3.6) in order to outperform the inverse varimax norm.

We assume a uniform probability distribution where the number of outcomes for a certain event is divided by the total number of outcomes. We consider the rate at which the voltage value of a grid point, corresponding to a peak value at the k -th time step, changes compared to the voltage values of adjacent grid cells at the k -th time step within the breast medium.

CHAPTER 3 NOVEL ROBUST TLM-BASED TIME-REVERSAL MICROWAVE RADAR IMAGING TECHNIQUE

In our modified Shannon entropy criterion (SEC) the definition of (3.6) is changed by re-defining p_l and changing the sign of (3.6) in order to find the minimum entropy in the 2-D TR TLM simulations. The SEC is defined as [5]

$$S(V_y^k) \triangleq p_l \log_2 p_l. \quad (3.7)$$

Here [5],

$$p_l = \frac{D^k \cdot |V_{ypeak}^k|^2}{\sum_{i,j} \left(\frac{V_y^k(i,j)}{V_{ypeak}^k} \right)^2} \quad (3.8)$$

where k is the time step of the TLM TR algorithm, (i, j) are grid cell coordinates, and the summation is over the breast region. $V_y^k(i, j)$ is the 2D TLM TM mode voltage at the (i, j) grid cell, and V_{ypeak}^k is the maximum voltage for time step k inside the breast region. The parameter D^k is a constant at time step k , which is related to the deviation of the node voltage values in a specified region around the peak value V_{ypeak}^k . The parameter $D^k = 1$ for all values of k in this chapter because the tumor sizes considered are generally much greater than the shortest wavelength of the UWB pulse. Small 3-mm-diameter tumors can be detected by using (3.7) with $D^k = 1$.

CHAPTER 3 NOVEL ROBUST TLM-BASED TIME-REVERSAL MICROWAVE RADAR IMAGING TECHNIQUE

The examples in the subsequent section demonstrate that the SEC is more robust than the inverse varimax norm for applications with the TLM TR and the FDTD TR algorithms.

3.4 EXAMPLES

In this section, both planar and cylindrical configurations of 2-D TLM breast models are investigated. These 2D breast models are derived from MRI data. The TLM TR algorithms and the SEC discussed in sections 3.2 and 3.3, respectively, are applied in the two examples.

3.4.1 Planar System using Time-Reversal Mirror

First we discuss and investigate the robustness of the SEC using a similar setup as in [1] using TRM. Both, the data acquisition model and the TR model are implemented with the TLM method, with a grid size of $0.5\text{ mm} \times 0.5\text{ mm}$ and a time step of 1.179 ps . The TLM TR algorithm is implemented within Matlab [10]. The maximum number of time steps in the TLM TR model is 3000. The TLM TR algorithm is run in reverse starting from time step 2500 since the recorded backscattered field at the receivers after that time step is very small and close to zero. The forward model used for data acquisition is based on 2-D MRI image cross-section of the breast as seen in Fig. 3.2. Fig. 3.3 shows the dielectric profile for the inhomogeneous breast tissue.

CHAPTER 3 NOVEL ROBUST TLM-BASED TIME-REVERSAL MICROWAVE
RADAR IMAGING TECHNIQUE

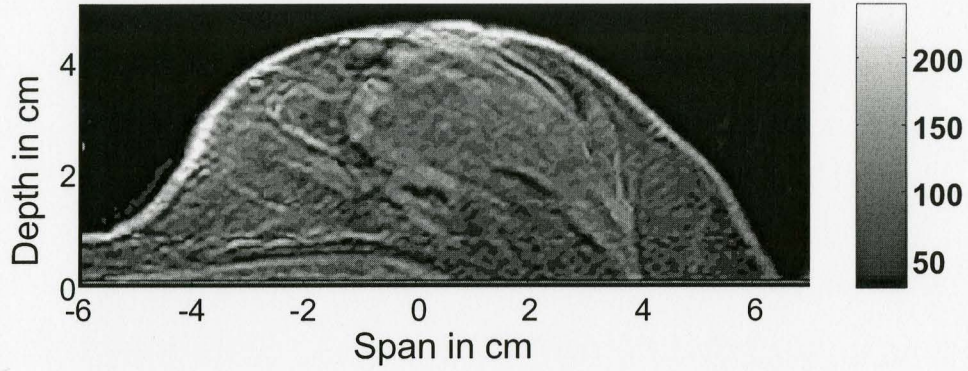


Fig. 3.2 The 2-D MRI data of a 57 year old female [5].

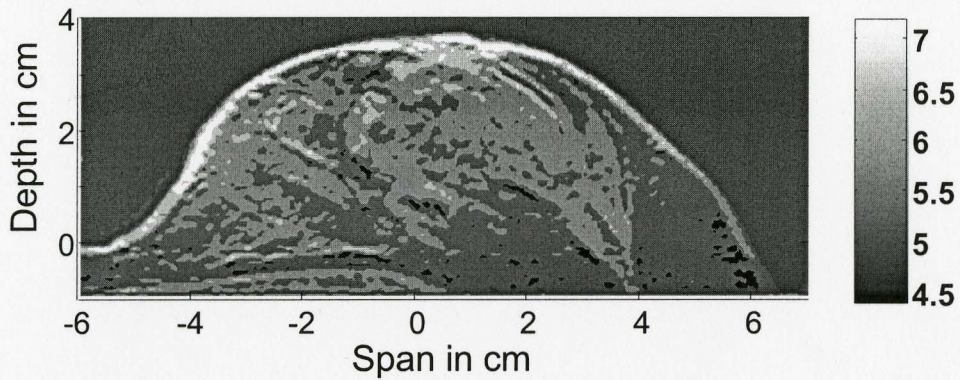


Fig. 3.3 The corresponding 2-D dielectric profile of the inhomogeneous breast tissue.

The regions corresponding to the fibroglandular tissues in the breast are linearly mapped to higher permittivity and conductivity values than breast fat with an upper bound of 32% above the nominal values ($\epsilon_r = 4.58$ and $\sigma = 0.52$ S/m) and a lower bound of 16% above the nominal

CHAPTER 3 NOVEL ROBUST TLM-BASED TIME-REVERSAL MICROWAVE RADAR IMAGING TECHNIQUE

values. Breast fat regions are mapped to values with $\pm 16\%$ variability from nominal breast fat values. The skin layer is artificially introduced and has dielectric values of $\epsilon_r = 31$ and $\sigma = 5.8$ S/m. The surrounding coupling medium is a lossless dielectric with dielectric constant $\epsilon_r = 4.48$.

For the forward model, the antenna element #12 is transmitting a 50-ps differentiated Gaussian UWB pulse. All the 23 antenna elements located at a small distance from the top of the breast are receivers as in [1]. The skin layer and 3-mm diameter tumor (a spherical scatterer) at -0.85 cm span and 3.65 cm depth are artificially introduced. Since specific antenna elements are not modeled, a transmitter is represented by a point source assigned a voltage value V_y (TM-mode), and the receivers are represented by observation points. As discussed in [1][2], the tumor acts as a point scatterer, which only introduces an amplitude scaling and a time delay to the shape of the total reflected field recorded at each receiver.

When doing TLM TR simulations to find the 3-mm diameter tumor, we consider first the case using the inverse varimax norm as in [1], and second, the case using the modified Shannon entropy criterion (SEC) as in [5]. We obtain the plot of the inverse varimax norm vs. time as shown in Fig. 3.4. The resultant image is shown in Fig. 3.5. It corresponds to a minimum of the varimax norm at the 749-th time step.

CHAPTER 3 NOVEL ROBUST TLM-BASED TIME-REVERSAL MICROWAVE RADAR IMAGING TECHNIQUE

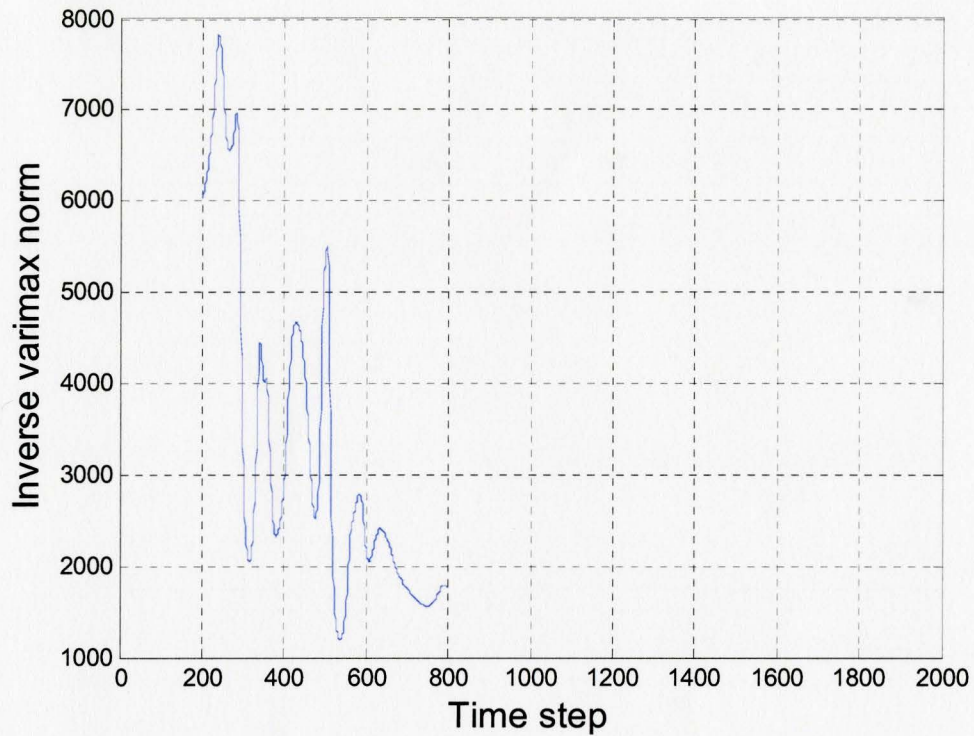


Fig. 3.4 The inverse varimax norm as function a of time. The first minimum at time step 749 is assigned as a solution. The corresponding tumor location is at -0.85 cm span and 3.55 cm depth.

Next, we employ the SEC instead of the inverse varimax norm. We obtain the plot of the SEC vs. time as shown in Fig. 3.6. The resultant image is shown in Fig. 3.7. It corresponds to a minimum of the SEC at 748 time step or 0.882 ns.

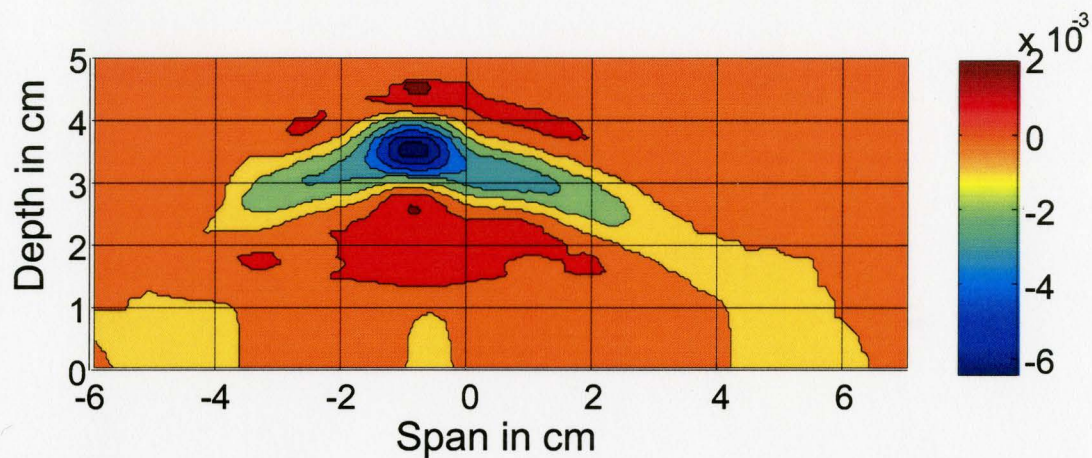


Fig. 3.5 The resultant image corresponding to the solution obtained using the inverse varimax norm. The corresponding tumor location is at -0.85 cm span and 3.55 cm depth, while the actual tumor location was at -0.85 cm span and 3.65 cm depth.

CHAPTER 3 NOVEL ROBUST TLM-BASED TIME-REVERSAL MICROWAVE RADAR IMAGING TECHNIQUE

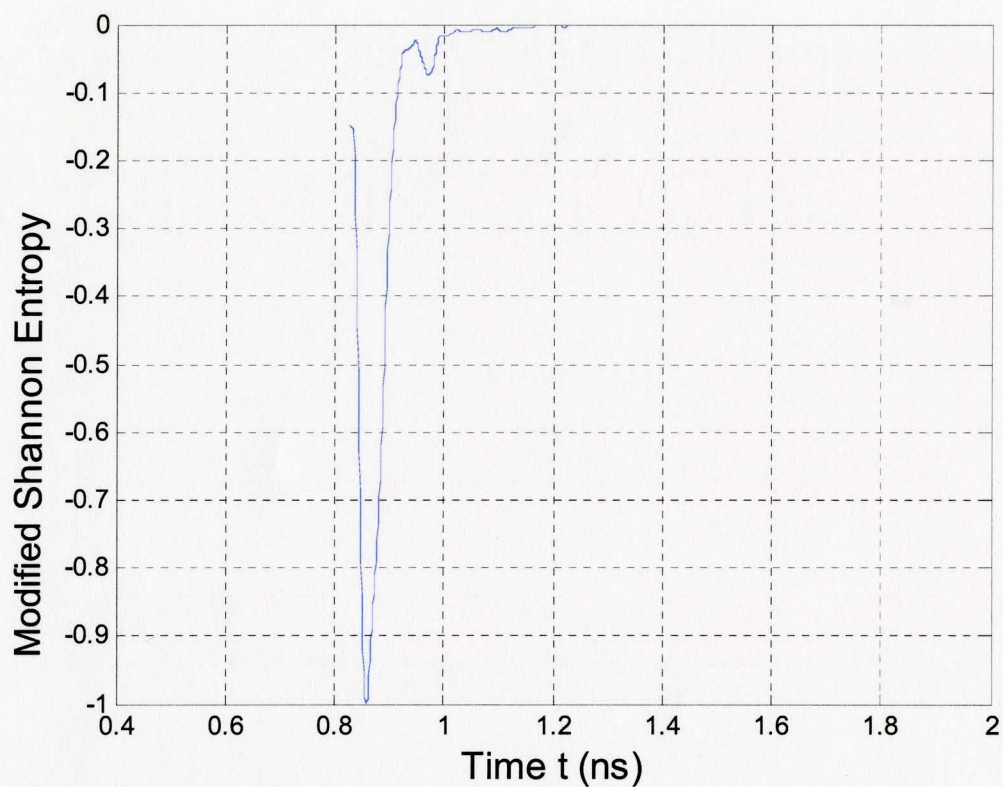


Fig. 3.6 The modified Shannon entropy criterion (SEC) response as function of time. The global minimum is assigned as solution. There is only one minimum instead of multiple minima and the corresponding location to the solution is at -0.85 cm span and 3.55 cm depth.

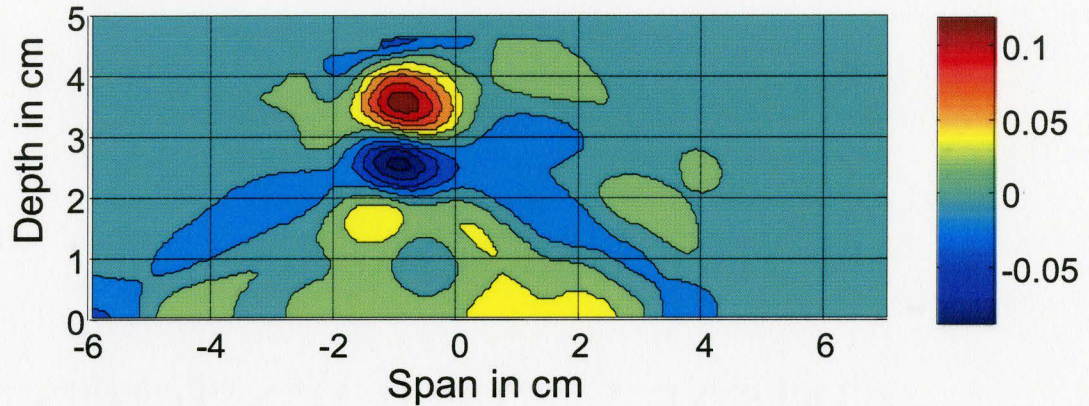


Fig. 3.7 The resultant image corresponding to the solution obtained using the SEC. The corresponding tumor location is at -0.85 cm span and 3.55 cm depth, while the actual tumor location was at -0.85 cm span and 3.65 cm depth.

There are too many minima in the inverse varimax norm and it is not obvious as to which minimum corresponds to the actual accurate solution. In [1] and [2], Kosmas *et al.* have an algorithm which stops when encountering the first minimum. But this is not necessarily a robust approach to finding the minimum entropy where the wave focuses back to the source.

On the other hand, when employing the SEC, there is only one minimum found for the entire set of time steps. So the time step corresponding to the solution is found at one minimum. Thus, this criterion is more robust as compared to the inverse varimax norm.

3.4.2 Cylindrical System using Time-Reversal Cavity

The dielectric profile for the cylindrical system derived from the MRI-data is shown in Fig. 3.8 without a tumor and in Fig. 3.9 with a tumor. A 3-mm diameter tumor is inserted at X span 0.3 cm and Y span 3.65 cm. There are 16 receivers with one transmitter. Here, we employ a time-reversal cavity where we store the backpropagated wave at 16 receiver locations.

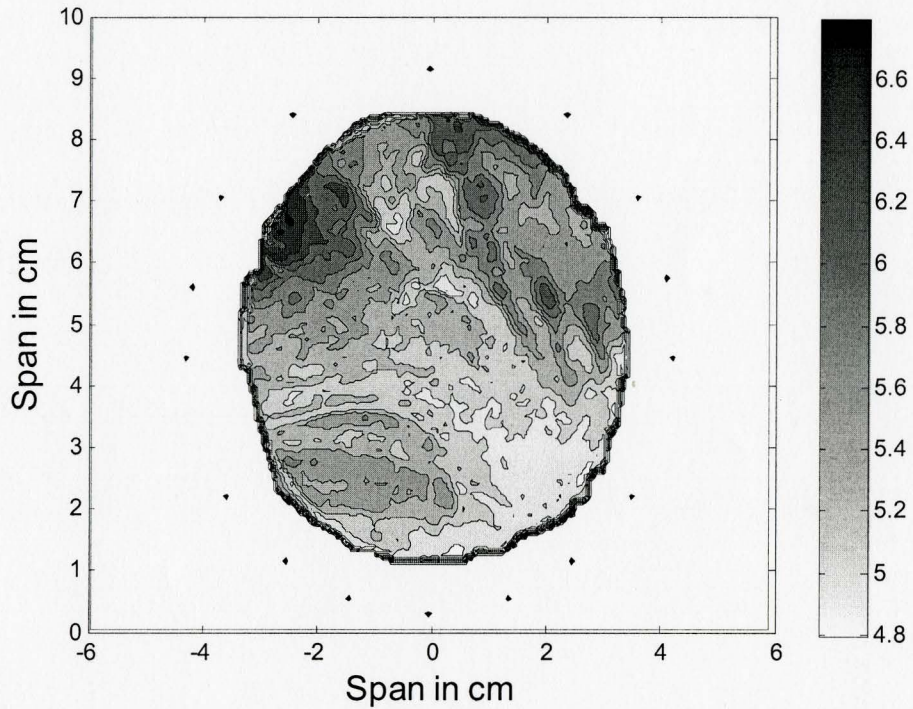


Fig. 3.8 The MRI-derived 2D TLM model for the cylindrical configuration for heterogeneous breast without tumor.

CHAPTER 3 NOVEL ROBUST TLM-BASED TIME-REVERSAL MICROWAVE RADAR IMAGING TECHNIQUE

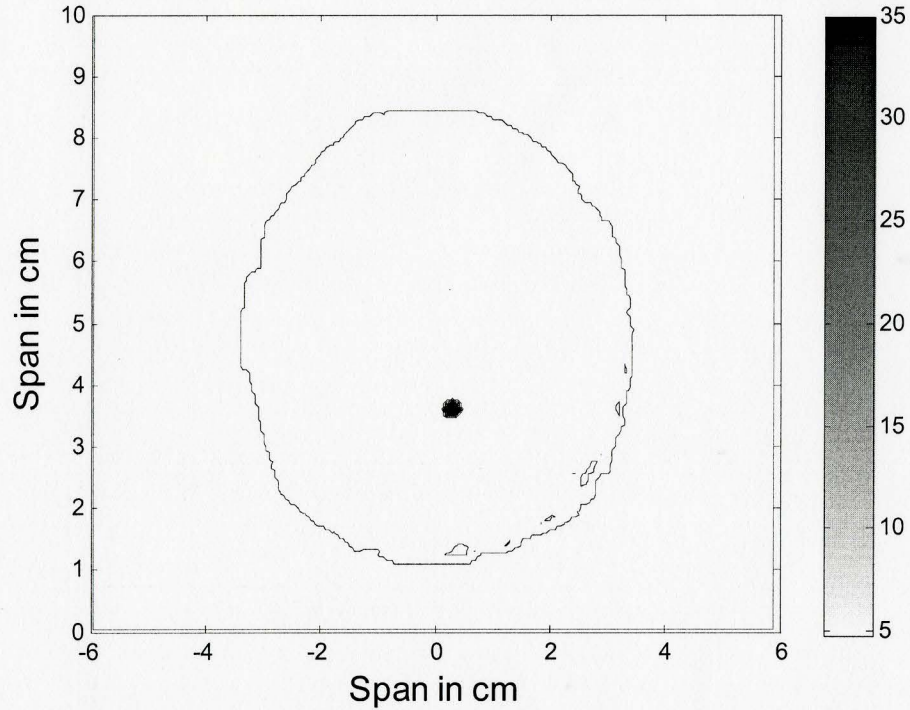


Fig. 3.9 The MRI-derived 2D TLM model for the cylindrical configuration for heterogeneous breast with tumor inserted at X span 0.3 cm and Y span 3.65 cm.

The TR TLM inverse varimax norm vs. time is plotted in Fig. 3.10. The inverse varimax has too many minima and the first minimum, as suggested in [1], does not correspond to the accurate solution. The solution corresponding to the global minimum of the inverse varimax norm is accurate and is at X span 0.2 cm and Y span 3.55 cm. Since there are too many minima and the first minimum does not yield an accurate solution, we conclude that the inverse varimax norm is an unreliable convergence criterion.

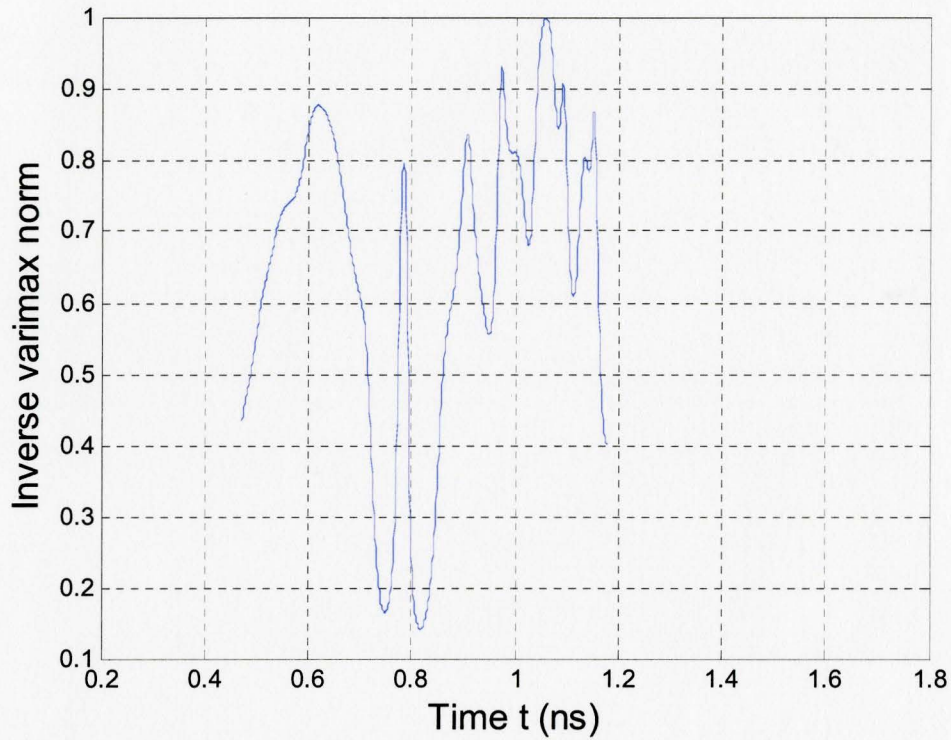


Fig. 3.10 The inverse varimax norm as a function of time. The first minimum does not give accurate solution. The location of the solution using the global minimum is at X span 0.2 cm and Y span 3.55 cm, which is fairly accurate.

The resultant image corresponding to the solution obtained using the global minimum of the inverse varimax norm is shown in Fig. 3.11.

Employing the SEC instead of the inverse varimax norm, we obtain the plot shown in Fig. 3.12. The resultant image is shown in Fig. 3.13. The SEC again has only one minimum which is the first minimum found when running the algorithm in reverse time. The time step found corresponds to

CHAPTER 3 NOVEL ROBUST TLM-BASED TIME-REVERSAL MICROWAVE
RADAR IMAGING TECHNIQUE

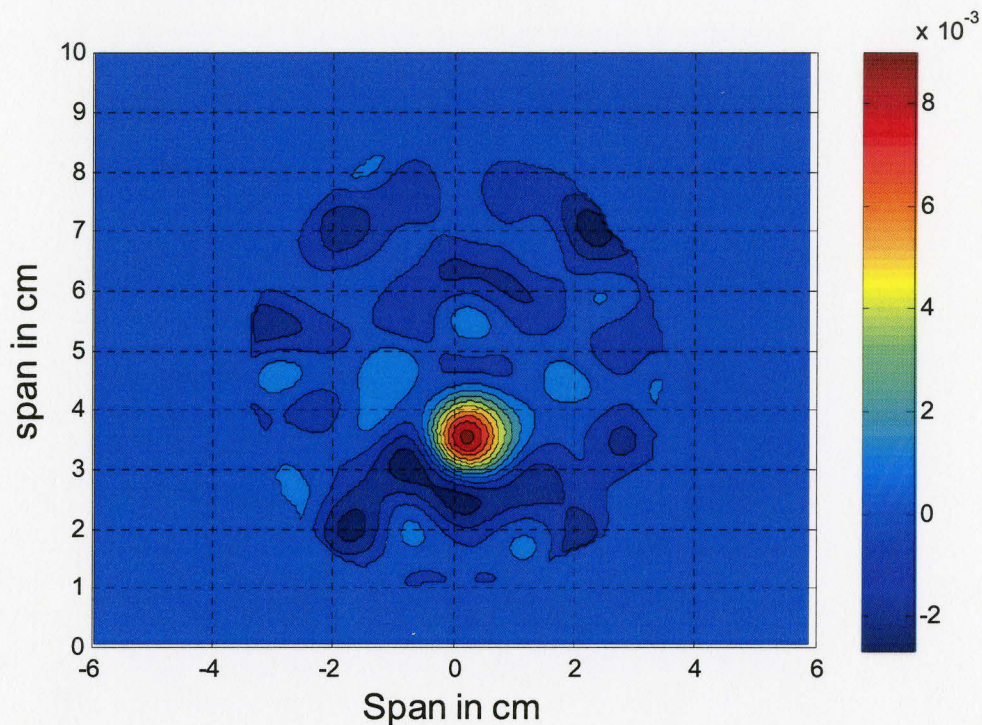


Fig. 3.11 The resultant image corresponding to the solution obtained using the global minimum of the inverse varimax norm. The corresponding location to the solution is at X span 0.2 cm and Y span 3.55 cm.

a global minimum and the resultant location is at X span 0.25 cm and Y span 3.55 cm, which is fairly accurate.

CHAPTER 3 NOVEL ROBUST TLM-BASED TIME-REVERSAL MICROWAVE
RADAR IMAGING TECHNIQUE

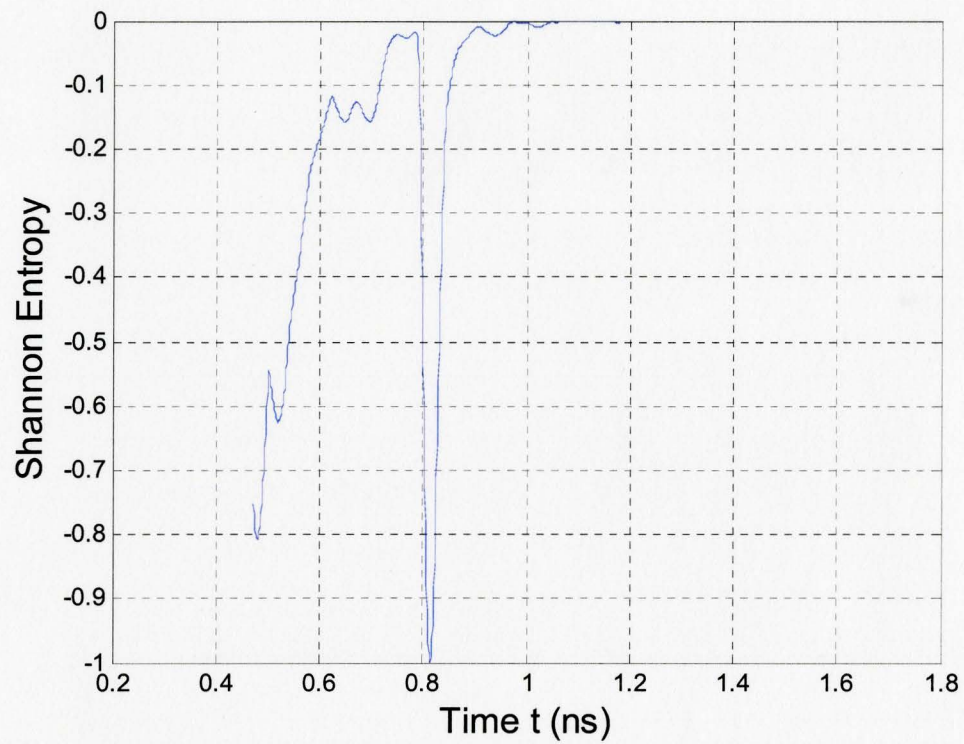


Fig. 3.12 The SEC response as a function of time. The first minimum is the global minimum and it gives an accurate solution. The location of the solution is at X span 0.25 cm and Y span 3.55 cm.

CHAPTER 3 NOVEL ROBUST TLM-BASED TIME-REVERSAL MICROWAVE
RADAR IMAGING TECHNIQUE

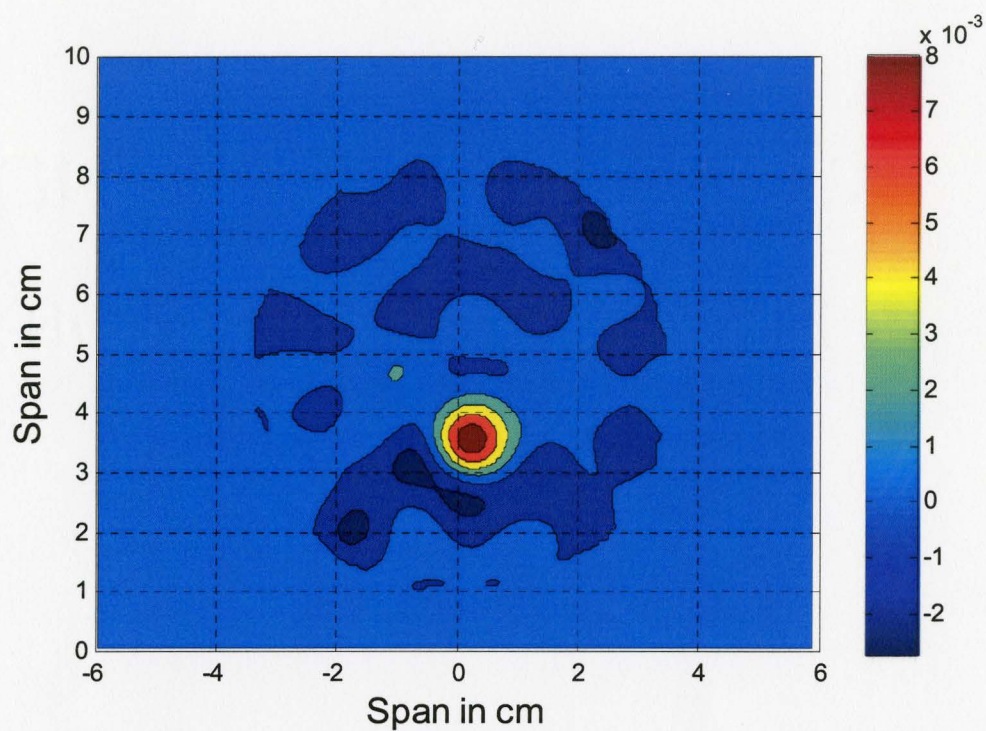


Fig. 3.13 The resultant image corresponding to the solution obtained using the SEC. The corresponding location to the solution is at X span 0.25 cm and Y span 3.55 cm.

3.5 CONCLUDING REMARKS

A novel robust TLM-based time-reversal algorithm for microwave radar imaging is proposed and applied to the detection of breast cancer tumors in both the cylindrical and planar systems. In addition, we devise a robust stopping criterion to determine when the wave focuses back to the source scatterer and to determine the location of the tumor. The new criterion we uses is the modified Shannon entropy criterion (SEC) [5].

The extractions of the tumor signal through skin-breast artifact removal algorithms and techniques to compensate for dispersion were not considered in this chapter. However, the TLM TR algorithm has a taper parameter that can be used to compensate for dispersion effects.

It is demonstrated through two examples, the TR mirror and TR cavity, that the SEC is more robust than using the inverse varimax norm. TR has been shown to be superior to other simple delay-based focusing techniques and here we have extended the TR algorithm by making it more robust in localizing small tumors. The importance of this finding becomes evident as the SEC also plays an important role in detection of tumors that are sub-wavelength in size.

CHAPTER 3 NOVEL ROBUST TLM-BASED TIME-REVERSAL MICROWAVE RADAR IMAGING TECHNIQUE

REFERENCES

- [1] P. Kosmas and C. M. Rappaport, "Time reversal with the FDTD method for microwave breast cancer detection," *IEEE Trans. Microwave Theory Tech.*, vol. 53, no. 7, pp. 2317-2323, July 2005.
- [2] P. Kosmas and C. M. Rappaport, "A matched-filter FDTD-based time reversal approach for microwave breast cancer detection," *IEEE Trans. Antennas and Propagat.*, vol. 54, no. 4, pp. 1257-1264, April 2006.
- [3] D. M. Hailu, "Review of ultrawideband microwave radar imaging techniques for breast cancer detection," CEM-R-38, January 2007.
- [4] C. Christopoulos, *The Transmission-Line Modeling (TLM) method in Electromagnetics*. Morgan & Claypool Publishers, San Rafael, CA, USA, 2006.
- [5] D. M. Hailu, N. K. Nikolova and M. H. Bakr, "Sub-wavelength microwave radar imaging for detection of breast cancer tumors," in *2007 IEEE Int. Microwave Symp. on Signals, Systems, and Electronics*, pp.107 – 110, Montréal, Canada, July 2007.
- [6] M. H. Bakr, P. P. M. So and W. J. R. Hoefer, "The generation of optimal microwave topologies using time-domain field synthesis," *IEEE Trans. Microwave Theory Tech.*, vol. 50, pp. 2537-2544, Nov. 2002.
- [7] M. Forest and W. J. R. Hoefer, "TLM synthesis of microwave structures using time reversal," in *IEEE MTT-S Int. Microwave Symp. Dig.*, pp. 779 – 782, Jun. 1992.
- [8] C. Shannon and W. Weaver, *The Mathematical Theory of Communication*. Urbana, University of Illinois, 1964.
- [9] R. Sorrentio, P. P. M. So and W. J. R. Hoefer, "Numerical microwave synthesis by inversion of the TLM process", in *21st European Microwave Conference Digest*, pp. 1273-1277, Stuttgart, Germany, Sept. 1991.
- [10] MATLAB™ 7.1, The MathWorks Inc., 3 Apple Hill Drive, Natick, MA, 2005.

CHAPTER 4

ACHIEVING SUB-WAVELENGTH RESOLUTION WITH THE TLM- BASED SHANNON ENTROPY TR TECHNIQUE

4.1 INTRODUCTION

UWB microwave radar imaging techniques for breast cancer detection seek to identify the existence and location of strong microwave scatterers in the breast. In an UWB microwave imaging system, a wideband pulse is transmitted from an array of antennas located near the breast surface and then the backscattered microwave signals from malignant lesions in the breast are used to identify the presence and location of tumors. The confocal microwave imaging (CMI) [1] technique, the microwave imaging based on space-time (MIST) beamforming [2], and the time reversal (TR) with the FDTD method [3][4] are some of the major UWB microwave radar imaging techniques [5] used for tumor

CHAPTER 4 ACHIEVING SUB-WAVELENGTH RESOLUTION WITH THE TLM-BASED SHANNON ENTROPY TR TECHNIQUE

detection and localization. However, these techniques can not achieve sub-wavelength resolution.

This chapter examines and presents the possibility of sub-wavelength tumor detection and localization using alternating phase radiators similar to the principle of phase-shifting mask (PSM) of Levenson *et al.* [6]. In analogy to the PSM technique, the use of alternating phase radiators increases the resolution of the backscattered fields for sub-wavelength detection of breast tumors. PSM [6] enables the clear regions of a mask to transmit light with a prescribed phase shift. All PSM variations employ the basic concept proposed by Levenson *et al.* [6]. When light passes through the aperture on the mask, an image is formed on the wafer. The image forming characteristics of this optical imaging systems are limited by the finite numerical aperture. The numerical aperture is related to the index of refraction of the medium in which the lens operate, and the angular aperture of the lens. Finite numerical aperture affects the resolution of the image and causes the image to spread. In PSM implementation, the electric field transmitted through one aperture is out of phase by 180° with the neighboring aperture. As a result, destructive interference minimizes the light intensity between their images. The images of such phase-shifting transmission have better resolution and higher contrast than a conventional transmission object without phase shifts.

In addition to employing the concept of the PSM technique for the forward and the TRM simulations, the TR algorithm with the TLM method [7]

CHAPTER 4 ACHIEVING SUB-WAVELENGTH RESOLUTION WITH THE TLM-BASED SHANNON ENTROPY TR TECHNIQUE

uses the modified Shannon entropy criterion (SEC) [8], an alternative more robust criterion to [3][4] for determining when the time-reversed propagating wave focuses back to the source scatterer. A 0.5-mm diameter tumor was detected and located using a 200-ps UWB pulse in a realistic inhomogeneous two dimensional breast model.

Section 4.2 discusses the motivation of employing the PSM technology for sub-wavelength microwave radar imaging. It also discusses the origin of the diffraction limit and proposed ways to overcome it using time reversal. The experimental setup is described in section 4.3 followed by the TLM-based TR algorithm in section 4.4. Section 4.5 discusses different numerical results. The effect of dielectric contrast on the detection of tumors of sub-wavelength size is discussed in section 4.6. Since the detection of evanescent waves is lost when the subwavelength scatterer is in the far field of the TRM, i.e., when the scatterer is located far from the antenna receivers, a TLM-based TR algorithm employing two TRMs is proposed and discussed in section 4.7. This is followed by a discussion of the effect of the depth and the proximity of the tumor to the antenna receivers.

4.2 MOTIVATION OF EMPLOYING PHASE-SHIFTING MASK (PSM) TECHNOLOGY FOR SUB-WAVELENGTH IMAGING

The principles of phase-shifting mask (PSM) of Levenson *et al.* [6] have been employed for sub-wavelength optical lithography since the early 1980's. Since 1982, various forms of PSM have been developed based on PSM [9]. It enables the clear regions of a mask to transmit light with a prescribed phase shift enhancing resolution beyond the diffraction limit.

To briefly summarize, when coherent light passes through a conventional transmission mask, the light diffracted by the two neighboring apertures interferes constructively to produce significant intensity in the region of the wafer between the apertures [6]. For the PSM mask, a transparent phase-shifting layer covers neighboring apertures. As a result, the layer reverses the polarity of the electric field corresponding to the covered aperture. The intensity pattern on the wafer at the apertures is unchanged by the PSM. However, due to destructive interference on the wafer between neighboring apertures, the waves diffracted from neighboring apertures produce minimal intensity between the apertures [6].

In a conventional transmission mask, the intensity between the apertures is maximized due to the constructive interference between the diffracted fields from the apertures. This effect causes reduction in the resolution of any optical system with coherent illumination [6].

CHAPTER 4 ACHIEVING SUB-WAVELENGTH RESOLUTION WITH THE TLM-BASED SHANNON ENTROPY TR TECHNIQUE

For the case of the PSM, the E-field transmitted through neighboring apertures is out of phase by 180° . As a result, the destructive interference minimizes the intensity between their images. The phase shift at the aperture happens when a transparent layer is added with a thickness of $d = \lambda / 2(n-1)$, where λ is wavelength and n is the index of refraction [6][9].

In UWB microwave imaging exploiting TR techniques, the subwavelength information about a tumor is carried by the evanescent waves. These waves generally decay exponentially and are lost before reaching the recording far-field plane of the time-reversal mirror (TRM). This is the origin of the diffraction limit. For an inhomogeneous medium such as the breast, the time-reversed wave which spatially converges to the location of the tumor is immediately followed by a diverging wave due to energy flux conservation [10][11][12].

Subject to further proof, we find our technique gains in resolutions due to the principles discussed in [6], [11] and [12]. In [11], a TR cavity is employed to show how to overcome the diffraction limit using an acoustic sink. De Rodny and Fink [11] also describe, using acoustic wave theory, how an acoustic sink produces a subwavelength focusing wave. From the theory of TR cavity, assuming a non-dissipative purely homogenous medium, a point-like source scatterer at \mathbf{r}_0 excited by a waveform $f(t)$ generates a wave field

CHAPTER 4 ACHIEVING SUB-WAVELENGTH RESOLUTION WITH THE TLM-BASED SHANNON ENTROPY TR TECHNIQUE

$$\Phi_S(\mathbf{r}; t) = \frac{A e^{-jk\|\mathbf{r}-\mathbf{r}_0\|}}{4\pi\|\mathbf{r}-\mathbf{r}_0\|} e^{-j\omega t} \text{ with complex magnitude } A \text{ and observation point } \mathbf{r}.$$

This is the solution of the wave equation with a source term

$$\nabla^2 \Phi_S(\mathbf{r}; t) - \frac{1}{c^2} \frac{\partial^2}{\partial t^2} \Phi_S(\mathbf{r}; t) = \delta(\mathbf{r} - \mathbf{r}_0) f(t) \quad (4.1)$$

The solution is an isotropic wave that diverges from \mathbf{r}_0 . These waves propagate up to the surface of the TR cavity and are recorded at the receivers.

In the TR simulation, the TR cavity then generates a spherical wave field, $\Phi_{TR}(\mathbf{r}; t)$, that focuses on \mathbf{r}_0 . This spherical wave field has two components, the time-reversed image of the emitted wave, $\Phi_S(\mathbf{r}; -t)$, and a wavefield generated by TR source $\Phi_{TRS}(\mathbf{r}; t)$ [11]. $\Phi_S(\mathbf{r}; -t)$ is given at a wavenumber k by the advanced or anti-causal homogeneous Green's function between source \mathbf{r}_0 and observation point \mathbf{r} as

$$G^-(\mathbf{r}, \mathbf{r}_0) = \frac{e^{jk\|\mathbf{r}-\mathbf{r}_0\|}}{4\pi\|\mathbf{r}-\mathbf{r}_0\|} \quad (4.2)$$

which is solution of a propagation equation with a source term

$$\nabla^2 \Phi_S(\mathbf{r}; -t) - \frac{1}{c^2} \frac{\partial^2}{\partial t^2} \Phi_S(\mathbf{r}; -t) = \delta(\mathbf{r} - \mathbf{r}_0) f(-t). \quad (4.3)$$

While the wave field $\Phi_{TR}(\mathbf{r}; t)$ is the solution of the propagation equation without a source

$$\nabla^2 \Phi_{TR}(\mathbf{r}; t) - \frac{1}{c^2} \frac{\partial^2}{\partial t^2} \Phi_{TR}(\mathbf{r}; t) = 0. \quad (4.4)$$

CHAPTER 4 ACHIEVING SUB-WAVELENGTH RESOLUTION WITH THE TLM-BASED SHANNON ENTROPY TR TECHNIQUE

The right hand side of equation (4.3) represents the time-reversed image of a source excited by $f(t)$ waveform at location \mathbf{r}_0 . The TR source term generates a field equal to

$$\Phi_{TRS}(\mathbf{r}; t) = \frac{A^* e^{-jk\|\mathbf{r}-\mathbf{r}_0\|}}{4\pi\|\mathbf{r}-\mathbf{r}_0\|} e^{-j\omega t} \quad (4.5)$$

The diverging wave generated by the TR source is given by the retarded or causal

Green's function $G^+(\mathbf{r}, \mathbf{r}_0) = \frac{e^{-jk\|\mathbf{r}-\mathbf{r}_0\|}}{4\pi\|\mathbf{r}-\mathbf{r}_0\|}$. The total spherical wave field

$\Phi_{TR}(\mathbf{r}; t)$ is then $\Phi_{TR}(\mathbf{r}; t) = \Phi_S(\mathbf{r}; -t) - \Phi_{TRS}(\mathbf{r}; t)$ and is given by [11]

$$\begin{aligned} \Phi(\mathbf{r}; t) &= A^* \frac{e^{jk\|\mathbf{r}-\mathbf{r}_0\|}}{4\pi\|\mathbf{r}-\mathbf{r}_0\|} e^{-j\omega t} - A^* \frac{e^{-jk\|\mathbf{r}-\mathbf{r}_0\|}}{4\pi\|\mathbf{r}-\mathbf{r}_0\|} e^{-j\omega t} \\ &= \frac{jkA^*}{2\pi} \text{sinc}(k\|\mathbf{r}-\mathbf{r}_0\|) \cdot e^{-j\omega t} \end{aligned} \quad (4.6)$$

In order to overcome the diffraction limit, a source such as an acoustic sink can be placed at the focusing point transmitting a diverging wave opposite in phase with the diverging part of (4.6) or $\Phi_{TRS}(\mathbf{r}; t)$. Due to destructive interference, the TR source with opposite phase cancels the diverging part of (4.6) and only the converging wave equal to $\Phi_S(\mathbf{r}; -t)$ remains. The theory developed for acoustic waves in [10][11] can be applied directly to EM fields. This is because the vertical E -field component of the solution of the 2-D vector wave equation satisfies the scalar wave equation whose solution is (4.6).

CHAPTER 4 ACHIEVING SUB-WAVELENGTH RESOLUTION WITH THE TLM-BASED SHANNON ENTROPY TR TECHNIQUE

Based on this finding, Lerosey *et al.* 2007 [12], proposed an approach for subwavelength focusing by building a microstructured medium in the near-field of the point where one intends to focus and use a TRM placed in the far field to build the time-reversed wave field that overcomes the diffraction limit and focuses at the target. Their approach consists of surrounding the focusing point by a microstructured medium with typical scales well below the wavelength. This is done by putting strong scatterers in the near-field of the source [12].

In our novel approach [8], subwavelength focusing is achieved by using the concept of the PSM and by arranging the transmitting/receiving array so that neighboring elements transmit opposite polarity pulses. From [11], we find that by having alternating polarity radiators in the TRM, the waves that diffract from the tumor have both the diverging wave produced by the TR source and the diverging wave opposite in phase to the diverging part of $\Phi_{TR}(\mathbf{r};t)$ in (4.6). Therefore, they interfere destructively and only a converging wave equal to $\Phi_S(\mathbf{r};-t)$ remains. Due to this setup, we find that there is detectable backscattered field emanating from scatterers of subwavelength size.

Our approach to recover evanescent waves is to transmit UWB pulses of alternating polarity with the antennas separated by $l = 5.7$ mm while the TRM is in the far-field region. By diffracting off the scatterer, evanescent waves are converted into propagating waves. This is due to the theorem of generalized

CHAPTER 4 ACHIEVING SUB-WAVELENGTH RESOLUTION WITH THE TLM-BASED SHANNON ENTROPY TR TECHNIQUE

reciprocity between evanescent waves and propagating waves [13]. Thus the evanescent waves are recovered in the back-propagation step of the TR process.

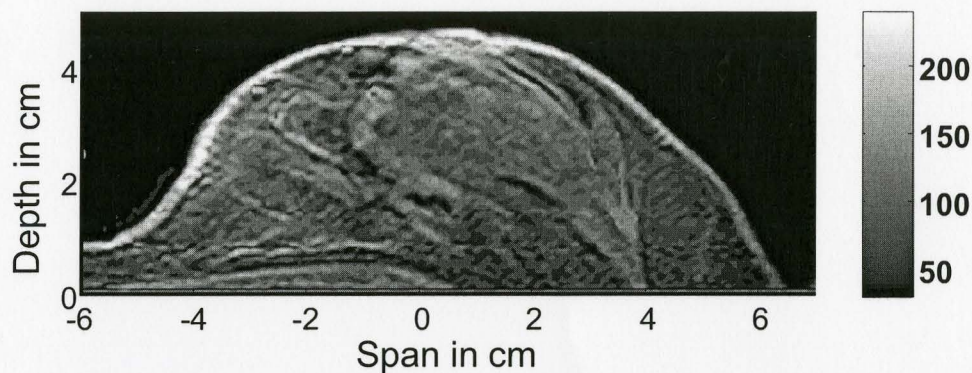
4.3 EXPERIMENTAL SETUP

The experimental system is comprised of an array of 23 receivers/transmitters located at a small distance from the top of the breast, and placed every $10 \cdot \Delta x$ with $\Delta x = 0.57$ mm, same as in [4]. All elements transmit simultaneously, but neighboring elements transmit opposite polarity pulses.

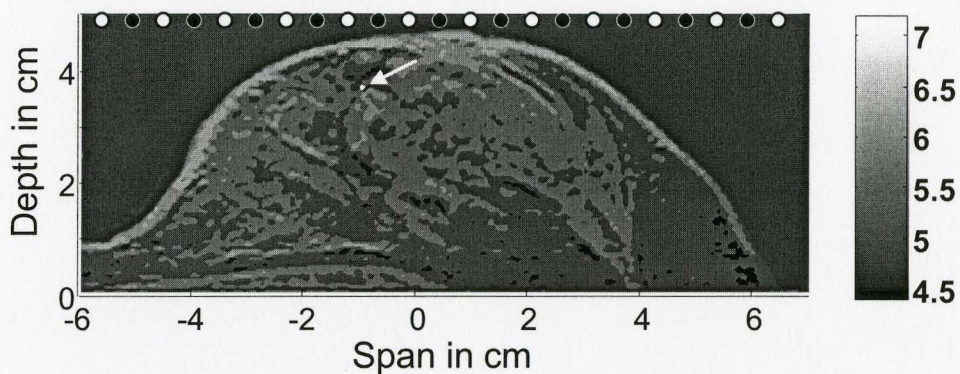
Both the data acquisition model and the TR model are implemented with the TLM method, with a grid size of $0.5 \text{ mm} \times 0.5 \text{ mm}$. The antenna locations are snapped to this grid. The forward model is based on a 2-D MRI image cross-section of the breast as seen in Fig. 4.1(a). Fig. 4.1(b) shows the dielectric profile for the inhomogeneous breast tissue. Fig. 4.2 shows the tumor and its permittivity contrast as compared to the surrounding medium.

The regions corresponding to the fibroglandular tissues in the breast are linearly mapped to higher permittivity and conductivity values than breast fat with an upper bound of 32% above the nominal values ($\epsilon_r = 4.58$ and $\sigma = 0.52 \text{ S/m}$) and lower bound of 16% greater than nominal values.

CHAPTER 4 ACHIEVING SUB-WAVELENGTH RESOLUTION WITH THE TLM-BASED SHANNON ENTROPY TR TECHNIQUE



(a)



(b)

Fig. 4.1 (a) The 2-D MRI data of a 57 year old female and (b) the corresponding 2-D dielectric profile of the inhomogeneous breast tissue with the 0.5-mm diameter tumor inserted at -0.95 cm span and 3.7 cm depth. The 23 receivers shown with circles are fed with alternating-phase voltage values.

CHAPTER 4 ACHIEVING SUB-WAVELENGTH RESOLUTION WITH THE TLM-BASED SHANNON ENTROPY TR TECHNIQUE

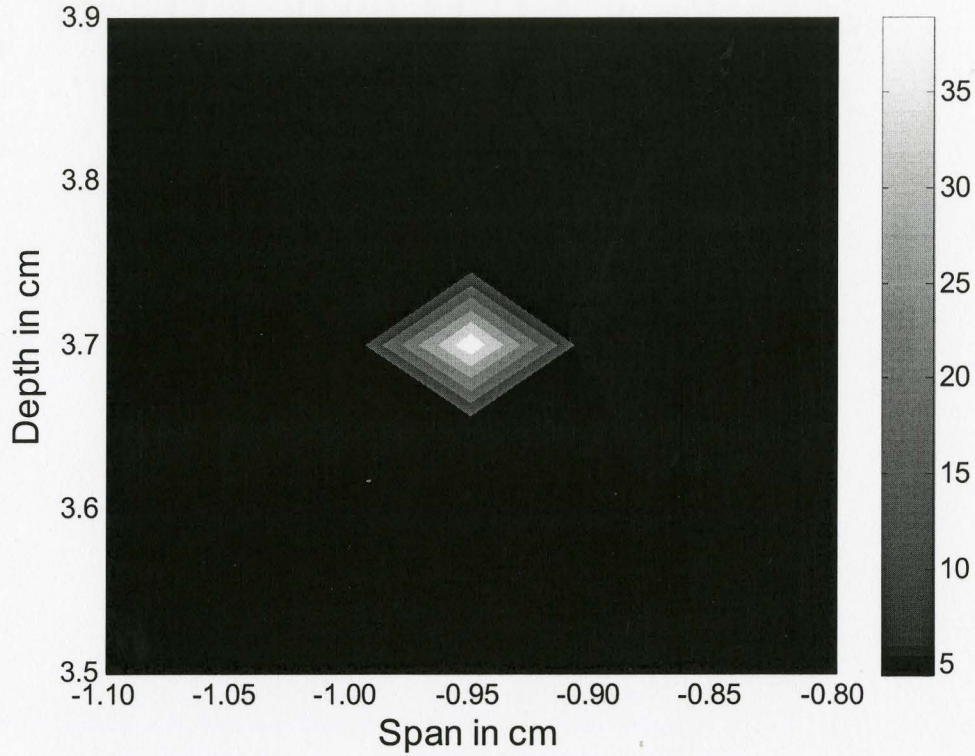


Fig. 4.2 Single breast dielectric profile of MRI-derived TLM model with a 0.5-mm diameter tumor inserted at -0.95 cm span and 3.7 cm depth.

Breast fat regions are mapped to values with $\pm 16\%$ variability from nominal breast fat values. The skin layer is artificially introduced and has dielectric values of $\epsilon_r = 31$ and $\sigma = 5.8$ S/m. The antenna receivers are subwavelength-size ($l = 5.7$ mm) apart. Because neighboring elements transmit with opposite polarity, there is a detectable backscattered field emanating from scatterers of subwavelength size.

4.4 TLM-BASED TR ALGORITHM USING MODIFIED SHANNON ENTROPY CRITERION (SEC)

The TLM-based TR algorithm using SEC is described for sub-wavelength microwave imaging. The algorithm incorporates the PSM concept in the forward or data acquisition model for sub-wavelength focusing. An FDTD TR algorithm that compensates for the ohmic losses was introduced in [3] through change of sign in the conductivity. Similarly, the proposed TLM TR algorithm has the ability to compensate for losses by introducing gain via change in the conductivity sign in the TLM normalized lossy stub conductance given by equation (3.4).

The TLM TR technique for the case of a TM-mode involves sequences of scattering and connection steps and was discussed in section 3.2. Similarly to the TR FDTD equations [3], if a point source radiates in free space and TR TLM equations are applied to all points in the grid, the wave will converge back to the source at the time corresponding to the maximum of the initial excitation. In [3], a minimum entropy criterion is employed based on the inverse varimax norm. Here we employ the SEC [8].

The SEC is given by equations (3.7) and (3.8) and its derivation is discussed in Section 3.3. The parameter D^k is a constant at time step k , which is related to the deviation of the node voltage values in a specified region around the peak value V_{peak}^k :

CHAPTER 4 ACHIEVING SUB-WAVELENGTH RESOLUTION WITH THE TLM-BASED SHANNON ENTROPY TR TECHNIQUE

$$D^k = std(X) \cdot std(Z) \quad (4.5)$$

where $std(\bullet)$ is the standard deviation and the vectors X and Z are

$$X = \left\{ \frac{V_y^k(i_{peak}-q, j)}{V_{ypeak}^k}, \frac{V_y^k(i_{peak}-q+1, j)}{V_{ypeak}^k}, \dots, \frac{V_y^k(i_{peak}+q, j)}{V_{ypeak}^k} \right\} \quad (4.6)$$

$$Z = \left\{ \frac{V_y^k(i, j_{peak}-m)}{V_{ypeak}^k}, \frac{V_y^k(i, j_{peak}-m+1)}{V_{ypeak}^k}, \dots, \frac{V_y^k(i, j_{peak}+m)}{V_{ypeak}^k} \right\}. \quad (4.7)$$

X is the variation along the x -coordinate and Z is the variation along the z -coordinate centered around the peak node. The values of m and q are bound by $\|2 \cdot q \cdot \Delta x\| \leq \Delta_k$ and $\|2 \cdot m \cdot \Delta z\| \leq \Delta_k$, where $\Delta x = \Delta z = 0.5$ mm and k is the time step. The parameter Δ_k determines the size of the specified region in which D^k is calculated. As in [8], $\Delta_k = 2$ cm.

The following is an outline of the steps in the algorithm [8]:

Step 1 Forward analysis of the breast model without tumor (*estimated healthy response*).

Note: Obtain the field solution using an averaged dielectric and conductivity estimate of the inhomogeneous breast tissue and skin layer.

Step 2 Forward analysis of breast model with tumor (*virtual measurement of realistic breast model*).

CHAPTER 4 ACHIEVING SUB-WAVELENGTH RESOLUTION WITH THE TLM-BASED SHANNON ENTROPY TR TECHNIQUE

Note: Obtain the field solution for the realistic heterogeneous breast model including tumor and skin layer. Once $V_y^t(x_i, z_i)$, the total response with tumor and breast medium, is obtained at each receiver at (x_i, z_i) , we find the particular tumor response

$$V_y^p(x_i, z_i) = V_y^t(x_i, z_i) - V_y^h(x_i, z_i) \quad (4.8)$$

The excitation signal for backpropagation at each receiver is then expressed as in equation (3.5) in section 3.2.

Step 3 TR backpropagation using TLM TR algorithm.

Note: Inject the response in equation (3.5) of the particular solution (*the backscattered fields stored at the receivers without clutter and noise*) in the reverse time sequence. The TLM TR model uses averaged estimates of the dielectric constant and conductivity. The TLM TR algorithm stops when SEC in equation (3.7) is minimized for all time steps.

4.5 RESULTS AND DISCUSSIONS

Both the forward model employing TLM [7] and the TLM TR algorithm are implemented within Matlab [14]. The maximum number of time steps in the TLM TR model is 3000. The TLM TR algorithm is run in reverse starting from

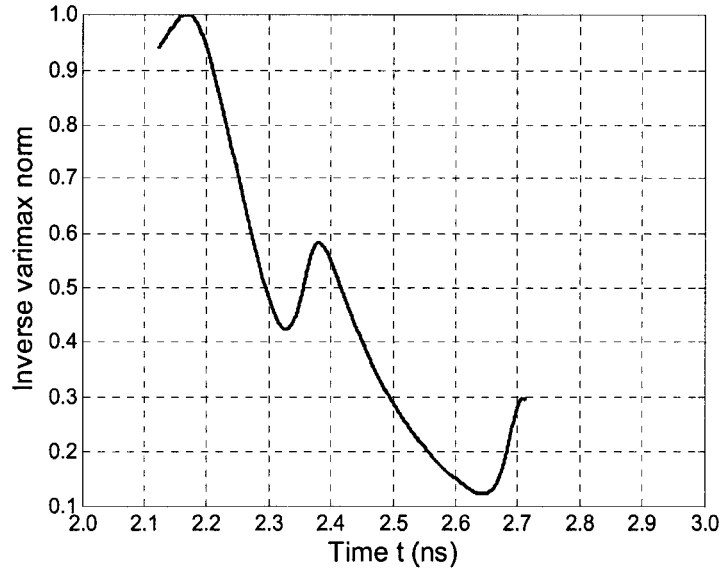
CHAPTER 4 ACHIEVING SUB-WAVELENGTH RESOLUTION WITH THE TLM-BASED SHANNON ENTROPY TR TECHNIQUE

time step 2500 since the recorded backscattered field at the receivers after that time step is very close to zero.

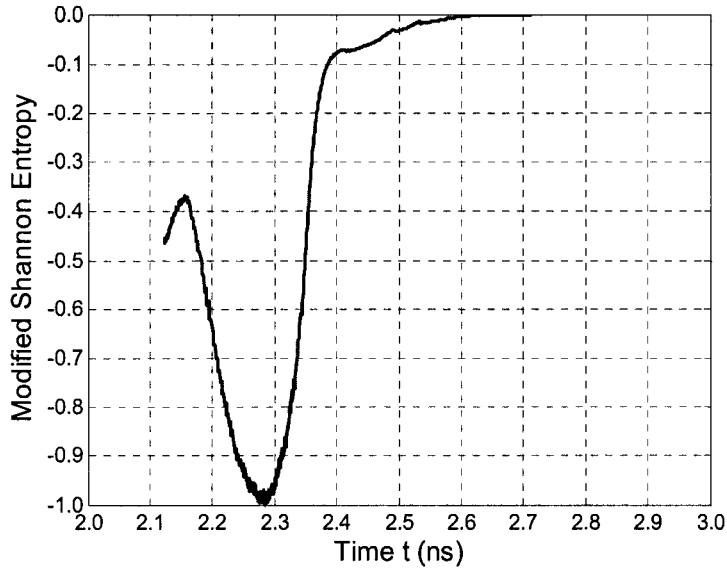
The 200-ps UWB pulse's shortest wavelength is large compared to the 0.5-mm diameter tumor. The excitation input to each antenna shown in Fig. 4.1(b) is a differentiated Gaussian pulse with full width at half maximum (FWHM) of 0.54 ns, and zero dc content. The shortest wavelength corresponds to the highest frequency in the spectrum of the pulse at 1% of the maximum, which is 4 GHz.

When using the TR technique and the inverse varimax norm as in [3] without incorporating the PSM technique, we obtain the inverse varimax norm vs. time shown in Fig. 4.3(a). The resultant image is shown in Fig. 4.4. The scatterer is not found because its size is below the diffraction limit of the pulse spectrum. There are also too many minima in the inverse varimax norm and thus it is not obvious where the algorithm should stop. On the other hand, the SEC, plotted vs. time in Fig. 4.3(b), demonstrates that the modified Shannon entropy is a robust minimum entropy criterion.

CHAPTER 4 ACHIEVING SUB-WAVELENGTH RESOLUTION WITH THE TLM-BASED SHANNON ENTROPY TR TECHNIQUE



(a)



(b)

Fig. 4.3 The response for: (a) the inverse varimax norm vs. time and (b) the modified Shannon entropy (SEC) vs. time. There is one minimum obtained at time step 1938 or 2.286 ns, where in (b), the wave converges to an optimal peak value.

CHAPTER 4 ACHIEVING SUB-WAVELENGTH RESOLUTION WITH THE TLM-BASED SHANNON ENTROPY TR TECHNIQUE

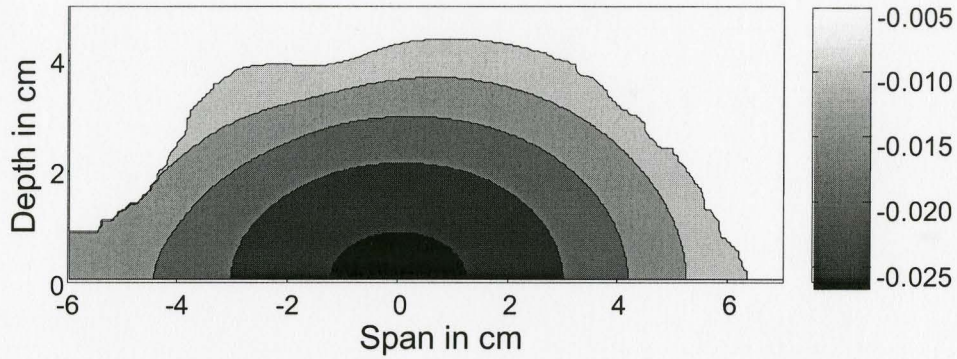


Fig. 4.4 The ghost image created by the TR technique with only one antenna transmitting in the forward model, all receivers transmitting in the TR model, and employing inverse varimax norm as in [3]. No scatterer is found.

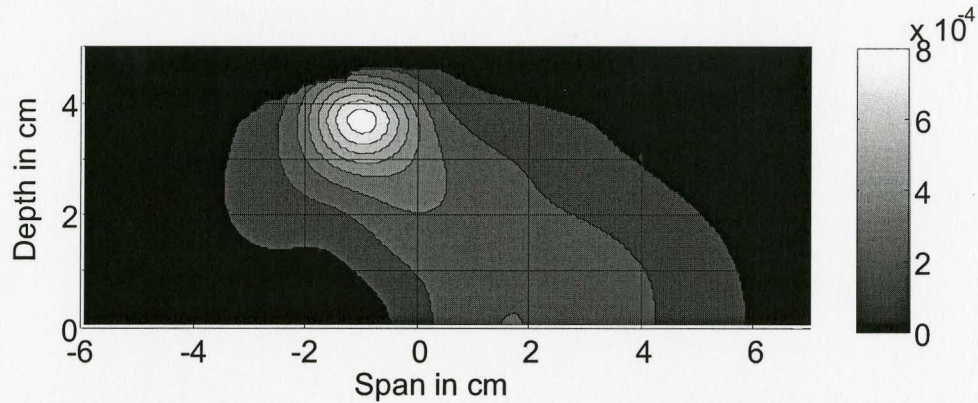


Fig. 4.5 The image obtained through the proposed TR technique with the TLM method and employing the concept of the PSM and the modified Shannon entropy.

CHAPTER 4 ACHIEVING SUB-WAVELENGTH RESOLUTION WITH THE TLM-BASED SHANNON ENTROPY TR TECHNIQUE

Fig. 4.5 shows the image detecting the 0.5-mm diameter tumor using the proposed TLM TR technique with the PSM and the modified Shannon entropy criterion. The image corresponds to the single minimum of the modified Shannon entropy obtained at time step 1938 or 2.286 ns. The wave converges to an optimal peak value. The tumor location found by the proposed algorithm uses a taper parameter of $\nu = 0.041 \cdot t_p$. It found the target at $[x, z] = [-1 \text{ cm}, 3.7 \text{ cm}]$ or -1 cm span and 3.7 cm depth while the actual location was at -0.95 cm span and 3.7 cm depth. The taper parameter plays an important role in compensating for dispersion and improving the resolution.

Fig. 4.6 shows the difference between the actual location of the tumor and the one found by the proposed algorithm using varying taper parameter values.

Although the tumor is detected for varying taper parameter values, the accuracy of the localization depends on it. The optimum taper parameter value of $\nu = 0.041 \cdot t_p$ is found by minimizing the difference between the location detected by the algorithm and actual location of the 0.5-mm size tumor, which is 1.2 cm from the receivers, within the accuracy of the grid size.

CHAPTER 4 ACHIEVING SUB-WAVELENGTH RESOLUTION WITH THE TLM-BASED SHANNON ENTROPY TR TECHNIQUE

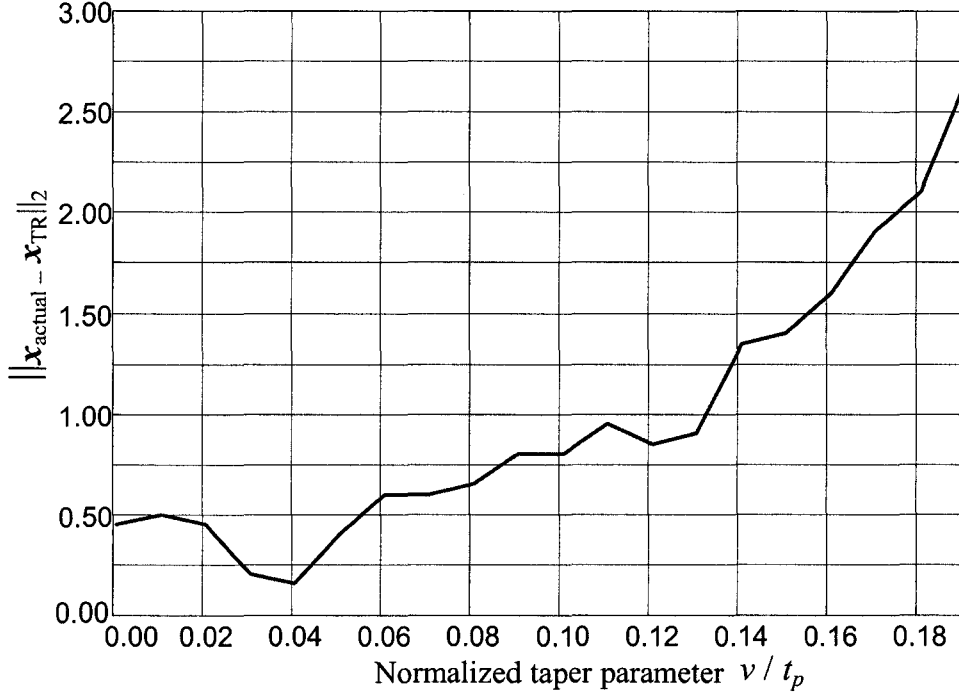


Fig. 4.6 The difference between the actual location of the tumor and the one found by the proposed TLM TR algorithm using varying taper parameter values. The location of the tumor is -0.95 cm span and 3.7 cm depth.

For all cases of varying taper parameter values, the TR algorithm using PSM and the modified Shannon entropy finds only one minimum. The corresponding location is denoted x_{TR} . Fig. 4.6 shows how the L2 norm difference between x_{actual} and x_{TR} increases as the taper parameter increases due to the increase in the width of the temporal window. The focusing resolution is increased as the taper parameter decreases.

4.6 EFFECT OF DIELECTRIC CONTRAST

The robustness of the modified SEC and the experimental setup is examined by changing the dielectric contrast of the breast medium. Table 4.1 compares the location found by our TLM TR algorithm for varying dielectric contrast. The taper parameter ($\nu = 0.041 \cdot t_p$) is fixed as in section 4.5 and the experimental setup is as in section 4.3. Only the dielectric contrast is altered while the forward and the TR simulations are performed with the MRI-derived breast model.

As the contrast is decreased from 6:1 to 1.3:1, the difference between \mathbf{x}_{TR} and \mathbf{x}_{actual} increases moderately. The tumor is detected in all the cases.

TABLE 4.1
COMPARISON OF DIELECTRIC CONTRAST ON DETECTION OF TUMOR

| Phantom Number Fat Peak (ϵ_r, σ) Fibroglandular Peak (ϵ_r, σ) | Dielectric Contrast between normal breast tissue and tumor ($\epsilon_r = 39$) | Location found by proposed algorithm (actual at -0.95 cm, 3.7 cm) |
|--|---|---|
| #1 (5.3, 0.60) (6.05, 0.69) | 6:1 (note: 9:1 in [3]) | (-1.00 cm, 3.7 cm) |
| #2 (17.34, 0.75) (19.73, 0.86) | 2:1 | (-0.95 cm, 3.30 cm) |
| #3 (22.98, 0.85) (26.15, 0.96) | 1.5:1 | (-0.95 cm, 3.25 cm) |
| #4 (26.37, 1.00) (30, 1.15) | 1.3:1 | (-0.95 cm, 3.25 cm) |

4.7 TLM-BASED TR ALGORITHM EMPLOYING TWO TRMs

In this section, we examine the use of two time-reversal mirrors (TRMs) perpendicular to each other and closer to the scatterers than the single plane TRM. By studying the TRM and its performance in localizing the tumor as the sub-wavelength sized tumor is moved within the inhomogeneous breast medium vertically away from the plane of recording antenna receivers, we find that the evanescent waves are lost for tumors deep in the breast and away from the skin-breast interface. The accuracy of localizing the tumor is affected because not enough waves scattered from the tumor are recorded at the TRM. We thus develop and study the TLM-based TR algorithm employing two TRMs.

Another set of measurement or forward simulation using an array of 9 receivers/transmitters located at a small distance from the breast along the depth dimension, and placed every $10 \times \Delta l$ with $\Delta l = 0.57$ mm. Then we employ the same setup as in section 4.3 but letting these 9 transmitters/receivers be located perpendicular to the 23 antennas. These nine antennas transmit pulses of alternating polarity in the forward model. The backscattered fields are recorded and used in the TR model to time reverse fields to the source.

A new taper parameter $\nu_2 = 0.03 \cdot t_{p2}$ is introduced for the backscattered fields coming from the additional antennas. The input signal at these receivers is then

CHAPTER 4 ACHIEVING SUB-WAVELENGTH RESOLUTION WITH THE TLM-BASED SHANNON ENTROPY TR TECHNIQUE

$$f_i(t) = V_y(x_i, z_i) \cdot \exp\left(-\left(\frac{t - t_{p2}}{\nu_2}\right)^2\right) \quad (4.9)$$

where t_{p2} is the time instant when the peak of the received waveform $V_y^{p2}(x_i, z_i)$ from the second TRM occurs for a short pulse excitation, and ν is the taper parameter, which determines the width of the impulse temporal window function. The location of each receiver determines the coordinates of (x_i, z_i) where $i = 1, \dots, M$ and M is the number of receivers for the second TRM ($M = 9$).

The algorithm is modified from the one in section 4.4. The following is an outline of the steps in the algorithm:

Step 1 Simulate forward analysis with only the first 23 TRM receivers of breast model without tumor (*estimated healthy response*).

Note: Obtain the field solution using an averaged dielectric and conductivity estimate of the inhomogeneous breast tissue and skin layer.

Step 2 Simulate forward model with only the first TRM receivers of breast model with tumor (*virtual measurement of realistic breast model*).

Note: Obtain the field solution for the realistic heterogeneous breast model including tumor and skin layer. Once $V_y^t(x_i, z_i)$ is obtained at each receiver at (x_i, z_i) , we find the particular tumor response as in equation (4.8). The excitation signal for

CHAPTER 4 ACHIEVING SUB-WAVELENGTH RESOLUTION WITH THE TLM-BASED SHANNON ENTROPY TR TECHNIQUE

backpropagation at each receiver is then expressed as in equation (3.5) in section 3.2.

Step 3 Simulate forward analysis with the second 9 TRM receivers of breast model without tumor (*estimated healthy response*).

Note: Obtain the field solution using an averaged dielectric and conductivity estimate of the inhomogeneous breast tissue and skin layer.

Step 4 Simulate forward analysis with the second TRM receivers of breast model with tumor (*virtual measurement of realistic breast model*).

Note: Obtain the field solution for the realistic heterogeneous breast model including tumor and skin layer. Once $V_y^t(x_i, z_i)$ is obtained at each receiver at (x_i, z_i) , we find the particular tumor response

$$V_y^{p2}(x_i, z_i) = V_y^t(x_i, z_i) - V_y^h(x_i, z_i) \quad (4.10)$$

The excitation signal for backpropagation at each receiver is then expressed as in equation (4.9).

Step 5 TR Backpropagation using TLM TR algorithm.

Note: Inject the responses for both the TRMs in Equation (3.5) and Equation (4.9) of the particular solutions (*the backscattered*

CHAPTER 4 ACHIEVING SUB-WAVELENGTH RESOLUTION WITH THE TLM-BASED SHANNON ENTROPY TR TECHNIQUE

fields stored at the receivers without clutter and noise) in the reverse time sequence. The TLM TR model uses averaged estimates of the dielectric constant and conductivity. The TLM TR algorithm stops when SEC in Equation (3.7) is minimized for all time steps.

4.7.1 Results and Discussion

The experimental setup uses two TRMs and the same dielectric profile for the breast medium as in section 4.3. A 0.5-mm diameter tumor is inserted inside. Fig. 4.7 shows the image and the improvement in localization obtained using the initial 23 receivers and additional antennas placed parallel to the z-axis in the TR model.

CHAPTER 4 ACHIEVING SUB-WAVELENGTH RESOLUTION WITH THE TLM-BASED SHANNON ENTROPY TR TECHNIQUE

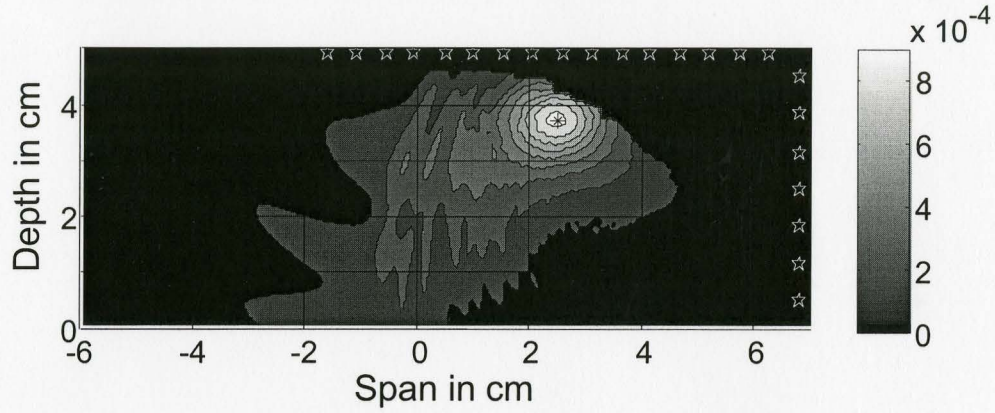


Fig. 4.7 The image obtained using two TRMs through the proposed TR technique with TLM method and employing the concept of PSM and SEC. The taper parameters are $\nu = 0.038 \cdot t_p$ and $\nu_2 = 0.003 \cdot t_p$. The 0.5-mm diameter tumor is shown by a black asterisk and the receivers in the TR model are denoted by stars.

The improved effect in localization by the use of the second TRM is shown for the case where the 0.5-mm diameter tumor is located at 0.75 cm depth and 4 cm span. When using just one TRM and a taper parameter $\nu = 0.019 \cdot t_p$, the resulting image is shown in Fig. 4.8. The same setup is used with now two perpendicular TRM and the resulting image is shown in Fig. 4.9.

CHAPTER 4 ACHIEVING SUB-WAVELENGTH RESOLUTION WITH THE TLM-BASED SHANNON ENTROPY TR TECHNIQUE

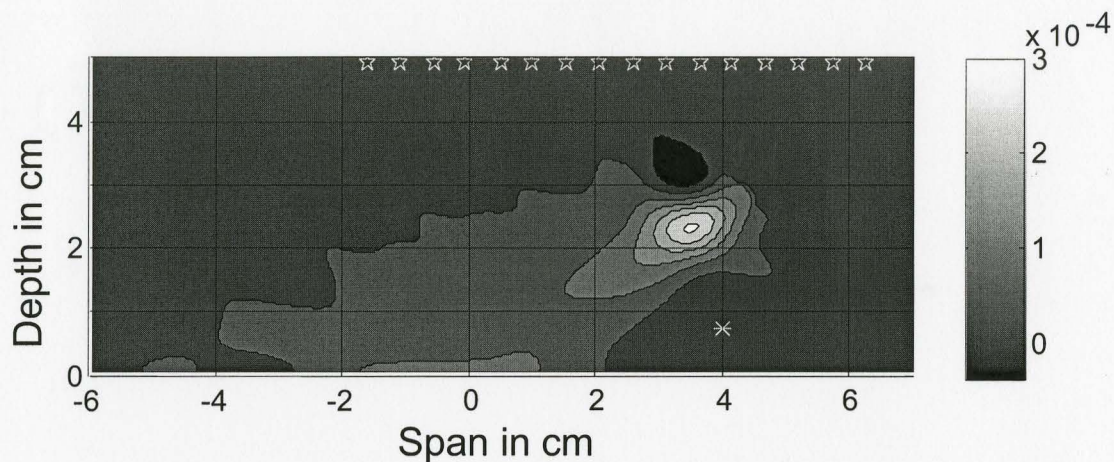


Fig. 4.8 The image obtained using a single TRM, employing the concept of PSM and using SEC. The taper parameter is $\nu = 0.019 \cdot t_p$. The 0.5-mm diameter tumor is shown by a white asterisk and the receivers in the TR model are shown by stars.

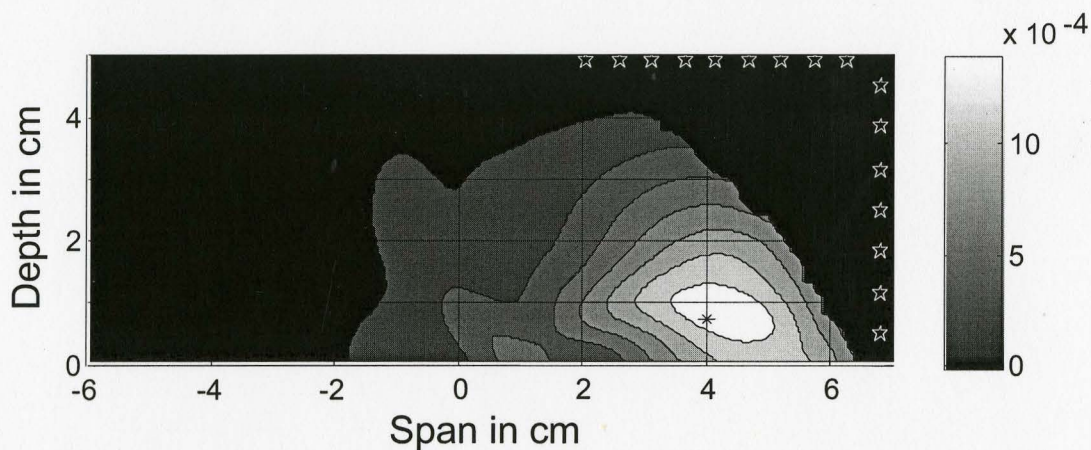


Fig. 4.9 The image obtained using two TRMs, employing the concept of PSM and using SEC. The taper parameters are $\nu = 0.019 \cdot t_p$ and $\nu_2 = 0.215 \cdot t_{p2}$. The 0.5-mm diameter tumor is shown by a black asterisk and the receivers in the TR model are denoted by stars.

4.7.2 Effect of Chest Wall

Fig. 4.10 shows the 2-D dielectric profile of the inhomogeneous breast tissue including the muscle chest wall and a 0.5-mm diameter tumor located close to the chest wall ($\epsilon_r = 26$, $\sigma = 3.8$ S/m).

The image obtained using the two TRMs with taper parameter values of $\nu = 0.019 \cdot t_p$ and $\nu_2 = 0.215 \cdot t_{p2}$ is shown in Fig. 4.11. The actual location of the tumor is shown in a red asterisk.

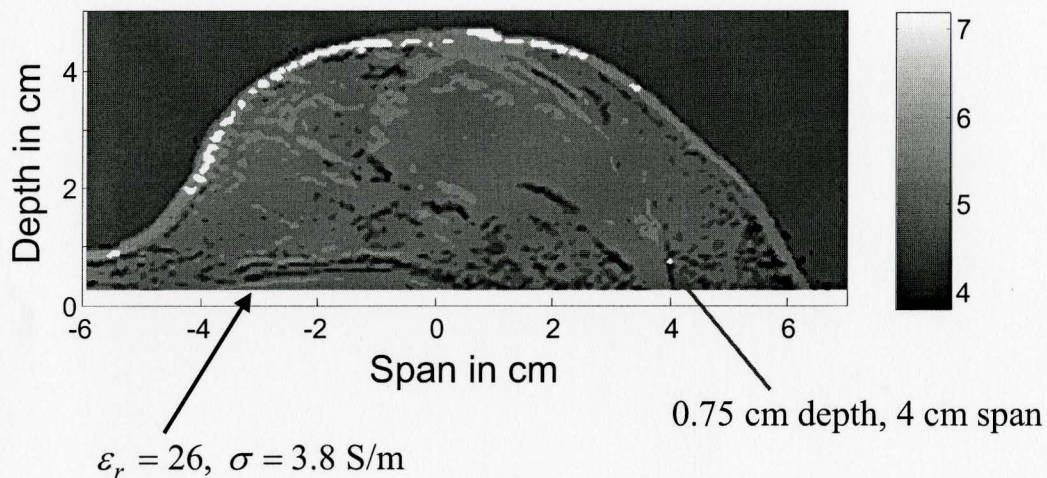


Fig. 4.10 The 2-D dielectric profile of the inhomogeneous breast tissue including the muscle chest wall and a 0.5-mm diameter tumor located close to the chest wall.

CHAPTER 4 ACHIEVING SUB-WAVELENGTH RESOLUTION WITH THE TLM-BASED SHANNON ENTROPY TR TECHNIQUE

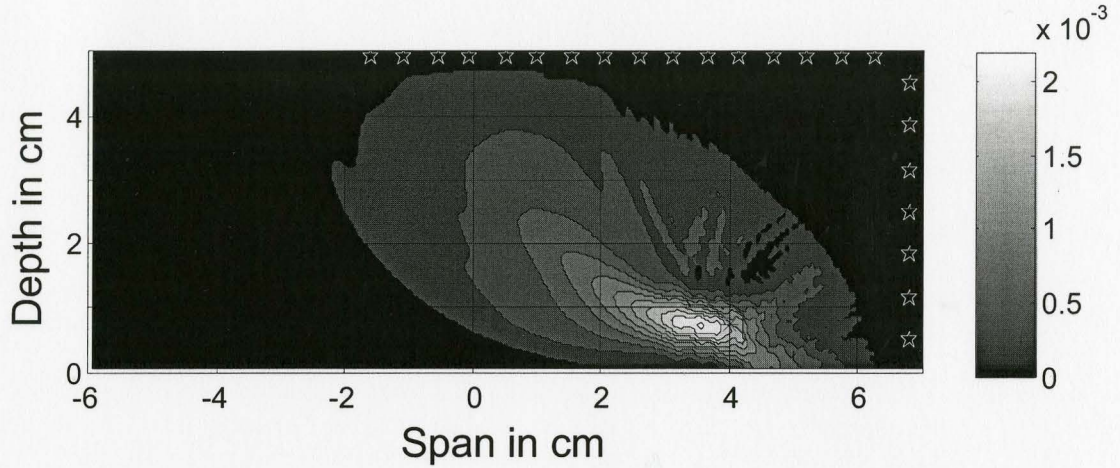


Fig. 4.11 The image obtained using two TRMs, employing the concept of PSM and using SEC. The taper parameters are $\nu = 0.019 \cdot t_p$ and $\nu_2 = 0.215 \cdot t_{p2}$. The 0.5-mm diameter tumor is shown with a red asterisk and the receivers in the TR model are shown as stars. The back-propagating waves focus to a location slightly different from the actual location because of the chest wall reflections.

4.8 CONCLUDING REMARKS

A novel approach to the detection of tumors well below a centimeter using a sub-wavelength ultrawide band (UWB) microwave radar imaging technique based on the principles of phase-shifting mask (PSM), time reversal and a modified Shannon entropy criterion (SEC) [8] was presented and discussed. A 0.5-mm diameter tumor was detected and located using a 200-ps UWB pulse in an inhomogeneous 2-D breast model. We report the first simulation results obtained using a subwavelength focusing technique where a focal spot of size less than $1/60^{\text{th}}$ of a wavelength is obtained. TR has been shown to be superior to other

CHAPTER 4 ACHIEVING SUB-WAVELENGTH RESOLUTION WITH THE TLM-BASED SHANNON ENTROPY TR TECHNIQUE

simple delay-based focusing techniques and here we have extended the TR algorithm by making it more robust in localizing sub-wavelength size tumors.

The origin of the diffraction limit and proposed way to overcome it using time-reversal and phase-shifting mask (PSM) technology was discussed. The TLM-based TR algorithm using SEC was described and the effect of the dielectric contrast on the detection of tumors of sub-wavelength size was analyzed. Since the evanescent waves are lost when the subwavelength scatterer is deep in the breast medium far from the TRM, a TLM-based TR algorithm employing two TRMs was proposed and discussed.

REFERENCES

- [1] E. C. Fear, X. Li, S. C. Hagness, and M. Stuchly, "Confocal microwave imaging for breast cancer detection: Localization of tumors in three dimensions," *IEEE Trans. Biomed. Eng.*, vol. 49, pp. 812–822, 2002.
- [2] E. J. Bond, S. C. Hagness, and B. D. Van Veen, "Microwave imaging via space-time beamforming for early detection of breast cancer," *IEEE Trans. Antennas Propagat.*, vol. 51, no. 8, pp. 1690-1705, 2003.
- [3] P. Kosmas and C. M. Rappaport, "Time reversal with the FDTD method for microwave breast cancer detection," *IEEE Trans. Microwave Theory Tech.*, vol. 53, no. 7, pp. 2317-2323, July 2005.
- [4] P. Kosmas and C. M. Rappaport, "A matched-filter FDTD-based time reversal approach for microwave breast cancer detection," *IEEE Trans. Antennas Propagat.*, vol. 54, no. 4, pp. 1257-1264, April 2006.
- [5] D. M. Hailu, "Review of ultrawideband microwave radar imaging techniques for breast cancer detection," Computational Electromagnetics Lab Technical Report, CEM-R-38, January 2007.

CHAPTER 4 ACHIEVING SUB-WAVELENGTH RESOLUTION WITH THE TLM-BASED SHANNON ENTROPY TR TECHNIQUE

- [6] M. D. Levenson, N. S. Viswanathan, and R. A. Simpson, "Improving resolution in photolithography with a phase-shifting mask," *IEEE Trans. Electron Devices*, ED-29, no. 12, pp. 1828-1836, 1982.
- [7] C. Christopoulos, *The Transmission-Line Modeling (TLM) method in Electromagnetics*. Morgan & Claypool Publishers, San Rafael, CA, USA, 2006.
- [8] D. M. Hailu, N. K. Nikolova, M. H. Bakr, "Sub-wavelength microwave radar imaging for detection of breast cancer tumors," in *2007 IEEE Int. Microwave Symp. on Signals, Systems, and Electronics*, pp.107-110, Montréal, Canada, July 2007.
- [9] A. B. Kahng and Y. C. Pati, "Subwavelength optical lithography: challenges and impact on physical design," in *1999 Int. Symp. on Physical Design*, pp. 112-119, 1999.
- [10] D. Cassereau and M. Fink, "Time-reversal of ultrasonic fields. III. Theory of the closed time-reversal cavity," *IEEE Trans. Ultrason. Ferroelectr. Freq. Control*, vol. 39, pp. 579-592, Sept. 1992.
- [11] J. de Rodny and M. Fink, "Overcoming the diffraction limit in wave physics using a time-reversal mirror and a novel acoustic sink," *Phys. Rev. Lett.* vol. 89, 124301, 2002.
- [12] G. Lerosey, J. de Rosny, A. Tourin and M. Fink "Focusing beyond the diffraction limit with far-field time reversal," *Science Mag.*, vol. 315. no. 5815, pp. 1120 – 1122, February 23, 2007.
- [13] R. Carminati, J. J. Saenz, J.-J. Greffet, M. Nieto-Vesperians, "Reciprocity, unitarity, and time-reversal symmetry of the S matrix of fields containing evanescent components," *Phys. Rev.*, vol. A 62, 012712, 2000.
- [14] MATLAB™ 7.1, The MathWorks Inc., 3 Apple Hill Drive, Natick, MA, 2005.

CHAPTER 5

NARROWBEAM

ULTRAWIDEBAND ANTENNAS

FOR MICROWAVE BREAST

CANCER DETECTION

5.1 INTRODUCTION

Ultra wideband (UWB) technology presents a revolutionary approach to wireless communications but is certainly not a new concept. The first UWB radio was the pulse-based Spark Gap radio, developed by Guglielmo Marconi in the late 1800's. The radio was used to transmit Morse code. By the 1980's, antenna advances made possible the impulse based transmission for radar and communications. In 1989, the U.S. Department of Defense started using the term 'Ultra Wideband' for baseband, or impulse technology and in 2002 the Federal Communication Commission (FCC) allocated the UWB spectrum. Since then, many researchers are exploring antenna designs, circuit designs, system designs and RF designs related to UWB applications [1][2][3].

CHAPTER 5 NARROWBEAM ULTRAWIDEBAND ANTENNAS FOR MICROWAVE BREAST CANCER DETECTION

UWB antennas are fundamental components of UWB radar imaging systems. Some UWB antennas have been developed for biomedical imaging applications. Many UWB radar imaging systems employ these antennas for transmitting and receiving short-duration UWB pulses. Consequently, studying the radiation and reception properties of these antennas is vital to determine their suitability for such applications.

One of the challenges associated with designing UWB antenna elements for application to breast cancer detection is the mismatch in dielectric properties at the skin interface generating a scattering response at least one order of magnitude larger than any tumor response. Further, other challenges include meeting antenna specifications and feasibility of fabrication. It would be ideal for these antennas to also remove or suppress skin interface artifacts with minimum distortion to the tumor response. In terms of experimental implementation, the challenges include the management of the aperture size, scan time, cost, broadband impedance matching, directivity, efficiency, and gain.

Transmission and reception by conventional UWB antennas are discussed and summarized in [1]. The report on narrowbeam ultrawideband antennas for microwave breast cancer detection [4] summarizes the advantages and disadvantages of the ultrawideband (UWB) antennas designed for microwave radar-based tumor detection. It describes proposed narrowbeam ultrawideband antennas. The report also compares feed structures and antenna designs explored for UWB near-field imaging applications. These comparisons include feasibility

CHAPTER 5 NARROWBEAM ULTRA WIDEBAND ANTENNAS FOR MICROWAVE BREAST CANCER DETECTION

of fabrication [4]. Many antennas can have improved impedance matching by using resistive loading at the cost of efficiency [1]. To reduce reflections from the antenna and to reduce dispersion, resistive-loading with certain profile is employed as in the Wu-King cylindrical antenna [5].

Prior UWB antennas designed for biomedical microwave radar imaging for the detection of breast cancer tumors include the bowtie [7][8], ridged pyramidal horn [9][10], microstrip-fed “Dark Eyes” [11][12] and slot [13] UWB antennas. The Wu-King cylindrical antenna is re-designed in [6] for applications to radar-based breast cancer detection. A resistively loaded Wu-King antenna is fabricated and soldered to an SMA connector and attached to a metal plug. But all these implementations have four key disadvantages. The first is that they are designed to operate close to the breast medium and immersed in coupling medium and not designed to work in contact with skin, i.e. as in ultrasound. The coupling medium complicates the hardware and maintenance. It may also be a health hazard when used with multiple patients. The second is that these antennas have dispersive radiation patterns. The patterns have multiple maxima and for the case of [13], the patterns split in the middle. The final disadvantage is that they do not have directional properties. The antennas radiate outside the human body and are susceptible to external interferences.

The TEM horn antenna has highly directive properties and can achieve UWB impedance matching with reduced dispersion [1]. In Section 5.2, we review the TEM horn antenna, followed by antenna specifications and objective

CHAPTER 5 NARROWBEAM ULTRA WIDEBAND ANTENNAS FOR MICROWAVE BREAST CANCER DETECTION

described in Section 5.3, and the first steps towards a completely novel antenna for UWB applications is examined in Section 5.4. The printed tapered TEM horn antenna with different feed structures is discussed in Section 5.4, followed by concluding remarks in Section 5.5.

5.2 REVIEW: TEM HORN ANTENNA [1][4]

UWB antennas are designed to operate within the Federal Communication Commission (FCC) allocated 7.5 GHz bandwidth from 3.1 GHz to 10.6 GHz. In order to understand the challenges of UWB antenna design, a comprehensive background outlining several antenna parameters are presented in the next section. Here the tapered TEM horn antenna and the double-ridged pyramidal horn antenna are reviewed.

5.2.1 Tapered TEM Horn Antenna [1]

A receiving TEM horn antenna in theory can give a direct measurement of an incident wave [1]. In [1], several ultrawideband antenna design techniques are discussed including the advantages of tapering, converting resonating structures to travelling-wave structures and reducing dispersion by resistive loading. It was experimentally found that the impulse response in the transmitting mode is proportional to the time derivative of the impulse response in the receiving mode of the antenna.

CHAPTER 5 NARROWBEAM ULTRA WIDEBAND ANTENNAS FOR MICROWAVE BREAST CANCER DETECTION

The design descriptions of the tapered horn antenna are in [1]. The antenna was simulated from 200 MHz to 40 GHz with the width of the input pulse being 133.3 ps, and the time support of the response determined by the lowest frequency of operation was 5 ns. The duration of the pulse or pulse width is chosen to correspond to the operating bandwidth of the UWB antenna. The radiated time-domain field was linearly polarized along the z axis. The tapering of the TEM horn reduces reflections and unwanted oscillation when the antenna receives z polarized monocycle field propagating along the x axis.

Although the reflections are significantly reduced due to the tapering, the radiated field is not the same as the derivative of the input pulse as proposed in [1][14] due to resonance effects in the antenna structure. The reflections can be further reduced by transforming the resonating structure into a traveling-wave one.

To do this, the lengths of the parallel plates near the feed point are reduced. In addition, to reduce the dispersion, a resistive loading was applied with the following profile [1]:

$$r^i(\kappa) = \frac{60\Re\{\psi\}}{h - |\kappa|} \quad (5.1)$$

where

$$\psi = 2 \left[\sinh^{-1} \frac{h}{r} - C(2kr, 2kh) - jS(2kr, 2kh) \right] + \frac{j}{kh} (1 - e^{-j2kh}) \quad (5.2)$$

CHAPTER 5 NARROWBEAM ULTRA WIDEBAND ANTENNAS FOR MICROWAVE BREAST CANCER DETECTION

and κ is a dimension such as the axial coordinate [5], r^i is the internal resistance for an antenna with height of $2h$ and radius r [1][5]. $C(a, x)$ is the generalized cosine integral and $S(a, x)$ is generalized sine integral.

The radiated waveform and time-domain received current for the non-resonating taper horn antenna are shown in [1]. The figures show that the radiated field is similar to the derivative of the input voltage while the induced current is the same as the incident wave.

5.2.2 Double-Ridged Pyramidal Horn Antenna

Past implementation of UWB horn antennas transmitting/receiving microwave energy used for microwave breast-cancer detection include the modified version of a double-ridged pyramidal horn antenna [15][16]. The waveguide section is eliminated, and one of the two ridges is replaced by a curved metallic plane terminated by resistors. The generic form of this configuration has been proposed in [17]. The design is customized to centimetre-scale dimensions for operation in the microwave frequency range operating in free space [9]. In [18], an experimental and numerical time-domain characterization of the UWB antenna immersed in the phantom's coupling medium (soybean oil) is presented.

The main structure of the horn antenna includes a pyramidal horn radiation cavity, metallic ridges, and curved metallic launching plane terminated with resistors [18]. The pyramidal horn is connected to the outer conductor of the coaxial feed via a Sub Miniature version A (SMA) connector and serves as the

CHAPTER 5 NARROWBEAM ULTRA WIDEBAND ANTENNAS FOR MICROWAVE BREAST CANCER DETECTION

ground plane. The depth of the pyramidal horn is 1.3 cm and the aperture dimensions are 2.5 cm by 2.0 cm. The curved planar launching plane is connected to the central conductor of the coaxial feed. It curves toward one of the sidewalls of the pyramidal horn and tapers toward the feed point. Two 100- Ω termination resistors are connected in parallel near opposite corners of the launching plane to suppress reflections from the end of the launching plane. A ridge is attached to the interior side of the horn-shaped ground plane opposite to the curved launching plane. The top surface of the ridge curves from the feed point toward the antenna aperture [18].

In [18], a 3-D FDTD model of the UWB antenna is simulated. The grid size is 0.5 mm \times 0.5 mm \times 0.5 mm. The curved or flared metal surfaces of the antenna are modeled using a staircase approximation. The antenna excitation is implemented using a 1.0-V 50- Ω resistive voltage source across the gap [19]. The 100- Ω termination resistors attached to the end of the launching plane are incorporated into the FDTD model using a lumped circuit element formulation [19]. The FDTD grid is terminated with a Berenger perfectly matched layer (PML) absorbing boundary condition [20].

Both the TEM horn and the pyramidal horn antennas have very good performance in terms of a narrowbeam radiation pattern, polarization, high gain, beamwidth, voltage standing wave ratio, and return loss. It is noted that resistive loading improves the return loss and impedance matching but at the cost of efficiency. These improvements of the bandwidth, gain and broadband

CHAPTER 5 NARROWBEAM ULTRA WIDEBAND ANTENNAS FOR MICROWAVE BREAST CANCER DETECTION

impedance matching, however, are at the cost of large physical size and difficult fabrication. These antennas are expensive and can not be utilized in cases where we need small antennas in an array. This is due to the limited surface area of the breast. Another factor to consider is the ability to integrate the antenna transmitter and receiver on the same circuit.

Thus small planar antennas that can achieve the aforementioned transmission and reception characteristics are desired.

5.3 ANTENNA SPECIFICATIONS

Several fundamental antenna parameters are considered in determining the optimal specifications. The challenging requirements for UWB antenna design in breast cancer detection is presented below.

5.3.1 Fundamental Antenna Parameters [21]

The performance of an antenna is described by various parameters, of which some are interrelated, and so not all are needed for a complete description. Among the most fundamental parameters for UWB antenna design are the bandwidth, the radiation pattern, and the gain. Further, the beamwidth, directivity, polarization, and efficiency are discussed.

The bandwidth indicates the range of frequencies within which the impedance of the antenna is sufficiently matched to its input transmission line impedance such that the return loss and the Voltage Standing Wave Ratio

CHAPTER 5 NARROWBEAM ULTRA WIDEBAND ANTENNAS FOR MICROWAVE BREAST CANCER DETECTION

(VSWR) are less than a specified standard. For antennas with ultra-wide bandwidths, the upper frequency can be 3 times greater than the lower (3:1 or greater). The VSWR and the return loss are dependent on the reflection coefficient Γ defined in equation (5.3) below. Γ measures the complex ratio of the reflected wave to the incident wave at a transmission line load. Fig. 5.1 shows the transmission line loaded with an antenna.

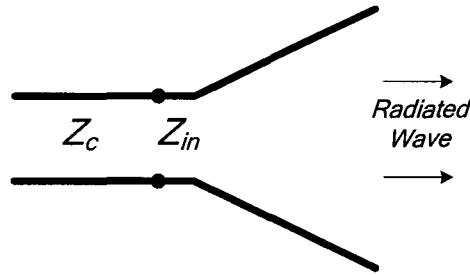


Fig. 5.1 Antenna in transmitting mode connected to a transmission line.

$$\Gamma = \frac{Z_{in} - Z_c}{Z_{in} + Z_c} \quad (5.3)$$

$Z_{in} = (R_r + R_L) + jX_{in}$ is the antenna input impedance and Z_c is the characteristic impedance of the transmission line. R_r is the radiation resistance of the antenna and R_L is its loss resistance.

Most network analyzers give scattering parameter matrix values and the S_{11} parameter is the reflection coefficient Γ . The goal of impedance matching is to achieve $|\Gamma| = 0$ or perfect transmission. The return loss is defined as

CHAPTER 5 NARROWBEAM ULTRA WIDEBAND ANTENNAS FOR MICROWAVE BREAST CANCER DETECTION

$$\text{return loss} = 20 \log(|\Gamma|) \quad (5.4)$$

The VSWR is given by

$$\text{VSWR} = \frac{V_{\max}}{V_{\min}} = \frac{1 + |\Gamma|}{1 - |\Gamma|}. \quad (5.5)$$

A good value for VSWR is 2.0 or less. This measure is important because if the antenna load is not perfectly matched to the transmission line, reflections at the load cause unwanted standing waves in the transmission line.

Ultimately, the power reflected at the terminals of the antenna has to be reduced for good impedance matching. The acceptable range of values for Γ that allows only 10% reflected power is 0.3162. This is because we want to maximize the radiated power.

5.3.2 Objective [4]

Practical low cost design and fabrication of UWB antennas is paramount for any UWB microwave imaging system that can be used in clinical trials. The antenna is also an integral part of the imaging tool for detecting small malignant breast tumors, without distortion from the skin and the clutter generated by the natural heterogeneity of normal breast tissue. In addition, the antenna has to be easy to fabricate, while the imaging system must ensure comfort for the patient and ease of maintenance.

CHAPTER 5 NARROWBEAM ULTRA WIDEBAND ANTENNAS FOR MICROWAVE BREAST CANCER DETECTION

The following design requirements are specified:

1. Operate in the frequency band 3.1 to 10.6 GHz.

The operating frequency band is in the microwave UWB. As in the basic UWB radar configuration, a transmitting antenna radiates extremely short duration (hundreds of picoseconds to nanoseconds) bursts of RF/microwave energy.

2. Avoid the use of a coupling medium.

The coupling medium of soybean oil or canola oil is used in most radar-based microwave imaging, which is inconvenient for women, who need frequent checkups for breast-cancer detection and diagnosis.

3. Low cost.

Most of the horn antennas and resistive monopole antennas designed for active microwave imaging techniques are costly. Antennas manufactured on printed-circuit-boards (PCB) by etching are very cost effective.

CHAPTER 5 NARROWBEAM ULTRAWIDEBAND ANTENNAS FOR MICROWAVE BREAST CANCER DETECTION

4. Linear polarization operating in the dominant TEM mode.

We need to know the polarization of the wave penetrating the breast tissue. This may require incorporation of a depolarizer to remove horizontally polarized wave. A linearly polarized electric field is required.

5. No losses and impedance matching with human breast tissue

We aim at a return loss less than -10 dB in the UWB region. The dielectric used for the antenna has to have similar averaged permittivity as the adipose tissue found in the breast.

6. Reduce noise.

The signal-to-noise (S/N) ratio is defined as the ratio of the maximum tumor energy to the maximum noise energy in the tumor-free phantom. The tumor response in the received waveforms contributes to “signal,” while “noise” is introduced by residual artifacts associated with antenna reverberation and reflections from the skin–breast interface, as well as conventional instrument noise. It is desirable to maximize the signal-to-clutter ratio.

CHAPTER 5 NARROWBEAM ULTRA WIDEBAND ANTENNAS FOR MICROWAVE BREAST CANCER DETECTION

7. Add band notch at 5.15-5.825 GHz (Optional)

For UWB antennas not to interfere with the IEEE 802.11a based systems, the antennas can be re-designed to add a band notch at 5.15-5.825 GHz. This is applicable to using the UWB radar imaging system in areas where there are wireless network transmissions.

5.4 PRINTED TAPERED TEM HORN ANTENNA WITH DIFFERENT FEED STRUCTURES

The Vivaldi antenna was first designed for wideband applications in 1979 [23] fed by a wideband balun transformer. Its advantages are its planar configuration; otherwise it has the same quality as TEM horn in terms of reduction in pulse distortion. Furthermore, it can be integrated onto the same circuit board as Tx and Rx [24]. The shape of transmitted UWB pulses is preserved by Vivaldi antenna because it produces the first derivative of a Gaussian monocycle input with high accuracy without distortion similar to the non-resonating tapered TEM horn [1][24]. The key components of the antenna in term of design are the high-frequency substrate materials, SMA connector, feed structure and the radiating section.

One of the disadvantages of the first design was that the balun must provide good performance over the UWB of the transmitted signal. Thus other

CHAPTER 5 NARROWBEAM ULTRA WIDEBAND ANTENNAS FOR MICROWAVE BREAST CANCER DETECTION

feed structures have been and continue to be explored for this type of antenna. In [1][25], a Vivaldi antenna similar to the one we want to investigate is described.

In this section, we examine and compare three dielectric substrate materials with standard substrate thicknesses. These are the 62 mil thick FR4 substrate, 31 mil thick FR4 substrate, and 40 mil Alumina substrate. Another material investigated was HIK powder where arbitrary dielectric constant and substrate dimensions are possible, but standard manufacturing fabrication techniques do not apply. Experimental prototype antennas manufactured in a lab using HIK powder is possible but the material's mechanical properties have to be investigated so that it would not easily break. Thus this direction was not investigated further and our implementation focuses on using existing standard high-frequency materials and fabrication technology.

Early microstrip antennas were fed by microstrip line or a coaxial probe through the ground plane. The new and prominent feeding techniques include the coaxial feed, microstrip (coplanar) feed, proximity-coupled microstrip feed, aperture-coupled microstrip feed, and coplanar waveguide feed [26].

5.4.1 Coaxial-to-Microstrip Feed Transition

A simple microstrip transmission line designed for a $50\text{-}\Omega$ characteristic impedance can serve as a feed structure to the radiating section of the antenna. Usually, the microstrip transmission line gradually tapers to a middle section such as a paired-strip transmission line [23] or to the radiating section [24]. Given the

CHAPTER 5 NARROWBEAM ULTRA WIDEBAND ANTENNAS FOR MICROWAVE BREAST CANCER DETECTION

thickness and dielectric constant of the substrate we can find the width of the transmission line from [27]

$$W = \frac{8e^A d}{e^{2A} - 2} \text{ for } W < 2d \quad (5.6)$$

where

$$A = \frac{Z_0}{60} \sqrt{\frac{\epsilon_r + 1}{2}} + \frac{\epsilon_r - 1}{\epsilon_r + 1} \left(0.23 + \frac{0.11}{\epsilon_r} \right) \quad (5.7)$$

and Z_0 is the desired characteristic impedance which is 50Ω , ϵ_r is the dielectric constant, and d is the substrate thickness.

The equation in (5.6) assumes an infinite ground plane but this is not the case in reality. So the formula gives us a starting value for doing electromagnetic (EM) optimization. Another method to obtain an initial starting point for EM optimization is to implement a circuit model using CAD tool such as ADS [28].

CHAPTER 5 NARROWBEAM ULTRA WIDEBAND ANTENNAS FOR
MICROWAVE BREAST CANCER DETECTION

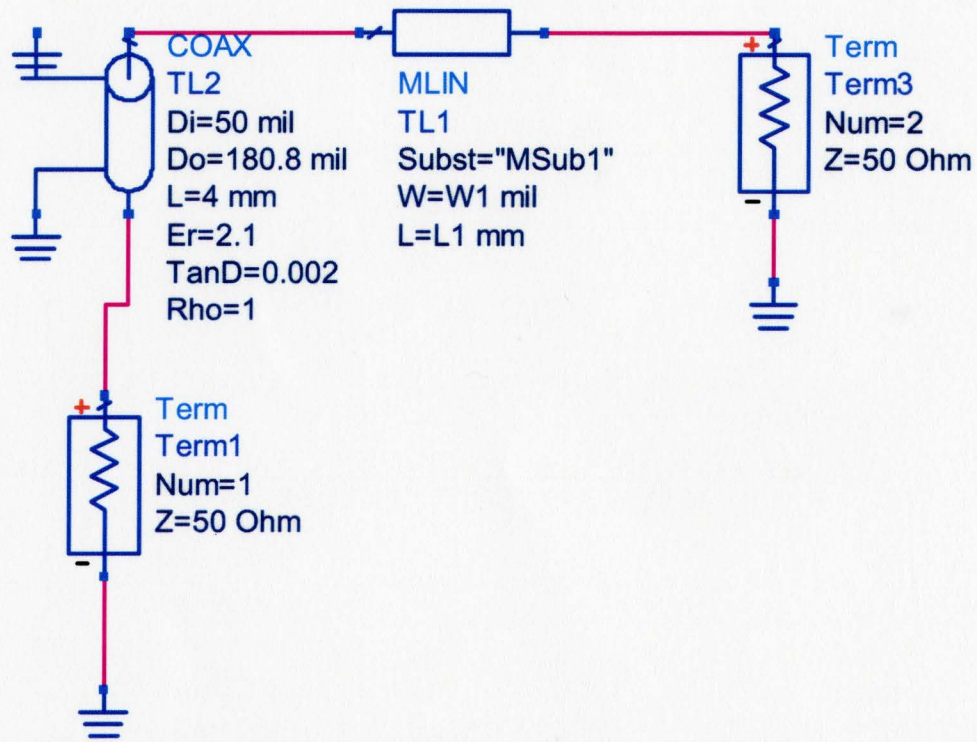


Fig. 5.2 An example of microstrip transmission line design using a circuit model in ADS [28].

Fig. 5.2 illustrates the circuit model used for the optimization of the width of the microstrip as a circuit parameter. Once a width is obtained, we can start the design of the microstrip line from this value in Ansoft HFSS [29].

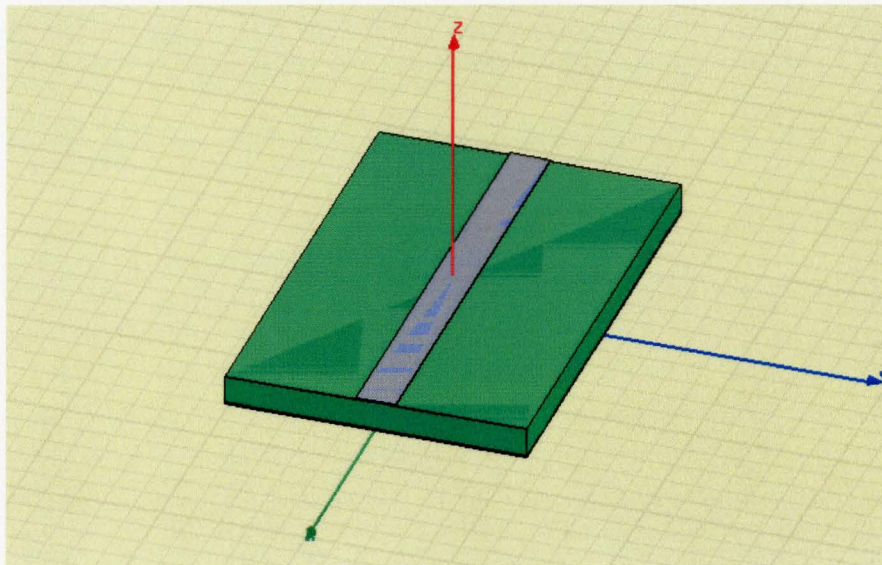


Fig. 5.3. An example of microstrip transmission line design using EM simulator in HFSS [29].

Fig. 5.3 shows the HFSS EM model of the microstrip transmission line. In general, the parameters to optimize are the width of the transmission line, the width of the ground plate, and the substrate height. Table 5.1 summarizes the values obtained for the various substrates under consideration.

The FR4 substrate has dielectric constant of 4.4 and loss tangent of 0.02 while the Alumina substrate has dielectric constant of 9.9 and loss tangent of 0.006. The specification for the design was that the return loss or $|S_{11}|$ must be less than -15 dB over the FCC approved UWB region. The results in Table 5.1 show the EM optimization results for the given standard high-frequency substrate materials and specification.

CHAPTER 5 NARROWBEAM ULTRA WIDEBAND ANTENNAS FOR MICROWAVE BREAST CANCER DETECTION

TABLE 5.1
SUMMARY OF MICROSTRIP DESIGN PARAMETERS

| PCB Substrate | PCB Thickness (mils) | Metal Thickness (mils) | Microstrip Width (mils) | Microstrip Ground Plate Width (mils) |
|----------------|----------------------|------------------------|-------------------------|--------------------------------------|
| <i>FR4</i> | 62 | 4 | 153 | 755 |
| <i>FR4</i> | 31 | 4 | 55 | 397 |
| <i>Alumina</i> | 40 | 4 | 55 | 410 |

Note: The substrate and copper metal thickness are from PCB fabrication standards.

5.4.2 SMA Connector Modeling

The antenna is fed by a 50- Ω coax feed from the bottom connected through a SMA connector and transitions to the feed structure including the microstrip discussed in Section IV.A. A SMA PCB blunt post terminal is found from an SMA catalog [30].

Fig. 5.4 shows the geometry of the SMA connector feeding the antenna. Table 5.2 outlines the SMA geometry parameters. In the designs explored, the SMA connector is fed from the bottom to the microstrip line. Four varying designs for the feed structure transitioning from the SMA connector to the

CHAPTER 5 NARROWBEAM ULTRA WIDEBAND ANTENNAS FOR MICROWAVE BREAST CANCER DETECTION

microstrip line are studied. The same SMA geometry parameters are used in these feed structure designs.

The inclusion of the SMA connector in the EM model improves the simulation result in terms of matching actual measurements. Other back metal of SMA connector is also modeled to improve the EM model of the feed structure to the antenna.

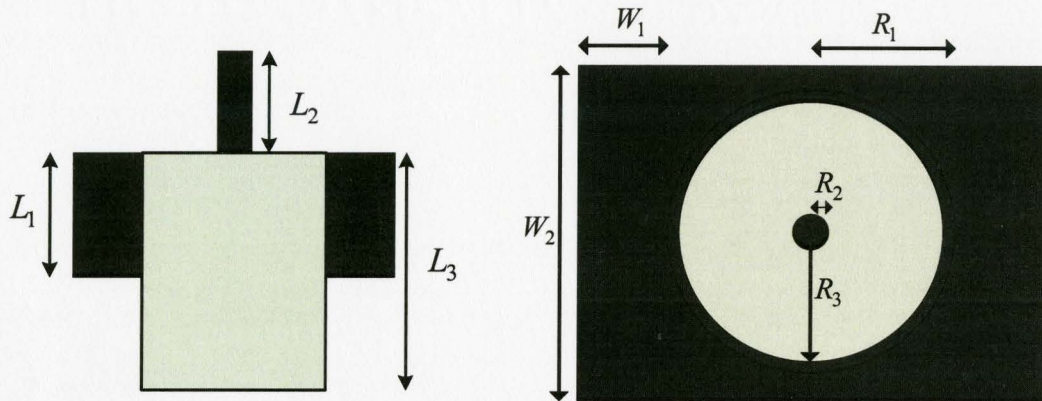


Fig. 5.4 The geometry of the SMA connector feeding the antenna.

CHAPTER 5 NARROWBEAM ULTRA WIDEBAND ANTENNAS FOR MICROWAVE BREAST CANCER DETECTION

TABLE 5.2
SMA GEOMETRY PARAMETERS

| W_1 (mil) | W_2 (mil) | L_1 (mil) | L_2 (mil) | L_3 (mil) | R_1 (mil) | R_2 (mil) | R_3 (mil) |
|----------------|----------------|----------------|----------------|----------------|----------------|----------------|----------------|
| 17 | 250 | 65 | 40 | 157 | 108 | 25 | 90 |

The SMA connector is modelled by a cylindrical band of electric current flowing on the centre copper conductor from the 50- Ω lumped port at the bottom to the top with a TEM field distribution in the ring about the probe. The E-field polarized in the x direction becomes linearly polarized in the z direction as it transits from the SMA connector to the microstrip line.

The dielectric of the cylinder is Teflon with dielectric constant of 2.1, and loss tangent of 0.001. It is simulated in Ansoft HFSS [29] and the return loss is found to be less than -20 dB over the bandwidth from 2 GHz to 11 GHz.

5.4.3 SMA Connector to Microstrip Feed Transition

Although there are several papers on various feeding techniques, which are summarized in [26], we focus on the coaxial feed or probe coupling, and microstrip feeds. In [26], the coaxial probe feeding of a microstrip patch antenna is shown and discussed. The feed structure is vital for efficient transfer of power from the input source to the radiating structure. Here, four possible feed structures are studied.

CHAPTER 5 NARROWBEAM ULTRA WIDEBAND ANTENNAS FOR MICROWAVE BREAST CANCER DETECTION

The setup for the first design involved attaching a SMA connector from the bottom of the PCB substrate. Then the centre conductor of the coax is passed through the substrate and soldered to the microstrip. This is similar to the setup in [26][31], which used a type N coaxial connector. Other than selection of the position of the centre feed point of the SMA connector with respect to the microstrip, no other structure is added to improve impedance matching, radiation pattern and return loss performance.

The advantage of this coaxial feed structure is its simplicity. This is due to the direct relation between input impedance and feed point position. The coaxial feed structure has the following disadvantages [26]:

- Coaxial feeding of an array requires a large number of solder joints making fabrication complicated, but for our application in breast cancer detection only at most a dozen antenna elements are needed in an array.
- For the UWB applications, a thicker substrate is needed to increase the bandwidth but this implies a longer probe. The longer probe increases spurious radiation from the probe and the feed inductance, which is for instance why using HIK powder substrate with 2 mm thick substrate became challenging using the coaxial probe feed.
- In [26], using ring shaped slot in the patch metallization concentric with the probe is suggested to offset the effects of the feed inductance.

CHAPTER 5 NARROWBEAM ULTRAWIDEBAND ANTENNAS FOR MICROWAVE BREAST CANCER DETECTION

This is at the cost of radiation pattern performance due to the electric field in the ring-shaped slot.

The second design involves the introduction of a radial stub along with the coaxial feed from the bottom. The radial stub is supposed to improve the radiation pattern and smoothly re-direct the power from the back of the antenna to the radiating section. Fig. 5.5 shows the feed structure with the radial stub. The distance between where the radial stub starts and the feed point is d_2 . The angle ϕ and radius R determine the dimensions of the radial stub. Vias can also be added to ground the stub to reduce the radiation from the back of the antenna. The radial stub was effective in increasing radiation efficiency of the antenna but at the cost of complication and difficulty in design.

Achieving wideband impedance matching to $50\text{-}\Omega$ using the radial stub proved very difficult because of the input reactance which increases for high frequencies and equivalent characteristic impedance being between $10 \sim 20 \text{ }\Omega$. In addition, during the EM simulation, higher-order modes were excited by the radial stub. Fig. 5.6 shows the E-field distribution in the radial stub and the microstrip line.

CHAPTER 5 NARROWBEAM ULTRA WIDEBAND ANTENNAS FOR MICROWAVE BREAST CANCER DETECTION

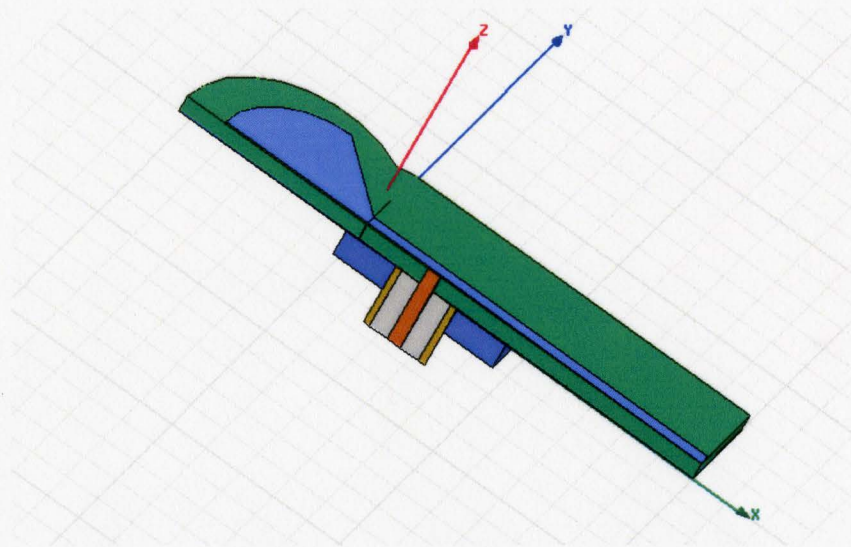


Fig. 5.5 The half-structure of the feed with the SMA connector, microstrip line and radial stub as simulated in HFSS.

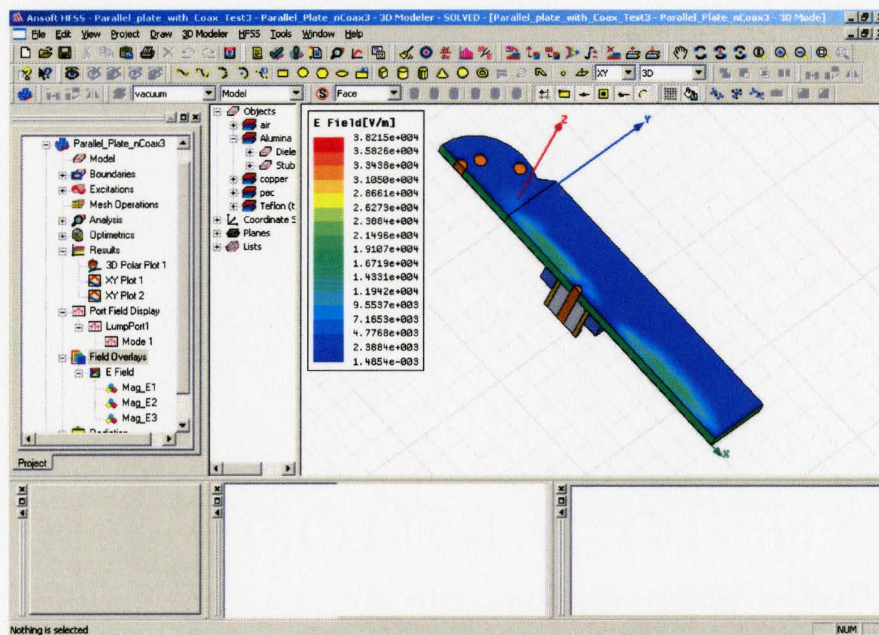


Fig. 5.6 The E-field distribution in the radial stub and the microstrip line as simulated in HFSS.

CHAPTER 5 NARROWBEAM ULTRA WIDEBAND ANTENNAS FOR MICROWAVE BREAST CANCER DETECTION

The third design involves reducing the radiation loss compared to the first design and improving the impedance match compared to the second design. The antenna impedance can be transformed by EM coupling between the microstrip and the coaxial probe. So the aim is to increase radiation efficiency and direct the radiation power in a narrowbeam towards the breast medium and at the same time design an antenna that has return loss less than -10 dB over the bandwidth from 3.1 GHz to 10.6 GHz. To accomplish this, EM energy from the SMA connector is coupled to the microstrip line by extending half of the cylindrically shaped SMA connector, including the shield and substrate, to be the same as the centre conductor (See Fig. 5.7). The coax probe feed point was placed a very small distance from the back end of the antenna. The distance between the feed point and the end of the microstrip line was set at 5 mil.

The proposed third design is implemented for all the substrates outlined in Table 5.1. The geometry of the proposed feed structure is shown in Fig. 5.7. The dimensions are the same as in Table 5.1.

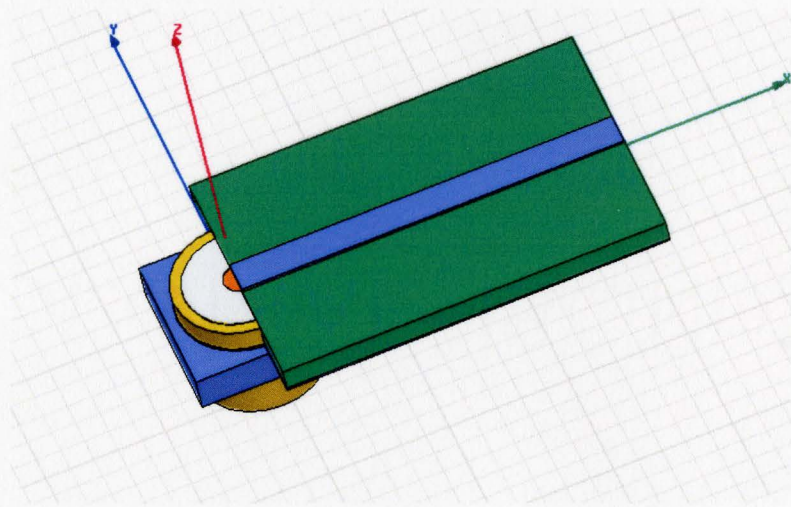


Fig. 5.7 The proposed feed structure with the SMA connector, EM coupling structure, and microstrip line implemented on alumina substrate and simulated in HFSS.

The corresponding return loss is shown in Fig. 5.8, while the voltage standing wave ratio (VSWR) in Fig. 5.9. The return loss is less than -12 dB over the bandwidth from 2 GHz to 11 GHz. The response $|S_{12}|$ and $|S_{11}|^2 + |S_{12}|^2$ are plotted in Fig. 5.10(a) and 5.10(b), respectively. The later measure is related to the radiated power by the feed structure, which is a way to determine the radiation efficiency of the structure when connected to the radiating component of antenna.

One can see from the plots that there is still some power radiated through the back to the air medium. This radiated power is about 10% of the power transmitted through the coaxial feed.

CHAPTER 5 NARROWBEAM ULTRA WIDEBAND ANTENNAS FOR
MICROWAVE BREAST CANCER DETECTION

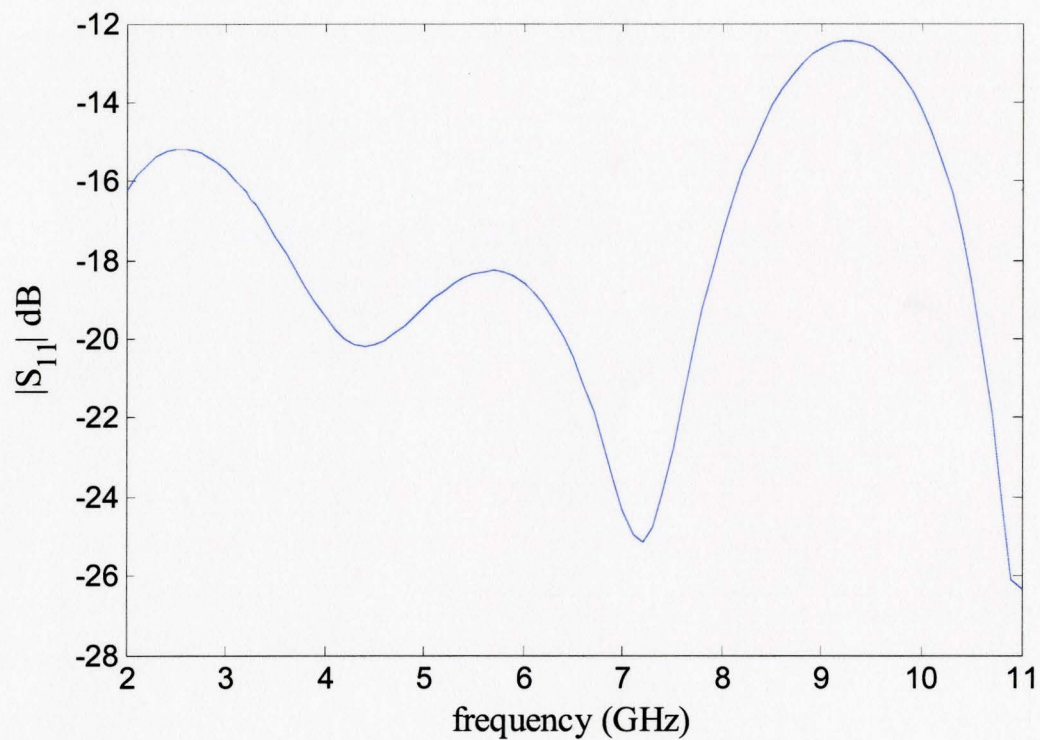


Fig. 5.8 The return loss $|S_{11}|$ dB response corresponding to the proposed feed structure in Fig. 5.7 as simulated in HFSS.

CHAPTER 5 NARROWBEAM ULTRAWIDEBAND ANTENNAS FOR MICROWAVE BREAST CANCER DETECTION

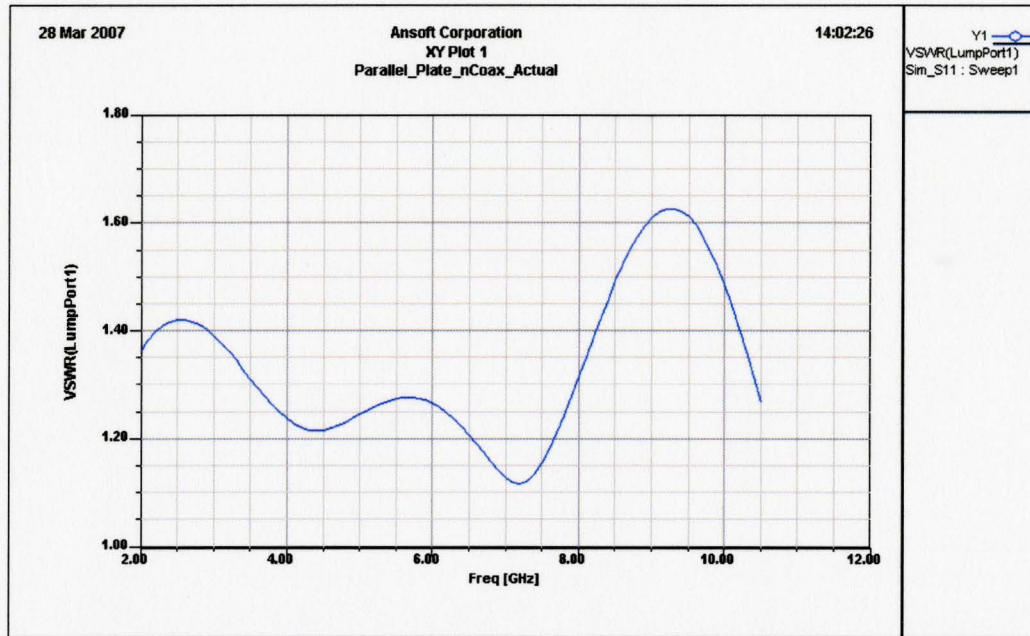


Fig. 5.9 The VSWR response corresponding to the proposed feed structure in Fig. 5.7 as simulated in HFSS.

CHAPTER 5 NARROWBEAM ULTRA WIDEBAND ANTENNAS FOR
MICROWAVE BREAST CANCER DETECTION

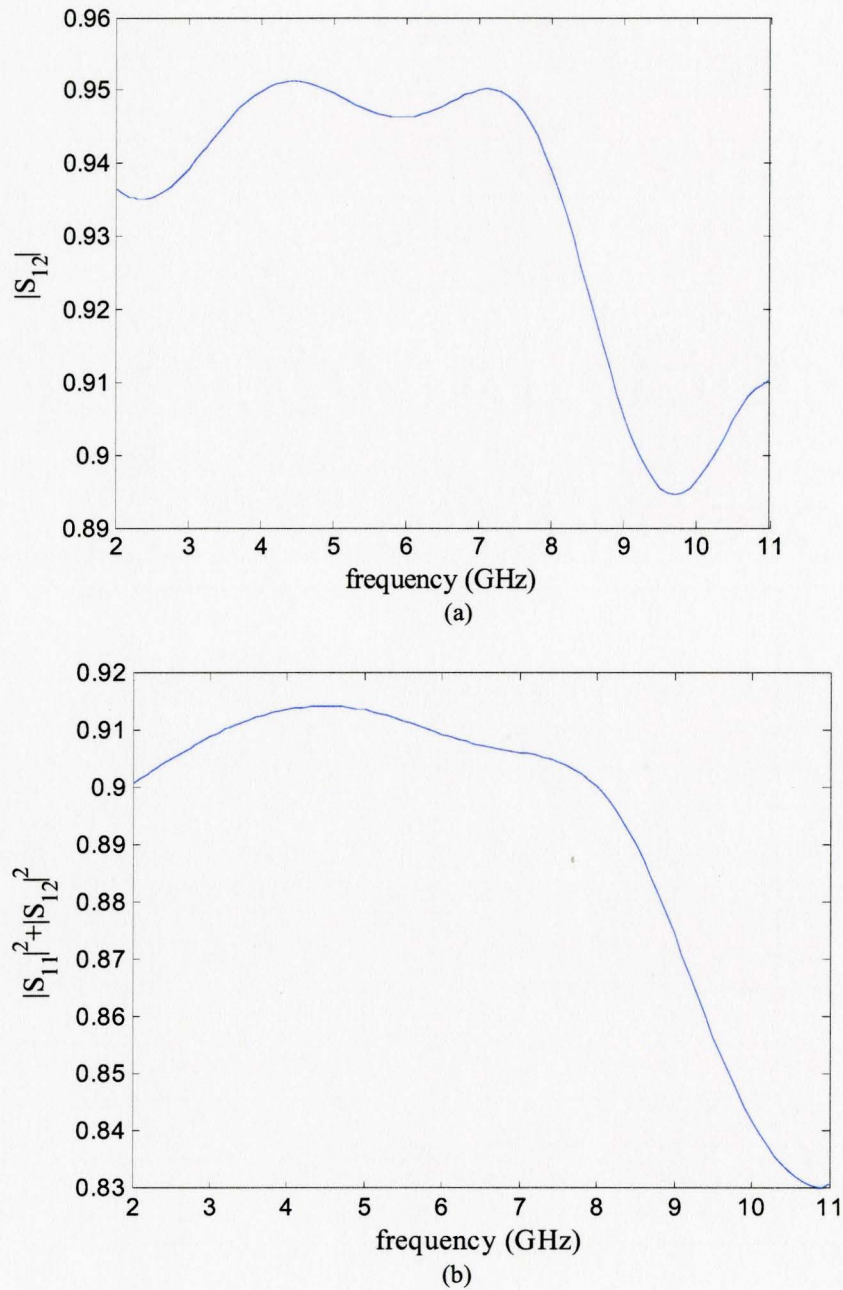


Fig. 5.10 Responses: (a) $|S_{12}|$ and (b) $|S_{11}|^2 + |S_{12}|^2$, corresponding to the proposed feed structure in Fig. 5.7 as simulated in HFSS.

CHAPTER 5 NARROWBEAM ULTRA WIDEBAND ANTENNAS FOR MICROWAVE BREAST CANCER DETECTION

In order to improve the return loss response, an additional dielectric layer is added to the third proposed design. So in this fourth design the microstrip is between two dielectric substrates of the same material. The use of double-layer dielectric substrate can be employed for PCB antenna fabrication since manufacturing companies give customers this option in design.

Fig. 5.11 shows the proposed feed structure with two dielectric layers. The corresponding return loss is seen in Fig. 5.12, while the VSWR in Fig. 5.13. The return loss is less than -12 dB over the bandwidth from 2 GHz to 11 GHz. The response $|S_{12}|$ and $|S_{11}|^2 + |S_{12}|^2$ are plotted in Fig. 5.14(a) and 5.14(b), respectively. The near-field radiation pattern is shown in Fig. 5.15. The near-field distribution does not show radiation behind the feed structure partly because there was an absorber placed in the back of antenna. Fig. 5.16 shows the E-field distribution in the substrate and half-ring shaped Teflon dielectric extension added to proposed feed structure.

The return loss achieved for this proposed feed structure is less than -15 dB from 3.1 GHz to 10.6 GHz.

CHAPTER 5 NARROWBEAM ULTRA WIDEBAND ANTENNAS FOR
MICROWAVE BREAST CANCER DETECTION

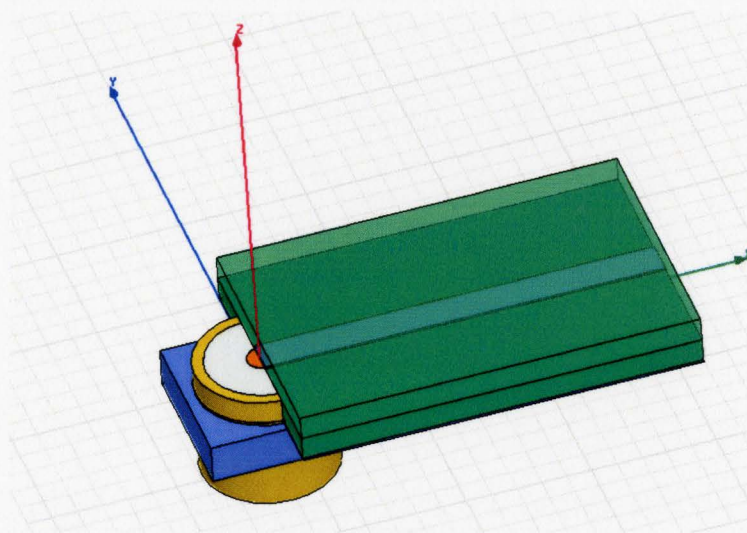


Fig. 5.11 The proposed feed structure with double-layer dielectric, the SMA connector, EM coupling structure, and microstrip line implemented on alumina substrate and simulated in HFSS.

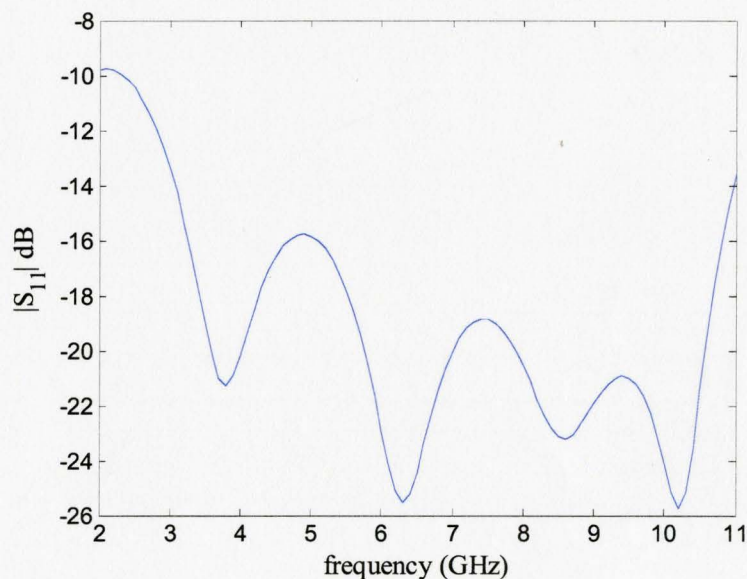


Fig. 5.12 The return loss $|S_{11}|$ dB response corresponding to the proposed feed structure in Fig. 5.11 as simulated in HFSS.

CHAPTER 5 NARROWBEAM ULTRA WIDEBAND ANTENNAS FOR MICROWAVE BREAST CANCER DETECTION

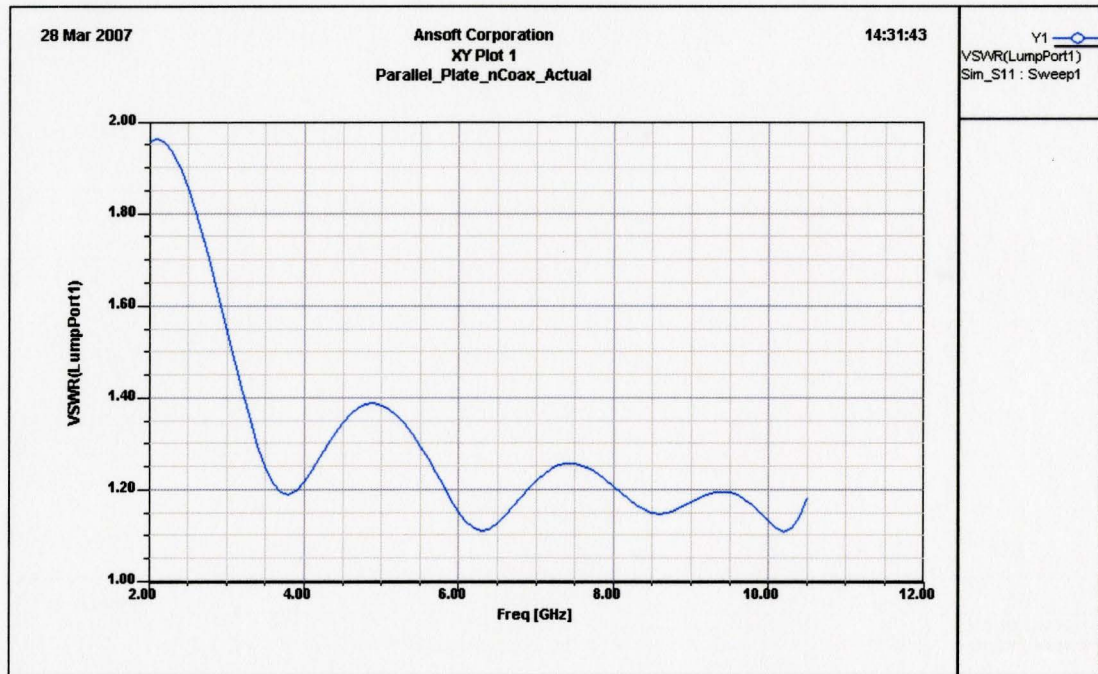


Fig. 5.13. The VSWR response corresponding to the proposed feed structure in Fig. 5.11 as simulated in HFSS.

CHAPTER 5 NARROWBEAM ULTRA WIDEBAND ANTENNAS FOR
MICROWAVE BREAST CANCER DETECTION

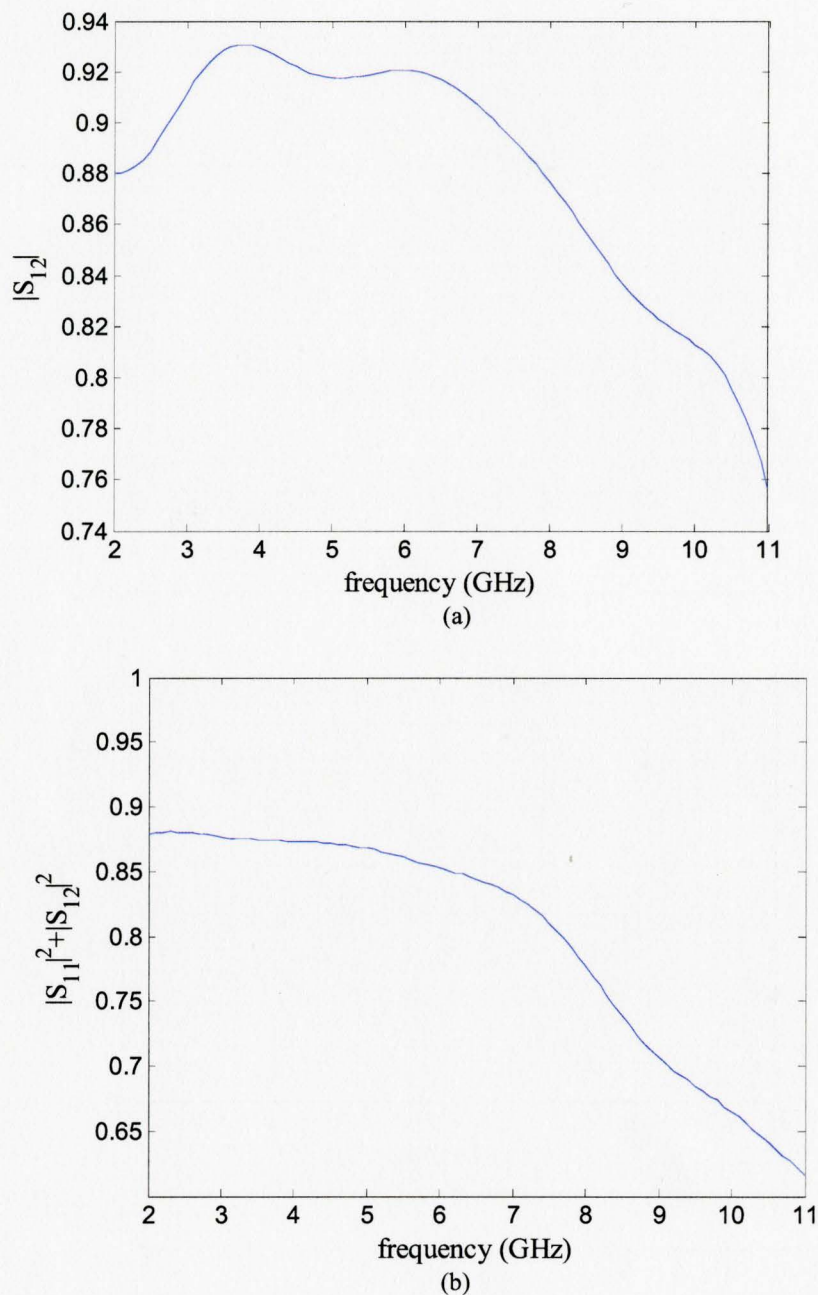
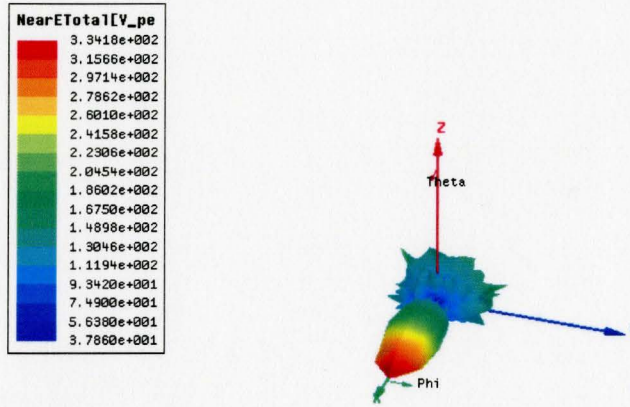
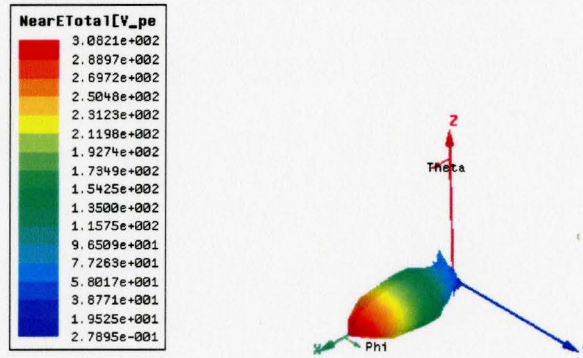


Fig. 5.14 Responses: (a) $|S_{12}|$ and (b) $|S_{11}|^2 + |S_{12}|^2$, corresponding to the proposed feed structure in Fig. 5.11 as simulated in HFSS.

CHAPTER 5 NARROWBEAM ULTRA-WIDEBAND ANTENNAS FOR MICROWAVE BREAST CANCER DETECTION



(a)



(b)

Fig. 5.15 The near-field radiation pattern: (a) without absorber in the back and (b) with absorber corresponding to the proposed feed structure in Fig. 5.11 as simulated in HFSS.

CHAPTER 5 NARROWBEAM ULTRAWIDEBAND ANTENNAS FOR MICROWAVE BREAST CANCER DETECTION

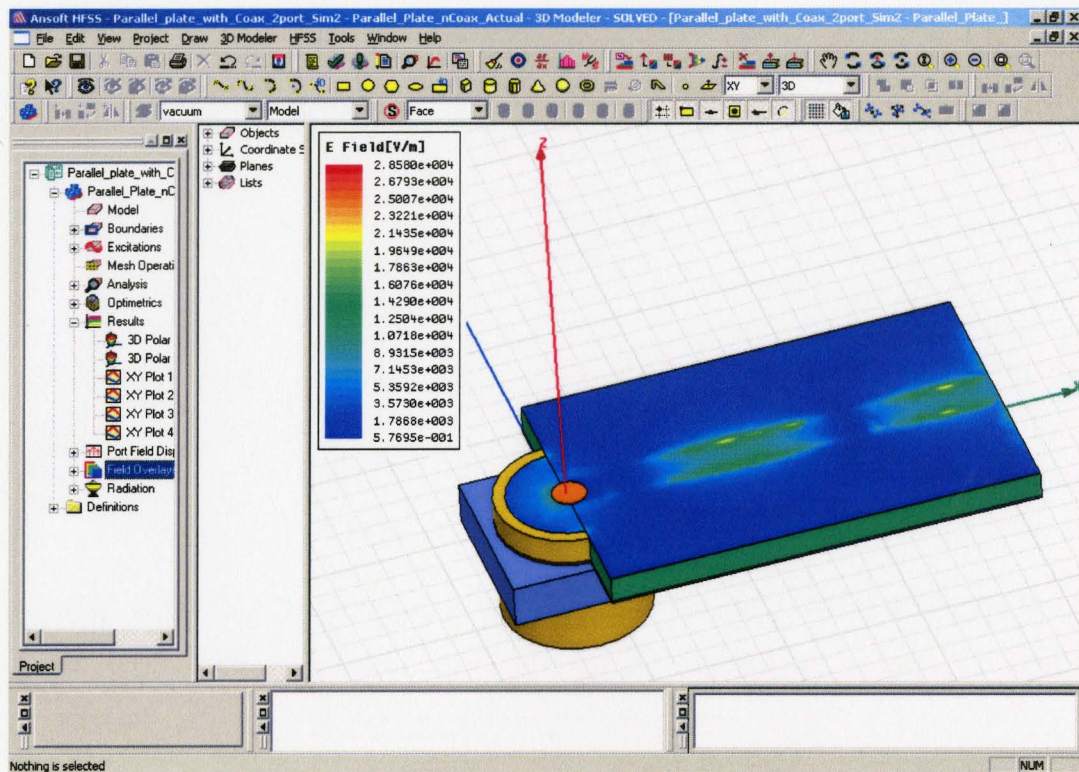


Fig. 5.16 The E-field distribution at 6 GHz in the substrate and Teflon extension added for the proposed feed structure in Fig. 5.11 as simulated in HFSS.

This feed structure is difficult to fabricate as it needs special manufacturing of the semi-cylindrical metal that has the same thickness as the SMA connector and is perhaps not feasible.

The feed structures proposed were also implemented on the 0.062" FR4 and 0.031" FR4 substrates. The return loss and VSWR is much improved using the FR4 substrate with thickness of 62 mil. The return loss and VSWR in the bandwidth from 2 GHz to 11 GHz were made worst as the thickness was decreased from 62 mil to 31 mil as expected in the UWB region.

CHAPTER 5 NARROWBEAM ULTRA WIDEBAND ANTENNAS FOR MICROWAVE BREAST CANCER DETECTION

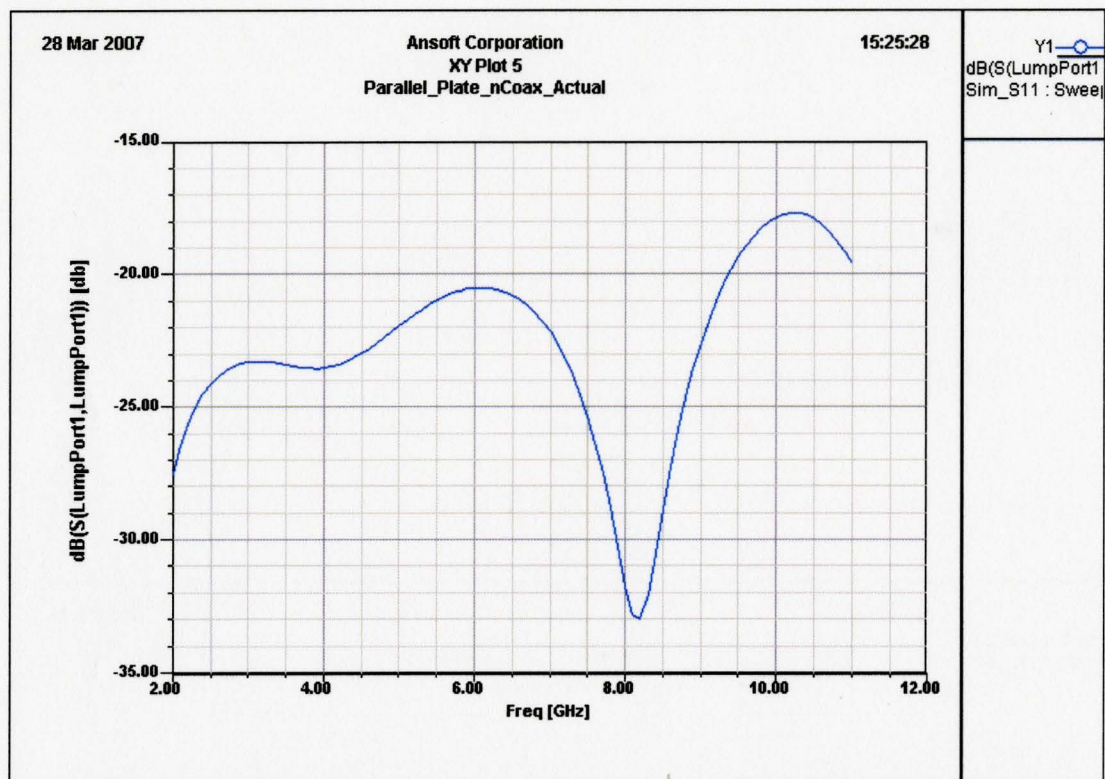


Fig. 5.17 The return loss $|S_{11}|$ dB response corresponding to the proposed feed structure with the SMA connector, EM coupling structure, and microstrip implemented on FR4 substrate with thickness of 62 mil as simulated in HFSS.

CHAPTER 5 NARROWBEAM ULTRA WIDEBAND ANTENNAS FOR MICROWAVE BREAST CANCER DETECTION



Fig. 5.18 The VSWR response corresponding to the proposed feed structure with the SMA connector, EM coupling structure, and microstrip implemented on FR4 substrate with thickness of 62 mil as simulated in HFSS.

CHAPTER 5 NARROWBEAM ULTRA WIDEBAND ANTENNAS FOR MICROWAVE BREAST CANCER DETECTION

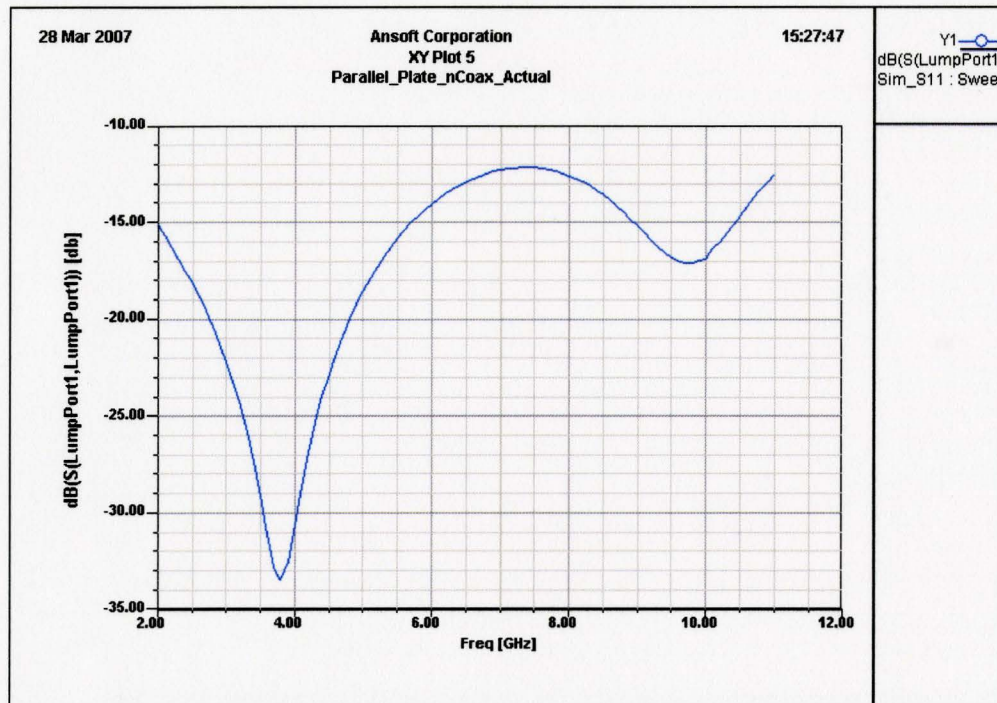


Fig. 5.19 The return loss $|S_{11}|$ dB response corresponding to the proposed feed structure with the SMA connector, EM coupling structure, and microstrip implemented on FR4 substrate with thickness of 31 mil as simulated in HFSS.

CHAPTER 5 NARROWBEAM ULTRA WIDEBAND ANTENNAS FOR MICROWAVE BREAST CANCER DETECTION

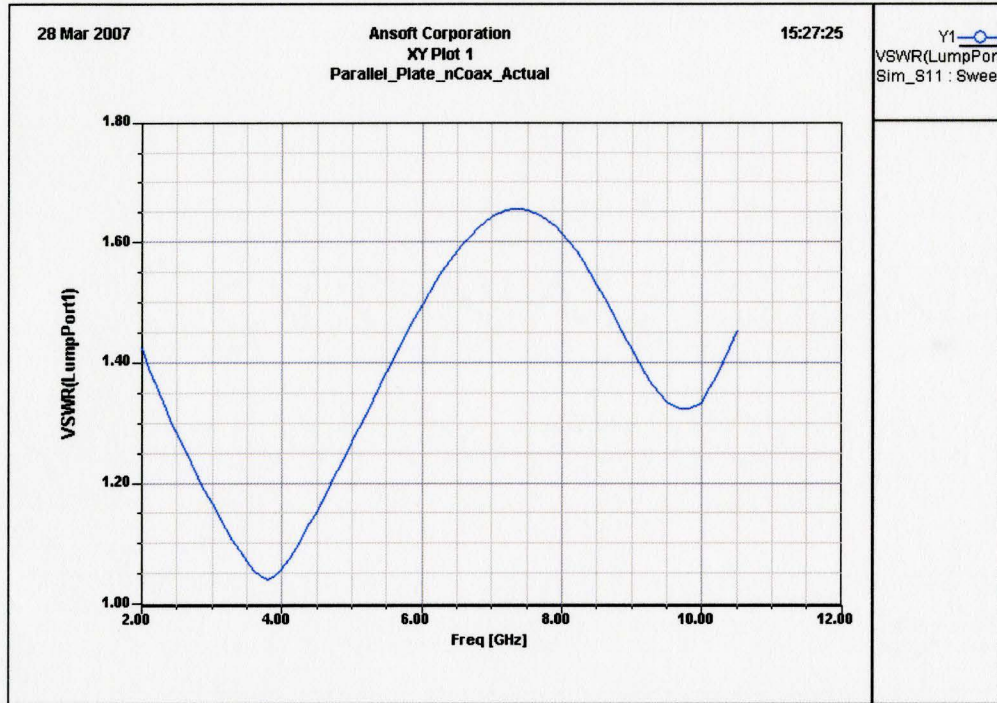


Fig. 5.20 The VSWR response corresponding to the proposed feed structure with the SMA connector, EM coupling structure, and microstrip implemented on FR4 substrate with thickness of 31 mil as simulated in HFSS.

Table 5.3 compares the various feed structures explored as components of UWB antennas. In addition to those proposed in this report, the comparison includes feed structures used in the literature such as the coplanar waveguide (CPW). The proposed structures outperform the other feed structures in terms of bandwidth, and impedance matching but at the expense of spurious feed radiation and complexity of fabrication. The alumina substrate performs better than FR4 at higher frequencies but its advantages are offset partly by the substrate thickness as the highest standard thickness is 40 mil. Custom design for the substrate is

CHAPTER 5 NARROWBEAM ULTRA WIDEBAND ANTENNAS FOR MICROWAVE BREAST CANCER DETECTION

costly which is to be avoided since we want to design low-cost planar microstrip antennas.

Let us first examine the computational domain and the model for the breast tissue without any tumors. The dielectric properties of breast adipose tissue is obtained from their measured complex permittivity $\tilde{\epsilon}$, which is

$$\tilde{\epsilon} = \epsilon' - j\epsilon'' \quad (5.8)$$

where $\epsilon' = \epsilon_0 \epsilon_r$ is the permittivity of the tissue; $\epsilon'' = \epsilon_0 \sigma / \omega$ is the out-of-phase dielectric loss factor, and σ is the total conductivity including contributions from frequency-independent ionic conductivity [32]. Gabriel *et al.* [32] reported permittivity measurements in the frequency range 10 Hz to 20 GHz for human skin and breast adipose tissue. In our experimental antenna design setup, we assume the adipose tissue and human skin layers to be homogeneous with certain average relative permittivity and conductivity in the prescribed computational domain. The experimental setup for simulating the antenna element is shown in Fig. 5.21. The antenna is to be designed to match the breast tissue and reduce skin-artifact reflections. The dispersive properties of normal breast tissue are included in the HFSS model using the averaged linear single-pole Debye model with values as in Bond *et al.* [33] valid from 100 MHz to 20 GHz.

CHAPTER 5 NARROWBEAM ULTRAWIDEBAND ANTENNAS FOR MICROWAVE BREAST CANCER DETECTION

The single Debye model is given by

$$\varepsilon_r(\omega) - j \frac{\sigma(\omega)}{\omega \varepsilon_0} = \varepsilon_\infty + \frac{\varepsilon_s - \varepsilon_\infty}{1 + j\omega\tau} - j \frac{\sigma_s}{\omega \varepsilon_0} \quad (5.9)$$

where ε_s is the low-frequency permittivity, ε_∞ is the high-frequency permittivity, τ is the relaxation time, $\omega = 2\pi f$ is the radian frequency, ε_0 is the permittivity of free-space and σ_s is the ionic conductivity. The Debye parameter values are given in Table 5.4.

The numerical domain employs symmetry with half the structure with dimensions of (61.9 x 43.6 x 54) mm³ box of the phantom followed by 2 mm thick (2 x 43.6 x 54) mm³ skin and (55 x 43.6 x 54) mm³ box of air. The antenna return loss $|S_{11}|$ dB is measured along with the antenna near-field pattern and directivity.

CHAPTER 5 NARROWBEAM ULTRAWIDEBAND ANTENNAS FOR
MICROWAVE BREAST CANCER DETECTION

TABLE 5.3
SUMMARY OF COMPARISON OF VARIOUS TYPES OF FEED STRUCTURE FOR UWB ANTENNAS

| Characteristics | Coaxial-Probe Feed | Coaxial-Probe Feed with Radial Stub | CPW Feed | Proposed Structure #1 (Fig. 6) | Proposed Structure #2 (Fig. 10) |
|---|-------------------------------|-------------------------------------|--------------------|---|---|
| Configuration | Non-planar | Non-planar | Coplanar | Non-planar | Non-planar |
| <i>Ease of Fabrication</i> | Soldering and drilling needed | Soldering and drilling needed | Alignment required | Soldering and drilling needed and special manufacturing for the SMA extension metal | Soldering and drilling needed and special manufacturing for the SMA extension metal |
| <i>Maximum Return Loss (3.1GHz to 10.6 GHz)</i> | -10 dB | 0 dB | -15 dB | -13 dB | -17 dB |
| <i>Spurious feed radiation</i> | More | Less | Less | Medium | More |
| <i>Polarization purity</i> | Poor | Good | Good | Excellent | Excellent |
| <i>Impedance Matching</i> | Easy | Poor | Easy | Easy | Easy |
| <i>Reliability</i> | Poor due to soldering | Good | Good | Better | Better |

CHAPTER 5 NARROWBEAM ULTRA WIDEBAND ANTENNAS FOR
MICROWAVE BREAST CANCER DETECTION

TABLE 5.4
AVERAGED DEBYE MODEL PARAMETERS

| Tissue | ϵ_{∞} | ϵ_s | τ ps | $\frac{\sigma}{S/m}$ |
|------------|---------------------|--------------|--------------|----------------------|
| Skin | 4 | 48 | 8 | 0.5 |
| Breast fat | 7 | 10 | 7 | 0.15 |
| Tumor | 4 | 54 | 7 | 0.7 |

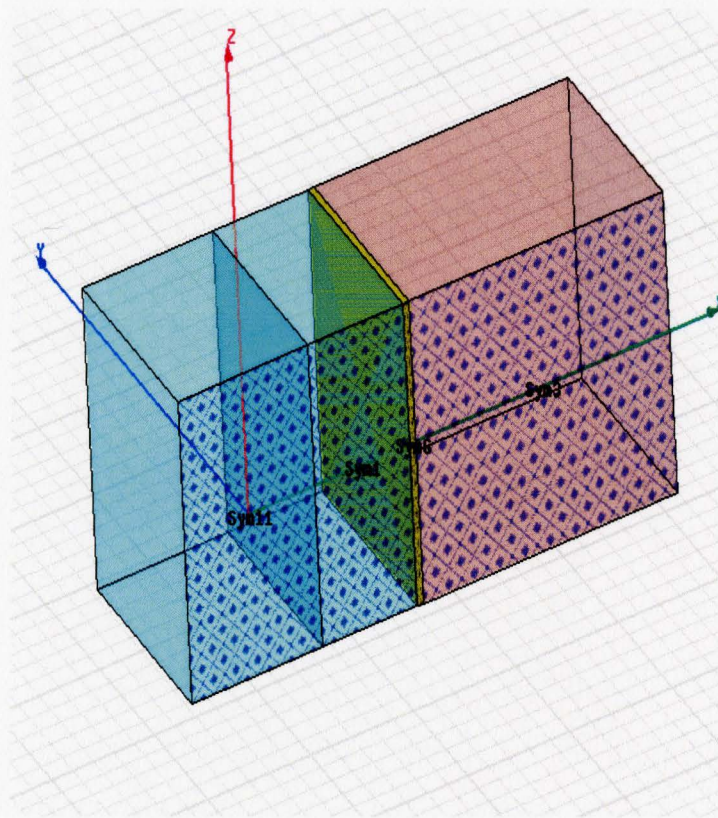


Fig. 5.21 The planar numerical model of the breast medium with the skin layer between the air-breast interface as simulated in HFSS.

CHAPTER 5 NARROWBEAM ULTRA WIDEBAND ANTENNAS FOR MICROWAVE BREAST CANCER DETECTION

TABLE 5.5
ANTENNA GEOMETRY DESIGN PARAMETERS

| Dimension | Value |
|---------------------|---------|
| Width | 63.5 mm |
| Length | 46 mm |
| Metal shield height | 16 mm |

Various narrowbeam microstrip planar TEM horn antenna designs were tried. The proposed antenna design is shown in Fig. 5.22.

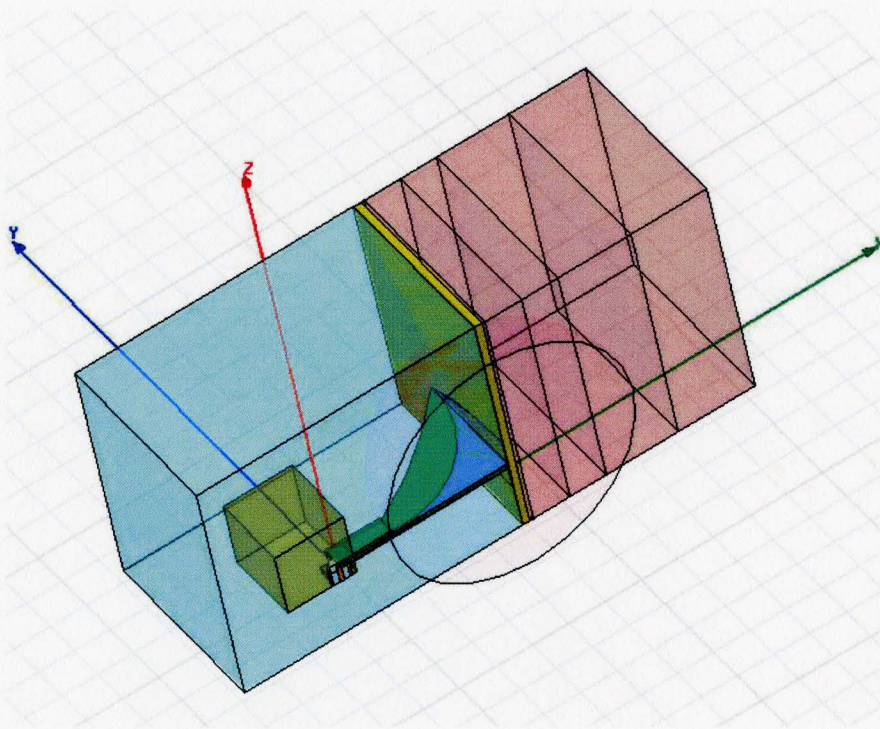


Fig. 5.22 Proposed antenna design #1 with feed structure on alumina substrate and the radiating substrate with dielectric constant of 12.24 and height of 40 mil as simulated in HFSS.

CHAPTER 5 NARROWBEAM ULTRA WIDEBAND ANTENNAS FOR MICROWAVE BREAST CANCER DETECTION

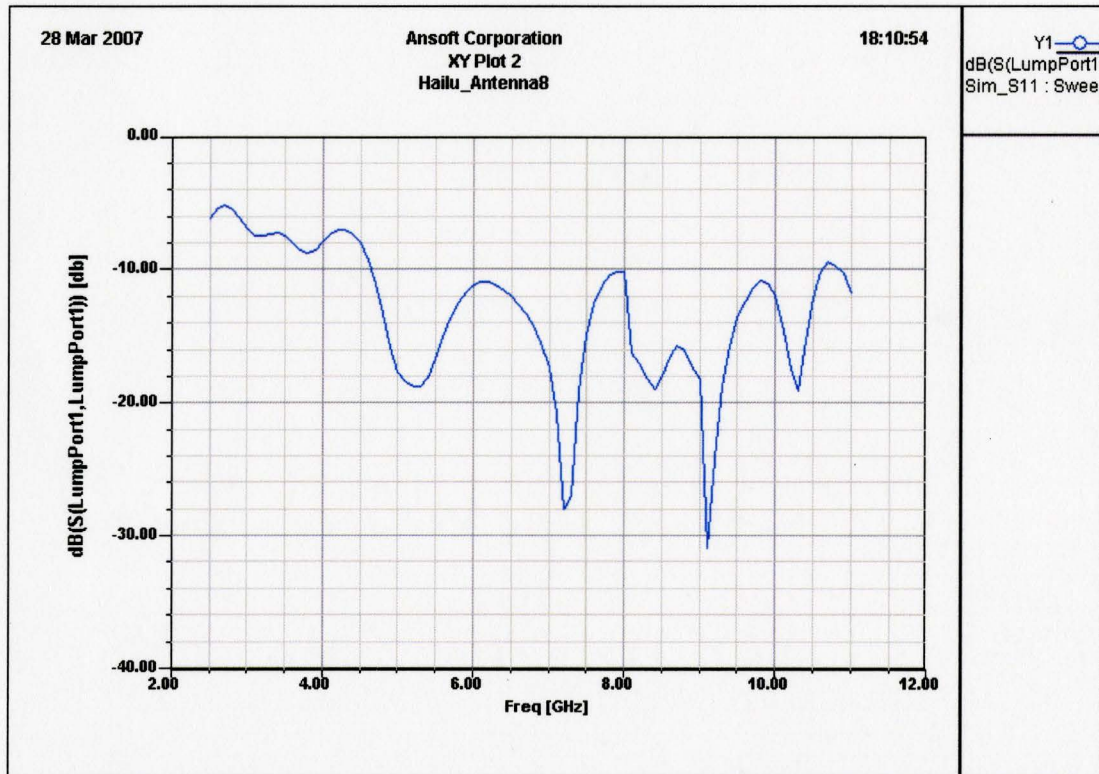


Fig. 5.23 The return loss response for proposed antenna design #1 as simulated in HFSS.

The corresponding responses for the antenna in Fig. 5.22 are return loss, VSWR, and near-field radiation pattern. They are shown in Fig. 5.23 to Fig. 5.25. Table 5.5 shows the antenna parameters for the design shown in Fig. 5.22. It is important to note that the challenges of designing the TEM horn antenna flared in the H-plane on a PCB for applications for breast cancer detection applications arise from the skin-breast artifact reflections and the fact that the antenna has to

CHAPTER 5 NARROWBEAM ULTRAWIDEBAND ANTENNAS FOR MICROWAVE BREAST CANCER DETECTION

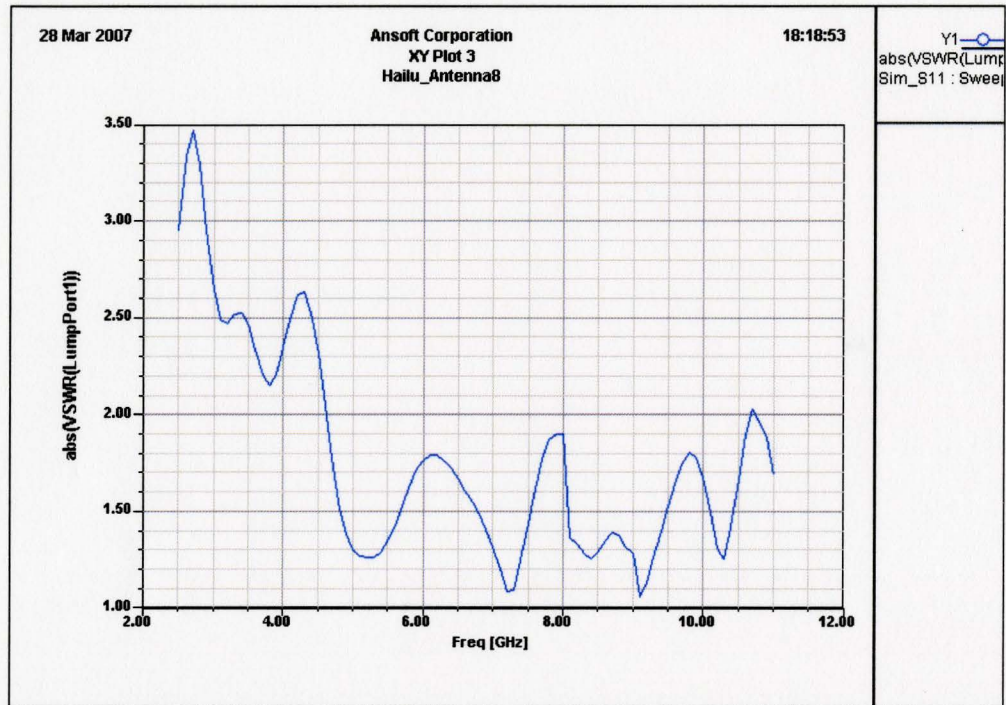


Fig. 5.24 The VSWR response for proposed antenna design #1 as simulated in HFSS [29].

be impedance matched to the breast fat tissue for maximum power transfer to the breast.

Other Vivaldi-type slot designs and the dual of the Vivaldi-type antennas based on microstrip design have been considered for UWB communications. It was shown that these types of antennas operate below 15 GHz. Advantages of these antennas are their light weight and thickness.

CHAPTER 5 NARROWBEAM ULTRAWIDEBAND ANTENNAS FOR MICROWAVE BREAST CANCER DETECTION

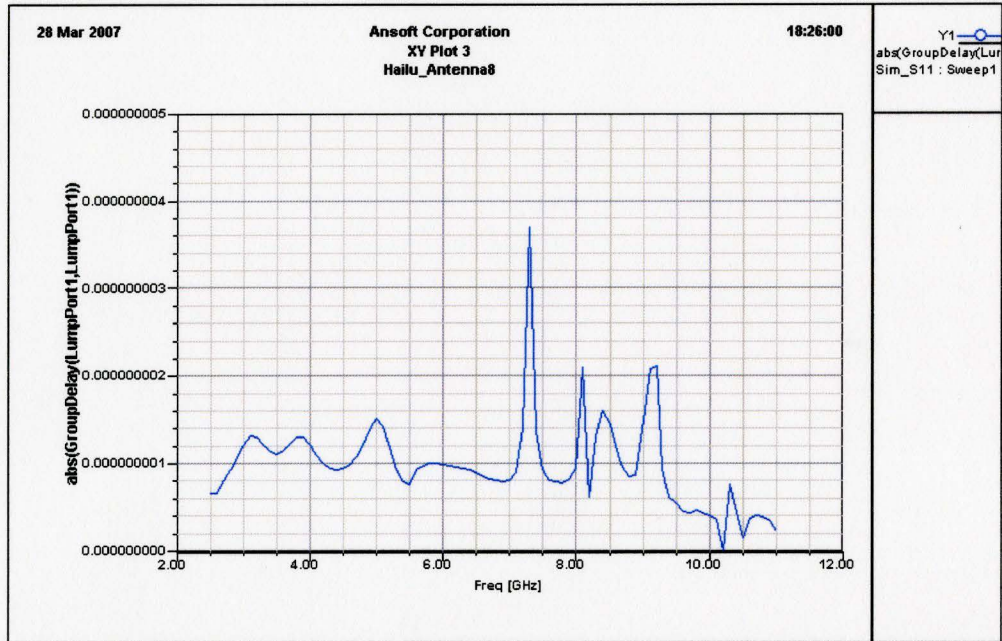


Fig. 5.25 The group delay response for proposed antenna design #1 as simulated in HFSS [29].

For UWB communications, the transient response has relatively sharp peak and has less gain than the horn antenna due to its smaller aperture [34]. The antenna's transient response analysis was conducted and it was found that the feeding network and the Vivaldi's antenna's aperture are a source for reflections [34]. It also has low pulse distortion.

Other challenges and disadvantages of designing planar microstrip antennas include the fact these antennas can induce surface waves. Thus cutting the dielectric substrate in a certain shape may be a strategy to avoid these effects. This design consideration was taken into account in the proposed antenna structures.

5.5 CONCLUDING REMARKS

The first step towards a completely novel antenna for UWB biomedical imaging applications has been demonstrated through the design and simulation of various feed structures and a TEM horn antenna flared in the H-plane on a PCB substrate. An antenna with stable narrowbeam radiation patterns would result in employing fewer array elements. The advantage and disadvantages of the proposed UWB antenna and other UWB antennas available in the literature and were discussed.

In the selection of the substrate, there is a trade-off between alumina and FR4 in cost, performance at high frequencies, and standard thicknesses since the thicker the substrate the better the UWB bandwidth impedance matching. The advantage of using the alumina substrate is that it performs better at higher frequencies in terms of dispersion and return loss, but the largest standard thickness without customization is 40 mil. This limits the UWB impedance matching performance. On the other hand, FR4 substrate can perform adequately, but provided the same thickness, underperforms alumina at higher frequencies. The advantage of FR4 substrate is that it is a cheap standard for PCB fabrication of circuits world-wide; in addition, it comes at a higher thickness at 62 mil than alumina, which improves the UWB impedance matching performance.

Future work would consider the fact that the dielectric properties of the breast vary from patient to patient due to size, age, patient's health and genetics.

CHAPTER 5 NARROWBEAM ULTRAWIDEBAND ANTENNAS FOR MICROWAVE BREAST CANCER DETECTION

These properties have statistical behavior, which requires a statistical model to be used in the design of the antenna to remove the skin-breast artifact.

REFERENCES

- [1] D. Ghosh, A. De, M. C. Taylor, T. K. Sarkar, M. C. Wicks and E. L. Mokole, "Transmission and reception by ultra-wideband (UWB) antennas," *IEEE Antennas and Propagat. Mag.*, vol. 48, no. 5, pp. 67-99, October 2006.
- [2] R. J. Fontana. A Brief History of UWB Communications. Multispectrum Solutions, Inc.
- [3] T. W. Barret. History of Ultra Wideband (UWB) Radar and Communications: Pioneers and Innovators.
- [4] D. M. Hailu, "Narrowbeam ultrawideband antennas for microwave breast cancer detection," Computational Electromagnetic Lab Technical Report, CEM-R-42, March 2007.
- [5] T. T. Wu and R. W. P. King, "The cylindrical antenna with non-reflecting resistive loading," *IEEE Trans. Antennas and Propagat.*, vol. 13, no. 3, pp. 369-373, 1965.
- [6] J. M. Sill and E. C. Fear, "Tissue sensing adaptive radar for breast cancer detection—experimental investigation of simple tumor models," *IEEE Trans. Microwave Theory Tech.*, vol. 53, pp. 3312-3319, Nov. 2005.
- [7] S. C. Hagness, A. Taflove, and J. E. Bridges, "Three-dimensional FDTD analysis of a pulsed microwave confocal system for breast cancer detection: design of an antenna-array element," *IEEE Trans. Antennas and Propagat.*, vol. 47, pp. 783–791, May 1999.
- [8] X. Yun, E. C. Fear and R. H. Johnston, "Compact antenna for radar-based breast cancer detection," *IEEE Trans. Antennas and Propagat.*, vol. 53, pp. 2374-2380, 2005.

CHAPTER 5 NARROWBEAM ULTRAWIDEBAND ANTENNAS FOR MICROWAVE BREAST CANCER DETECTION

- [9] X. Li, S. C. Hagness, M. K. Choi and D. W. van der Weide, "Numerical and experimental investigation of an ultrawideband ridged pyramidal horn antenna with curved launching plane for pulse radiation," *IEEE Trans. Antennas and Wireless Propagat. Lett.*, vol. 2, pp. 259-262, 2003.
- [10] X. Li, E. J. Bond, B. D. Van Veen and S. C. Hagness, "An overview of ultra-wideband microwave imaging via space-time beamforming for early-stage breast-cancer detection," *IEEE Trans. Antennas Propagat.*, vol. 47, pp. 19-34, Feb. 2005.
- [11] H. Kanj and M. Popović, "Miniaturized microstrip-fed "Dark Eyes" antenna for near-field microwave sensing," *IEEE Antennas and Wireless Propagat. Lett.*, pp. 1-4, 2005.
- [12] N. Tavasolian, H. Kanj and M. Popović, "The effect of breast glands on microwave tumor sensing with 'dark eyes' antenna," in *2006 IEEE Antennas and Propagat. Symp.*, pp. 291-294, 2006.
- [13] H. M. Jafari, M. J. Deen, S. Hranilovic and N. K. Nikolova, "Slot antenna for ultra-wideband applications," in *2006 IEEE Antennas and Prop. Symp.*, pp. 1107-1110, 2006.
- [14] J. R. Andrews, "UWB signal sources, antennas and propagation," *IEEE Tropical Conference on Wireless Communication Technology*, Hawaii, pp. 439-440, October 2003.
- [15] K. L. Walton and V. C. Sundberg, "Broadband ridged horn design," *Microwave J.*, vol. 4, no. 2, pp. 96-101, Apr. 1964.
- [16] B. M. Notaros, C. D. McCarrick and D. P. Kasilingam, "Two numerical techniques for analysis of pyramidal horn antennas with continuous metallic ridges," in *IEEE AP-S Int. Symp.*, vol. 2, pp. 560-563, 2001.
- [17] E. T. Rosenbury, G. K. Burke, S. D. Nelson, R. D. Stever, G. K. Gerverno and D. J. Mullenhoff, "Low cost impulse compatible wideband antenna," *U.S. Patent 6 348 898*.
- [18] X. Li, S. K. Davis, S. C. Hagness, D. W. Weide and B. D. Van Veen, "Microwave imaging via space-time beamforming: experimental investigation of tumor detection in multilayer breast phantoms," *IEEE Trans. Microwave Theory Tech.*, vol. 52, pp. 1856-1865, Aug. 2004.

CHAPTER 5 NARROWBEAM ULTRA WIDEBAND ANTENNAS FOR
MICROWAVE BREAST CANCER DETECTION

- [19] M. Picket-May, A. Taflová and J. Baron, "FD-TD modeling of digital signal propagation in 3-D circuits with passive and active loads," *IEEE Trans. Microwave Theory Tech.*, vol. 42, pp. 1514–1523, Aug. 1994.
- [20] J. P. Berenger, "A perfectly matched layer for the absorption of electromagnetic waves," *J. Comput. Phys.*, vol. 114, pp. 185–200, 1994.
- [21] C. A. Balanis, *Antenna Theory Analysis and Design*, 3rd Ed., Wiley, New York, NY, USA, 2005.
- [22] *IEEE Transactions on Antennas Propagation*, Vols. AP-17, No. 3, May 1969; Vol. AP-22, No. 1, January 1974; and Vol. AP-31, No. 6, Part II, November 1983.
- [23] P.J. Gibson, "The Vivaldi Aerial," in *9th European Microwave Conf.*, 1979.
- [24] J. A. N. Noronha, T. Bielawa, C. R. Anderson, D. G. Sweeney, S. Licul and W. A. Davis, "Designing antennas for UWB systems," *Microwaves and RF Mag.*, June 2003.
- [25] J. Shin and D. H. Schaubert, "A parameter study of stripline-fed Vivaldi notch-antenna arrays," *IEEE Transactions on Antennas and Propagat.*, vol. 47, no. 5, pp. 879-886, May 1999.
- [26] R. Garg, P. Bhartia, I. Bahl, A. Ittipiboon, *Microstrip Antenna Design Handbook*. Artech House, Inc., MA, 2001.
- [27] D. M. Pozar, *Microwave Engineering*. Second Edition, John Wiley & Sons, Inc., NY, 1998.
- [28] Agilent ADS 2003C, Agilent Technologies, 395 Page Mill Road, Palo Alto, CA 94303, USA, 2003.
- [29] Ansoft HFSS ver. 10.1, Ansoft Corporation, 225 West Station Square Drive, Suite 200, Pittsburgh, PA 15219 USA, 2006.
- [30] SMA Catalog, Amphenol Corporation, Four Old Newtown Road, Danbury, CT 06810 USA. http://www.amphenolrf.com/Products/CatalogPages/sma_catalog.pdf, pp.5584, 2007.

CHAPTER 5 NARROWBEAM ULTRA WIDEBAND ANTENNAS FOR
MICROWAVE BREAST CANCER DETECTION

- [31] J. X. Zheng and D. C. Chang, "End-correction network of a coaxial probe for microstrip patch antennas," *IEEE Trans. on Antennas and Propagat.*, vol. 39, pp. 115-118, 1991.
- [32] S. Gabriel, R. W. Lau and C. Gabriel, "The dielectric properties of biological tissues: II. Measurements on the frequency range 10 Hz to 20 GHz," *Phys. Med. Biol.*, vol. 41, no. 11, pp. 2251-2269, Nov. 1996.
- [33] E. J. Bond, S. C. Hagness and B. D. Van Veen, "Microwave imaging via space-time beamforming for early detection of breast cancer," *IEEE Trans. Antennas Propagat.*, vol. 51, no. 8, pp. 1690-1705, 2003.
- [34] W. Sörgel and W. Wiesbeck, "Influence of the antennas on the ultra-wideband transmission," *EURASIP Journal on Applied Signal Processing*, pp. 296-305, 2005.
- [35] K. C. L. Chan and Y. Huang, "A compact semi-circular disc dipole with notched-band for ultra-wideband applications," *Ultra Wideband Systems, Technologies and Applications*, pp. 226-230, 2006.

CHAPTER 6

CONCLUSIONS

The thesis presents novel approach to the detection of tumors of size well below a centimeter using a sub-wavelength ultra-wide band (UWB) microwave radar imaging technique. The approach belongs to the group of time-reversal techniques, which are considered promising for the purposes of UWB microwave imaging. The novel approaches described and explained in this thesis include two major contributions: 1) a robust convergence criterion based on the modified Shannon entropy measure, which leads to a unique unambiguous solution; 2) significantly enhanced resolution due to the use of the principle of phase-shifting mask for the design of the antenna array excitation.

In Chapter 2, the existing UWB microwave radar imaging techniques for breast cancer detection are reviewed.

In Chapters 3 and 4, the modified Shannon Entropy Criterion (SEC) is described and its application to determining when the time-reversed propagating wave focuses back to the scatterer.

CHAPTER 6 CONCLUSIONS

In Chapter 3, the novel robust TLM-based time-reversal microwave radar imaging technique is presented. The simulation required for the data acquisition model and the TR model is implemented in two-dimensional TM-mode and simulated using Matlab. The planar and cylindrical examples, with dielectric profile based on MRI-derived data of the breast of a 57-year old female, are used to demonstrate the advantages of the SEC as compared to the inverse varimax norm criteria. Then the need to use a technique for detection below the diffraction limit imposed by the UWB pulse is discussed.

In Chapter 4, a sub-wavelength UWB microwave imaging technique is proposed that incorporates SEC and the experimental setup formulated using PSM principle in a TR algorithm. The novel technique is then applied to detect a 0.5-mm diameter tumor using a 200-ps UWB pulse. The breast is in the supine position. We investigate the effect of dielectric contrast and the effect of the depth or the proximity of the tumor to the antenna receivers on the robustness of the SEC in detecting the sub-wavelength tumors. Based on these findings, a sub-wavelength microwave imaging technique that exploits two TRMs is proposed using the SEC and PSM in a TR algorithm to improve tumor localization.

In Chapter 5, we design the feed structure of an UWB antenna for microwave radar imaging. UWB antennas are fundamental components of UWB imaging systems. Many UWB radar imaging systems employ these antennas for transmitting and receiving short-duration UWB pulses. Consequently, studying

CHAPTER 6 CONCLUSIONS

the radiation and reception properties of these antennas is vital in order to determine their suitability for such applications.

The TEM horn antenna is studied and suggestions for future work are made regarding hardware implementations. In addition to the feed structure, antenna models and breast phantoms are implemented using Ansoft HFSS. For optimizing the feed structure circuit models in Agilent ADS were utilized.

The following research topics should be addressed in future developments.

- (1) Implementation of the sub-wavelength imaging technique using a time-reversal cavity (TRC) for UWB microwave radar imaging in the prone position.
- (2) Investigating the use of metamaterials and novel technologies to build antennas for sub-wavelength microwave imaging.
- (3) Investigating novel UWB antenna designs that use the developments and exploration in Chapter 5 to build upon and fabricate the designs.
- (4) Development of robust theory, which provides with a quantitative measure the resolution improvement of using the experimental setup for the sub-wavelength microwave radar imaging technique.

BIBLIOGRAPHY

Agilent ADS, Agilent Technologies, 1400 Fountaingrove Parkway, Santa Rosa, CA 95403-1799, USA.

American Cancer Society, "Cancer facts and figures 2007," Amer. Cancer Soc., Atlanta, GA, 2007.

J. R. Andrews, "UWB signal sources, antennas and propagation," *IEEE Tropical Conference on Wireless Communication Technology*, Hawaii, pp. 439-440, October 2003.

Ansoft HFSS ver. 10.1, Ansoft Corporation, 225 West Station Square Drive, Suite 200, Pittsburgh, PA 15219, USA, 2006.

M. H. Bakr, P. P. M. So and W. J. R. Hoefer, "The generation of optimal microwave topologies using time-domain field synthesis," *IEEE Trans. Microwave Theory Tech.*, vol. 50, pp. 2537-2544, Nov. 2002.

C. A. Balanis, *Antenna Theory Analysis and Design*, 3rd Ed., Wiley, New York, NY, USA, 2005.

T. W. Barret. History of Ultra Wideband (UWB) Radar and Communications: Pioneers and Innovators.

J. P. Berenger, "A perfectly matched layer for the absorption of electromagnetic waves," *J. Comput. Phys.*, vol. 114, pp. 185-200, 1994.

E. J. Bond, S. C. Hagness and B. D. Van Veen, "Microwave imaging via space-time beamforming for early detection of breast cancer," *IEEE Trans. Antennas Propagat.*, vol. 51, no. 8, pp. 1690-1705, 2003.

M. Born and E. Wolf, *Principles of Optics*. 6th Ed. New York: Pergamon Press, 1980.

BIBLIOGRAPHY

- A. E. Bulyshev, S. Y. Semenov, A. E. Souvorov, R. H. Svenson, A. G. Nazarov, Y.E. Sizov and G. P. Tatsis, "Computational modeling of three-dimensional microwave tomography of breast cancer," *IEEE Trans. Biomed. Eng.*, vol. 48, no. 9, pp. 1053-1056, Sep. 2001.
- R. Carminati, J. J. Saenz, J. -J. Greffet and M. Nieto-Vesperians, "Reciprocity, unitarity, and time-reversal symmetry of the S matrix of fields containing evanescent components," *Phys. Rev.*, vol. A 62, 012712, 2000.
- D. Cassereau and M. Fink, "Time-reversal of ultrasonic fields. III. Theory of the closed time-reversal cavity," *IEEE Trans. Ultrason. Ferroelectr. Freq. Control*, vol. 39, pp. 579-592, Sept. 1992.
- S. S. Chaudhary, R. K. Mishra, A. Swarup and J. M. Thomas, "Dielectric properties of normal and malignant human breast tissues at radiowave and microwave frequencies," *Indian J. Biochem. Biophys.*, vol. 21, pp. 76-79, Feb. 1984.
- K. C. L. Chan and Y. Huang, "A compact semi-circular disc dipole with notched-band for ultra-wideband applications," *Ultra Wideband Systems, Technologies and Applications*, pp. 226-230, 2006.
- W. C. Chew, *Waves and Fields in Inhomogeneous Media*. New York: Van Nostrand Reinhold, 1990.
- C. Christopoulos, *The Transmission-Line Modeling (TLM) method in Electromagnetics*, Morgan & Claypool Publishers, San Rafael, CA, USA, 2006.
- S. K. Davis, H. Tandradinata, S. C. Hagness and B. D. Van Veen, "Ultrawideband microwave breast cancer detection: a detection-theoretic approach using the generalized likelihood ratio test," *IEEE Trans. Biomed. Eng.*, vol. 52, no. 7, 2005.
- J. G. Elmore, M. B. Barton, V. M. Moceris, S. Polk, P. J. Arena and S. W. Fletcher, "Ten-year risk of false positive screening mammograms and clinical breast examinations," *New Eng. J. Med.*, vol. 338, no. 16, pp. 1089-1096, 1998.
- E. C. Fear, S. C. Hagness, P. M. Meaney, M. Okoniewski and M. A. Stuchly, "Enhancing breast tumor detection with near field imaging," *IEEE Microwave Mag.*, vol. 3, pp. 8-56, Mar 2002.

BIBLIOGRAPHY

E. C. Fear, X. Li, S. C. Hagness and M. A. Stuchly, "Confocal microwave imaging for breast cancer detection: Localization of tumors in three dimensions," *IEEE Trans. Biomed. Eng.*, vol. 49, pp. 812–822, Aug. 2002.

E. C. Fear, J. Sill and M. A. Stuchly, "Experimental feasibility study of confocal microwave imaging for breast tumor detection," *IEEE Trans. Microwave Theory Tech.*, vol. 51, no. 3, pp. 887–892, 2003.

E. C. Fear and M. A. Stuchly, "Microwave detection of breast cancer," *IEEE Trans. Microwave Theory Tech.*, vol. 48, no. 11, pp. 1854–1863, 2000.

M. Fink, *Phys. Today* 50, 34, 1997.

M. Fink, D. Cassereau, A. Derode, C. Prada, P. Roux, M. Tanter, J. L. Thomas and F. Wu, "Time-reversed acoustics," *Rep. Prog. Phys.*, vol. 63, pp. 1933–1995, 2000.

R. J. Fontana. A Brief History of UWB Communications. Multispectrum Solutions, Inc.

M. Forest and W. J. R. Hoefer, "TLM synthesis of microwave structures using time reversal," in *IEEE MTT-S Int. Microwave Symp. Dig.*, pp. 779–782, Jun. 1992.

S. Gabriel, R. W. Lau and C. Gabriel, "The dielectric properties of biological tissues: II. Measurements on the frequency range 10 Hz to 20 GHz," *Phys. Med., Biol.*, vol. 41, no. 11, pp. 2251–2269, Nov. 1996.

R. Garg, P. Bhartia, I. Bahl and A. Ittipiboon, *Microstrip Antenna Design Handbook*. Artech House, Inc., MA, 2001.

D. Ghosh, A. De, M. C. Taylor, T. K. Sarkar, M. C. Wicks and E. L. Mokole, "Transmission and reception by ultra-wideband (UWB) antennas," *IEEE Antennas and Propagat. Mag.*, vol. 48, no. 5, pp. 67–99, October 2006.

P. J. Gibson, "The Vivaldi Aerial," in *9th European Microwave Conf.*, 1979.

S. C. Hagness, A. Taflove and J. E. Bridges, "Two-dimensional FDTD analysis of a pulsed microwave Confocal system for breast cancer detection: fixed-focus and antenna-array sensors," *IEEE Trans. Biomed. Eng.*, vol. 45, no. 12, pp. 1470–1479, 1998.

BIBLIOGRAPHY

S. C. Hagness, A. Taflove and J. E. Bridges, "Three-Dimensional FDTD analysis of a pulsed microwave Confocal system for breast cancer detection: design of an antenna-array element," *IEEE Trans. Antennas Propagat.*, vol. 47, no. 5, pp. 783-791, 1999.

D. M. Hailu, N. K. Nikolova and M. H. Bakr, "Sub-wavelength microwave radar imaging for detection of breast cancer tumors," in *2007 IEEE Int. Microwave Symp. on Signals, Systems, and Electronics*, pp.107-110, Montréal, Canada, July 2007.

D. M. Hailu, "Review of ultrawideband microwave radar imaging techniques for breast cancer detection," Computational Electromagnetic Lab Technical Report, CEM-R-38, January 2007.

D. M. Hailu, "Narrowbeam ultrawideband antennas for microwave breast cancer detection," Computational Electromagnetic Lab Technical Report, CEM-R-42, March 2007.

S. Haykin, *Adaptive Filter Theory*. Upper Saddle River, NJ: Prentice-Hall, 1996.

P. T. Huynh, A. M. Jarolimek and S. Daye, "The false-negative mammogram," *Radiograph*, vol. 18, no. 5, pp. 1137-1154, 1998.

IEEE Transactions on Antennas Propagation, Vols. AP-17, No. 3, May 1969; Vol. AP-22, No. 1, January 1974; and Vol. AP-31, No. 6, Part II, November 1983.

H. M. Jafari, M. J. Deen, S. Hranilovic and N. K. Nikolova, "Slot antenna for ultra-wideband applications," in *2006 IEEE Antennas and Prop. Symp.*, pp. 1107-1110, 2006.

W. T. Joines, Y. Zhang, C. Li and R. L. Jirtle, "The measured electrical properties of normal and malignant human tissues from 50 to 900 MHz," *Med. Phys.*, vol. 21, pp. 547-550, Apr. 1994.

A. B. Kahng and Y. C. Pati, "Subwavelength optical lithography: challenges and impact on physical design," in *1999 Int. Symp.on Physical Design*, pp. 112-119, 1999.

H. Kanj and M. Popović, "Miniaturized microstrip-fed "Dark Eyes" antenna for near-field microwave sensing," *IEEE Antennas and Wireless Propagat. Lett.*, pp. 1-4, 2005.

BIBLIOGRAPHY

- P. Kosmas and C. M. Rappaport, "Time reversal with the FDTD method for microwave breast cancer detection," *IEEE Trans. Microwave Theory Tech.*, vol. 53, no. 7, pp. 2317-2323, July 2005.
- P. Kosmas and C. M. Rappaport, "A matched-filter FDTD-based time reversal approach for microwave breast cancer detection," *IEEE Trans. Antennas and Propagat.*, vol. 54, no. 4, pp. 1257-1264, April 2006.
- S. Lehman and A. J. Devaney, "Transmission mode time-reversal superresolution imaging," *J. Acoust. Soc. Amer.*, vol. 113, pp. 2742-2753, 2003.
- G. Lerosey, J. de Rosny, A. Tourin and M. Fink "Focusing beyond the diffraction limit with far-field time reversal," *Science Mag.*, vol. 315. no. 5815, pp. 1120 – 1122, February 23, 2007.
- M. D. Levenson, N. S. Viswanathan and R. A. Simpson, "Improving resolution in photolithography with a phase-shifting mask," *IEEE Trans. Electron Devices*, ED-29, no. 12, pp. 1828-1836, 1982.
- X. Li, E. J. Bond, B. D. Van Veen and S. C. Hagness, "An overview of ultra-wideband microwave imaging via space-time beamforming for early-stage breast-cancer detection," *IEEE Antennas Propagat. Mag.*, vol. 47, pp. 19-34, Feb. 2005.
- X. Li, S. K. Davis, S. C. Hagness, D. W. Weide and B. D. Van Veen, "Microwave imaging via space-time beamforming: experimental investigation of tumor detection in multilayer breast phantoms," *IEEE Trans. Microwave Theory Tech.*, vol. 52, pp. 1856-1865, Aug. 2004.
- X. Li and S. C. Hagness, "A confocal microwave imaging algorithm for breast cancer detection," *IEEE Microwave Wireless Compon. Lett.*, vol. 11, no. 3, pp. 130-132, 2001.
- X. Li, S. C. Hagness, M. K. Choi and D. W. Van Der Weide, "Numerical and experimental investigation of an ultrawideband ridged pyramidal horn antenna with curved launching plane for pulse radiation," *IEEE Trans. Aantennas and Wirelss Propagat. Lett.*, vol. 2, pp. 259-262, 2003.
- D. Li, P. M. Meaney, T. Raynolds, S. A. Pendergrass, M. W. Fanning and K. D. Paulsen, "Parallel-detection microwave spectroscopy system for breast imaging," *Rev. Sci. Instrum.*, vol. 75, pp. 2305-2313, 2004.

BIBLIOGRAPHY

Q. H. Liu, Z. Q. Zhang, T. T. Wang, J. A. Bryan, G. A. Ybarra, L. W. Nolte and W. T. Joines, "Active microwave imaging I – 2-D forward and inverse scattering methods," *IEEE Trans. Microwave Theory Tech.*, vol. 50, no. 1, pp. 123-133, January 2002.

Mammography and Beyond: Developing Techniques for the Early Detection of Breast Cancer. Washington, DC: Institutes of Medicine, National Academy Press, 2001.

MATLAB™ 7.1, The MathWorks Inc., 3 Apple Hill Drive, Natick, MA, 2005.

P. M. Meaney and K. D. Paulsen, "Nonactive antenna compensation for fixed-array microwave imaging: Part II—Imaging results," *IEEE Trans. Med. Imag.*, vol. 18, no. 6, pp. 508-518, June 1999.

P. M. Meaney, M. W. Fanning, D. Li, S. P. Poplack and K. D. Paulsen, "A clinical prototype for active microwave imaging for the breast," *IEEE Trans. Microwave Theory Tech.*, vol. 48, no. 11, pp. 1841-1853, Nov. 2000.

J. A. N. Noronha, T. Bielawa, C. R. Anderson, D. G. Sweeney, S. Licul and W. A. Davis, "Designing antennas for UWB systems," *Microwaves and RF Mag.*, June 2003.

B. M. Notaros, C. D. McCarrick and D. P. Kasilingam, "Two numerical techniques for analysis of pyramidal horn antennas with continuous metallic ridges," in *IEEE AP-S Int. Symp.*, vol. 2, pp. 560–563, 2001.

M. Piket-May, A. Taflove and J. Baron, "FD-TD modeling of digital signal propagation in 3-D circuits with passive and active loads," *IEEE Trans. Microwave Theory Tech.*, vol. 42, pp. 1514–1523, Aug. 1994.

E. D. Pisano, M. J. Yaffe and C. M. Kuzmiak, *Digital Mammography*, Lippincott Williams & Wilkins, Philadelphia, PA, USA 2004.

S. P. Poplack, P. M. Meaney, A. Hartov, K. D. Paulsen, T. D. Torsteson, M. R. Grove, S. K. Soho and W. A. Wells, "Electromagnetic breast imaging: Average tissue property value in women with negative clinical findings," *Radiol.*, vol. 231, no. 2, pp. 571-580, May 2004.

D. M. Pozar, *Microwave Engineering*. Second Edition, John Wiley & Sons, Inc., NY, 1998.

BIBLIOGRAPHY

- J. de Rodny and M. Fink, "Overcoming the diffraction limit in wave physics using a time-reversal mirror and a novel acoustic sink," *Phys. Rev. Lett.* vol. 89, 124301, 2002.
- E. T. Rosenbury, G. K. Burke, S. D. Nelson, R. D. Stever, G. K. Gerverno and D. J. Mullenhoff, "Low cost impulse compatible wideband antenna," *U.S. Patent* 6 348 898.
- C. Shannon and W. Weaver, *The Mathematical Theory of Communication*. Urbana, University of Illinois, 1964.
- J. Shin and D. H. Schaubert, "A parameter study of stripline-fed Vivaldi notch-antenna arrays," *IEEE Transactions on Antennas and Propagat.*, vol. 47, no. 5, pp. 879-886, May 1999.
- J. M. Sill and E. C. Fear, "Tissue sensing adaptive radar for breast cancer detection—experimental investigation of simple tumor models," *IEEE Trans. Microwave Theory Tech.*, vol. 53, pp. 3312-3319, Nov. 2005.
- SMA Catalog, Amphenol Corporation, Four Old Newtown Road, Danbury, CT 06810 USA. http://www.amphenolrf.com/Products/CatalogPages/sma_catalog.pdf, pp.55-84, 2007.
- W. Sörgel and W. Wiesbeck, "Influence of the antennas on the ultra-wideband transmission," *EURASIP Journal on Applied Signal Processing*, pp. 296-305, 2005.
- R. Sorrentino, L. Rosseli and P. Mezzanote, "Time-reversal in finite difference time domain method," *IEEE Microwave Guided Wave Lett.*, vol. 3-11, no. 11, pp. 402-404, Nov. 1993.
- R. Sorrentio, P. P. M. So and W. J. R. Hoefer, "Numerical microwave synthesis by inversion of the TLM process", in *21st European Microwave Conference Digest*, pp. 1273-1277, Stuttgart, Germany, Sept. 1991.
- A. E. Souvorov, A. E. Bulyshev, S. Y. Semenov, R. H. Svenson and G. P. Tatsis, "Two-dimensional computer analysis of a microwave flat antenna array for breast cancer tomography," *IEEE Trans. Microwave Theory Tech.*, vol. 48, no. 8, pp. 1413-1415, Aug. 2000.
- J. R. Taylor, *Scattering Theory*, FL: R. Krieger Inc., 1983.

BIBLIOGRAPHY

- N. Tavasolian, H. Kanj and M. Popović, "The effect of breast glands on microwave tumor sensing with 'dark eyes' antenna," in *2006 IEEE Antennas and Propagat. Symp.*, pp. 291-294, 2006.
- B. Van Veen, "Minimum variance beamforming," in *Adaptive Radar Detection and Estimation*, S. Haykin and A. Steinhardt, Eds. New York: Wiley, 1992, ch. 4, pp. 161-236.
- K. L. Walton and V. C. Sundberg, "Broadband ridged horn design," *Microwave J.*, vol. 4, no. 2, pp. 96-101, Apr. 1964.
- D. W. Winters, E. J. Bond, B. D. Van Veen and S. C. Hagness, "Estimation of the frequency-dependent average dielectric properties of breast tissue using a time-domain inverse scattering technique," *IEEE Trans. Antennas Propagat.*, Vol. 54, no. 11, November 2006.
- T. T. Wu and R. W. P. King, "The cylindrical antenna with non-reflecting resistive loading," *IEEE Trans. Antennas and Propagat.*, vol. 13, no. 3, pp. 369-373, 1965.
- X. Yun, E. C. Fear and R. H. Johnston, "Compact antenna for radar-based breast cancer detection," *IEEE Trans. Antennas and Propagat.*, vol. 53, pp. 2374-2380, 2005.
- Z. Q. Zhang, Q. Liu, C. Xiao, E. Ward, G. Ybarra and W. T. Joines, "Microwave breast imaging: 3-D forward scattering simulation," *IEEE Trans. Biomed. Eng.*, vol. 50, no. 10, pp. 1180-1189, Oct. 2003.
- J. X. Zheng and D. C. Chang, "End-correction network of a coaxial probe for microstrip patch antennas," *IEEE Trans. on Antennas and Propagat.*, vol. 39, pp. 115-118, 1991.
- W. Zhi, F. Chin and M. Chia, "Near Field UWB LCMV imaging for breast cancer detection with entropy based artifacts removal," in *IEEE Int. Conf. on Acoustics, Speech, and Signal Processing*, vol. 2, II-577 - II-580, May 2006.